Politecnico di Torino

Master of Science in Environmental and Land Engineering
Track: Climate Change
A.Y. 2023/2024
Graduation Session March 2025

Regional vegetation tipping in a numerical Earth system Model of Intermediate Complexity

Supervisors:
Prof. Jost Diedrich Graf Von Hardenberg
Prof. Francesco Ragone

Candidate:
Lisa Ferrari

Abstract

Vegetation plays a fundamental role in the climate system, influencing energy exchange, the hydrological cycle and atmospheric composition. At the same time, vegetation dynamics are strongly influenced by climatic conditions, creating complex feedback mechanisms that regulate the Earth's climate. Representing these interactions between climate and vegetation is essential in numerical climate models, which must realistically simulate vegetation to improve the representation of the climate system. This thesis focuses on the Planet Simulator (PlaSim), an Earth system Model of Intermediate Complexity, and on the Simulator for Biospheric Aspects (SimBA), its embedded simple dynamic vegetation model. SimBA can operate in two modes: in the non-interactive vegetation mode simulated vegetation does not influence the climate, while in the interactive mode vegetation influences the climate through four land surface variables: surface albedo, surface roughness, surface conductance and soil water holding capacity.

The work begins with an introduction on the role of vegetation in the climate system, with a focus on Leaf Area Index (LAI), a variable used as an indicator of vegetation characteristics, followed by a detailed description of SimBA parametrizations. A significant part of the research focused on the tuning of SimBA parametrizations in the interactive vegetation mode, specifically the snow-free albedo and soil water holding capacity, allowing for a more realistic representation of the climate system. Subsequently, an analysis of the climate simulated using SimBA was carried out to evaluate the changes induced by an interactive vegetation compared to a non-interactive one, and to assess biases with observations, obtained from the ERA5 reanalysis.

An analysis was conducted to evaluate how well PlaSim simulates vegetation at both global and regional scales. The LAI simulated by PlaSim was compared to benchmarks (GIMMS LAI4g and ERA5 reanalysis datasets) and to four Earth System Models from the sixth phase of the Coupled Model Intercomparison Project (CMIP6), with the aim of contextualizing the performance of PlaSim within the framework of more complex models. The analysis revealed that PlaSim struggles to represent seasonal cycles both in the mid-latitudes and the tropics, while it performs relatively well in replicating the global spatial distribution and mean global value, remaining within the range of CMIP6 models. Lastly, a simulation with increasing atmospheric CO_2 concentration was run using PlaSim in the tuned interactive vegetation mode. The goal was to investigate how vegetation responded to rising atmospheric CO_2. Specifically, regional vegetation tipping was analysed in Europe and the Amazon rainforest. The simulation revealed instances of regional vegetation tipping, occurring both in mid-latitudes and the tropics, driven by non-linear feedbacks between changes in hydrological cycle and shifts in vegetation patterns.

Contents

Introduction

Vegetation is an essential component of the climate system, as it influences the climate through various physical and chemical feedbacks. Therefore, it should be appropriately represented in numerical climate models, which are complex numerical representations of the climate system (IPCC, 2012). Earth system Models of Intermediate Complexity (EMICs) are numerical climate model of particular interest, as they bridge the gap between simple conceptual models and more comprehensive Global Climate Models (GCMs). These models replicate the Earth system, along with almost all Earth components and their interactions rather completely, but in a simplified way compared to more complex models (Shi et al., 2019). EMICs are particularly interesting due to their coarser resolution and simpler parametrizations, which allows for long-term simulations with relatively low computational costs (Angeloni et al., 2020). Given the critical role of vegetation in the climate system, EMICs should contain a reasonably accurate representation of dynamic vegetation and its feedback on the climate system.

This thesis focuses on the Planet Simulator (PlaSim), an Earth-system Model of Intermediate complexity developed at the University of Hamburg, and particularly on its dynamic vegetation module, the Simulator for Biospheric Aspects (SimBA) (Lunkeit et al., 2011). The simple dynamic vegetation model embedded in PlaSim can operate in two modes: in the non-interactive vegetation mode, simulated vegetation does not influence the climate, while in the interactive mode, vegetation influences the climate through four land-surface variables. SimBA had rarely been used before, since its interactive vegetation mode had not yet been tuned prior to this work. The first objective of the present work was to tune the dynamic vegetation module in its interactive mode, allowing for a more realistic representation of the climate system. This step enabled the use of an interactive vegetation in climate simulations.

The intrinsic characteristics of EMICs, coupled with a dynamic vegetation module that can influence the climate system, allow for the study of topics such as vegetation tipping points. This is made possible by the ability of EMICs to simulate long time scales, coupled with their rather complete representation of Earth components. The introduction of a tuned interactive vegetation in PlaSim, which was carried out as part of this thesis, enables the study of vegetation response to increasing atmospheric CO_2, particularly in relation to vegetation tipping points. One of the possible tipping elements of the climate system is the Amazon dieback (Chen et al., 2021), which was the focus of the final part of this work.

To summarize, this work had various objectives. First, the tuning of SimBA parametrizations in the interactive vegetation mode was carried out to improve the representation of the simulated climate. Second, the simulated vegetation was compared to both observations and CMIP6 model, to assess how well PlaSim could represent vegetation dynamics. Finally, the tuned vegetation mode was used to investigate vegetation tipping in two regions: Europe and the Amazon rainforest.

An outline of the chapters and their respective topics is provided below. While the first two chapters provide general background information, each chapter after that builds upon the key findings of the previous one.

Chapter one provides an introduction to the importance of vegetation in the climate system, focusing on biogeochemical and biogeophysical feedbacks. It introduces the Leaf Area Index (LAI), a key variable throughout this work, as it serves as an indicator of vegetation characteristics. This chapter provides an explanation on how LAI is measured, and it discusses the available LAI datasets. Finally, it addresses how LAI is expected to change in the future and it provides a brief introduction on the role of LAI in numerical climate models.

Chapter two introduces the Planet Simulator (PlaSim), and it provides an in depth explanation of SimBA parametrizations, which serve as an important background for the topics addressed in the following chapter.

Chapter three explains the tuning process applied to both the snow-free albedo and soil water holding capacity parametrizations, which improved the representation of the climate system. Lastly it provides an analysis of the simulated climate, comparing observations with the results of two PlaSim simulations, one in the non-interactive and one in the tuned interactive vegetation mode. This analysis is aimed at understanding how an interactive vegetation affects the climate compared to non-interactive vegetation, and assessing the biases with observations.

Chapter four focuses on evaluating how the LAI simulated in PlaSim compares to observations, and it contextualizes its performance in the framework of more complex Earth System Model from the CMIP6 project. The analysis was carried out at both global and regional scales, with a focus on both Europe and the Amazon. Specifically, spatial patterns, seasonality, mean global value and interannual variability are examined. This evaluation of vegetation in PlaSim is essential to highlight its strengths and limitations and to validate its use for the analysis presented in the last chapter.

Chapter five presents the results of the analysis aimed at identifying vegetation tipping in both Europe and the Amazon rainforest. First, it provides a description of the experimental setup used to run the PlaSim simulation, followed by an introduction to the two regions considered, their significance within the climate system and the risk of Amazon dieback, which is considered a possible tipping element of the climate system. Then, the results of the analysis are presented, detailing where abrupt changes are observed in the two regions and how they are linked to changes in the hydrological cycle.

The most important findings are summarized in the **Conclusions**.

1. General background on the interaction between vegetation and the climate system

1.1. The role of the biosphere in the climate system

The biosphere is an essential part of the climate system, and it influences many aspect of the Earth climate, including atmospheric composition, surface temperature and the hydrological cycle. Energy exchange, hydrological cycle and atmospheric composition are influenced through chemical, physical and biological processes such as radiation, evapotranspiration, photosynthesis, precipitation interception and carbon uptake (Bonan, 2008). Living organisms, both on land and in the ocean, are responsible for the composition of the atmosphere on Earth, which differs from that of other planets for its high concentration of oxygen and relatively low carbon dioxide levels. Moreover, forests and vegetation influence surface albedo and transfer soil water to the leaf surface, where it is evaporated.

Changes in the climate affect both the biosphere and vegetation, which in turn can influence the climate system through different feedbacks. These processes regulate the interactions between the biosphere and the Earth climate system. They are divided into two categories: biogeochemical and biogeophysical feedbacks (Prentice et al., 2015).

Biogeochemical feedbacks involve the exchange of greenhouse gases and aerosols between the ecosystems and the atmosphere, which are mediated by biological organisms. They include processes such as:

- The CO_2 fertilization effect, which refers to the increase in primary production as a consequence of rising atmospheric CO_2. This mechanism generally causes an increases in carbon uptake.
- Increasing emission of biogenic volatile organic compounds (BVOCs) from plants, due to increasing leaves temperature. BVOCs are responsible for increased production of secondary organic aerosols, which have a cooling effect on the climate.
- Changes in fire regimes, which release carbon to the atmosphere more rapidly than it would happen through decomposition, thus decreasing the total carbon storage on land. Fires also emit black carbon, which reduces snow albedo, the fraction of solar radiation reflected into space, and leads to warming. On the other hand, organic compounds released by fire lead to cooling.

Biogeophysical feedbacks arise from the influence of vegetation on physical properties of ecosystems (e.g. surface albedo). Biogeoophysical feedbacks include changes in surface albedo and changes in transpiration rates, which can impact the hydrological cycle. For example, different vegetation types have different albedo values, and as vegetative cover changes due to warming, surface temperatures likely change as well.

The influence of vegetation on the climate system is quite different for different biomes and forest types. Tropical forests, which represent 45% of forest area on Earth, display high rates of evapotranspiration, producing a decrease in temperature and an increase in precipitation compared to pastureland. In Amazonia, tropical Asia and Africa, cooling due to evapotranspiration offsets the decreasing albedo of forests compared to non-forested areas. Tropical forests also contribute to global warming mitigation through carbon sequestration, but they are quite vulnerable to dryer, warmer climates, which can lead to forest dieback. Boreal forests, located at high altitudes in the northern hemisphere, account for 27% of the world's total forested area. The lower surface albedo during the snow season, due to the presence of trees, leads to warming of the climate compared to their absence, influencing the global average temperature. Moreover, compared to tropical forests, they show weaker evaporation rates (and subsequently lower evaporative cooling) and more moderate carbon storage. Lastly, temperate forests, which account for 16% of the global forest area, show moderate evaporative cooling (lower than that of tropical forests and higher than that of boreal forests), lower albedo compared to cropland, and strong carbon storage (Bonan, 2008; FAO (Food and Agriculture Organization of the United Nations), 2020). The spatial distribution of different forest biomes is shown in *Figure 1*.

This thesis focuses on biogeophysical feedbacks, as the carbon cycle is not represented in the climate model used in this work. Moreover, vegetation characteristics will be examined through the leaf area index (LAI). This parameter is used in many Earth System Models to depict vegetation structure and canopy (Bonan, 2008). LAI influences climate variables such as albedo and it is relatively easy to measure compared to other quantities that describe vegetation. Additionally, it is available in many satellite products.

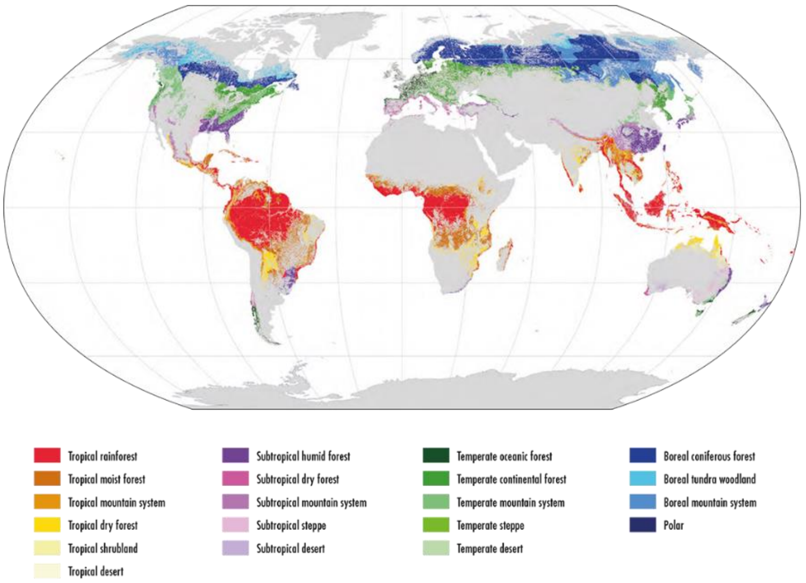

Figure 1: Distribution of forests with tree cover of at least 30 percent in 2015, according to the Copernicus moderate resolution (100m) land-cover map (FAO (Food and Agriculture Organization of the United Nations), 2020).

1.2. Leaf Area Index: definition and measurements

The Leaf Area Index (LAI) quantifies the amount of leaf material present in an ecosystem. It is defined as half of the total green area per unit horizontal ground surface area, it is a dimensionless variable that generally varies between 0 and 10, depending on local environmental conditions (Global Climate Observing System, s.d.).

The Leaf Area Index in a region can be estimated either through field measurements or through remote sensing methods (Fang et al., 2019). Field measurements of LAI are generally obtained using:

- Direct methods, which mainly consist of harvesting leaves (destructing sampling) or collecting leaf litters, the plant material that has fallen to the ground, which is then sorted by species. The leaf surface is then measured using scanners or through laboratory tests, during which the leaf area per unit of dry leaf mass (SLA) is assessed for each age class and then multiplied by the dry mass to obtain the Leaf Area Index.

  Direct methods are generally quite time-consuming and labour-intensive, and they may conflict with the principle of nature conservation. Nonetheless, they allow a good estimate of the true LAI value, thus providing reference values for indirect and satellite measurements.
- Indirect methods, which are either based on the use of allometric equations or optical methods. The latter involves different available devices that measure the transmission of radiation

through canopy to estimate the LAI, while allometric equations link the Leaf Area Index to other readily measurable biophysical variables, such as the diameter at breast height (DBH). Allometric equations vary based on taxonomy, locations and other factors (Yan et al., 2019). Compared to direct methods, indirect methods are non-destructive, and they are widely used for remote sensing validation (Yan et al., 2019). Direct methods are faster than indirect methods and they are generally used to survey large areas.

There are primarily two approaches used in remote sensing LAI estimation:

- Empirical relationships with canopy reflectance or with Vegetation Indices (VIs), which are spectral transformations of two or more bands used to assess various vegetation properties, such as photosynthetic activity and canopy structural variations (Huete et al., 2002).
  Existing empirical relationships still show limitations due to their sensitivity to external factors, such as vegetation type, atmospheric quality, leaf chlorophyl content and background reflectance. New Vegetation Indices that are robust to these factors while remaining sensitive to LAI must be developed in the future to improve the estimation ability. Furthermore, the accuracy of the empirical relationship method depends on the used ground measurement datasets and their representativeness (Yang et al., 2022).
- Model inversion methods. The LAI is estimated from canopy reflectance using available canopy reflectance models, which define the interaction between canopy and radiation (Yang et al., 2022). The LAI estimation is performed through a model inversion method, in which canopy biophysical variables are determined by finding the best fit between the remote sensing reflectance and the computed reflectance (Fang et al., 2019). However, the problem is usually ill-posed, as the number of unknowns is often higher than the number of reflectance bands supplied by observations, which can lead to inaccurate inversion results. Different regularization strategies have been proposed to solve this issue and increase the robustness of estimation, including the use of prior parameter constraints and multi-source observations (Yan et al., 2019).

The data used for the measurement mainly derives from passive optical sensors, LiDAR (Light Detection and Ranging), and microwave sensors.

Passive optical sensors have been widely used since the 1980s to measure LAI at different spatial scales, thanks to their cost-effectiveness and their ability to acquire observations regularly. Currently, numerous LAI datasets are available from different sensors, including MODIS, LANDSAT and CYCLOPES. The main issue linked to the use of passive optical sensors is their saturation over canopies with high LAI. Moreover, unlike active sensors, passive sensors can only be used in daylight (Tang et al., 2014).

LiDAR sensors, which are active optical sensors, can be employed to estimate LAI. Different approaches may be used:

- LiDAR sensors measure the canopy gap fraction, which is the fraction of the canopy layer that is not blocked by wood and foliage. The gap fraction is then correlated with the Leaf Area Index.
- LiDAR sensors provide estimates of biophysical parameters such as foliage density and canopy cover, which are used in allometric equations to estimate the LAI.

Their main advantages are their cost effectiveness and their ability to measure the vertical LAI profile at different heights. Different LiDAR platforms can be used: ground-based, airborne and spaceborne. Passive optical sensors can be used in combination with LiDAR sensors either to improve the biophysical parameters estimation or to perform quality assessment of the LiDAR-derived LAI.

Finally, microwave sensors have the potential to bridge the information gaps from optical sensors acquisitions caused by cloud cover, therefore the combination of these two sensors may allow improvement in LAI estimations. The use of microwave sensors still poses challenges caused by observational conditions, sensor configuration, and the underlying soil (Fang et al., 2019).

1.3. Global LAI products

Different moderate resolution (250 m to 7 km) global LAI datasets have been made available over the past decades, such as GIMMS (Global Inventory Modelling and Mapping Studies), GLASS (Global Land Surface Satellite) and GLOBMAP LAI. Most of these products were derived from MODIS (Moderate Resolution Imaging Spectroradiometer) and AVHRR (Advanced Very High Resolution Radiometer) sensors, using different methodologies (Song et al., 2021).

MODIS sensors are aboard the Terra and Aqua satellites, launched by NASA in 1999 and 20002 respectively. They acquire data in 36 spectral bands, and they image the Earth every 1 to 2 days. The spatial resolution varies from 250 m to 1 km, depending on the band. They allow to understand and monitor both global dynamics and processes occurring in oceans, land, and lower atmosphere (National Aeronautics and Space Administration, s.d.). They provide a spatial and radiometric resolution that is superior to the one of AVHRR sensors, therefore ensuring better spatial, radiometric and spectral representation of vegetation (Lu et al., 2015).

The AVHRR is a scanning system aboard the National Oceanic and Atmospheric Administration (NOAA) family of polar orbiting platforms and European MetOp satellites. They are equipped with five spectral bands, with a resolution of 1.1 km, scanning the Earth twice per day. The AVHRR was designed to provide radiance data to analyse clouds distribution, land-water boundaries, sea surface temperatures and vegetation classification and greenness through passively measured visible, near infrared and thermal infrared radiation bands. The AVHRR instruments have been used since the early 1980's to generate global LAI measures, offering the longest available time record of data (National Oceanic and Atmospheric Administration (NOAA), s.d.). However, AVHRR sensor degradation and orbital drift are two significant sources of inconsistency to build robust LAI models, as well as insufficient reference data prior to the late 1990's. The reprocessing of AVHRR historical data is therefore crucial to ensure consistency with current records (Fang et al., 2019).

Uncertainties in LAI estimations from indirect methods are generally higher in areas where LAI is high, this is because the value can be measured when light reaches the soil and it is scattered back in a measurable amount (Gobron & Verstraete, 2009). Some studies showed that uncertainties in LAI estimations from MODIS data, calculated from the standard deviation and the error layers, are higher in the boreal and tropical regions and during summer, due to high LAI values (Fang et al., 2019).

1.4. Importance of LAI in the climate system

The Leaf area index is an essential climate variable, which is a physical, chemical or biological variable or a group of linked variables that critically contribute to the characterization of the climate on Earth (Global Climate Observing System, s.d.). LAI is used as an indicator of the state of vegetation development, to characterize its physical properties, and to describe the vegetation feedback to the climate system (Boussetta et al, 2013; Fang et al., 2019).

As previously mentioned, vegetation influences albedo. In snow free areas, an increase in LAI generally reduces surface albedo, since grass and crops have higher albedo than other plant functional types, as shown in *Figure 2*. Similarly, the presence of forests in snow-covered areas causes lower albedo values compared to crops and grass. The decrease in albedo due to the presence of forests increases the heating of land, contributing to its warming (Bonan, 2008).

Forests impact the hydrological cycle by releasing water vapor in the atmosphere through evapotranspiration, which further contributes to cooling by increasing cloud formation. Cloud formation, in turn, determines positive feedback on precipitations, whose increase generally benefits the ecosystem (Bonan, 2008). An increase in LAI generally enhances canopy evapotranspiration. Global modelling studies revealed that the rise in global LAI has led to an increase in land evapotranspiration, contributing to half of the observed rise in evapotranspiration over the past 30 years (Fang et al., 2019).

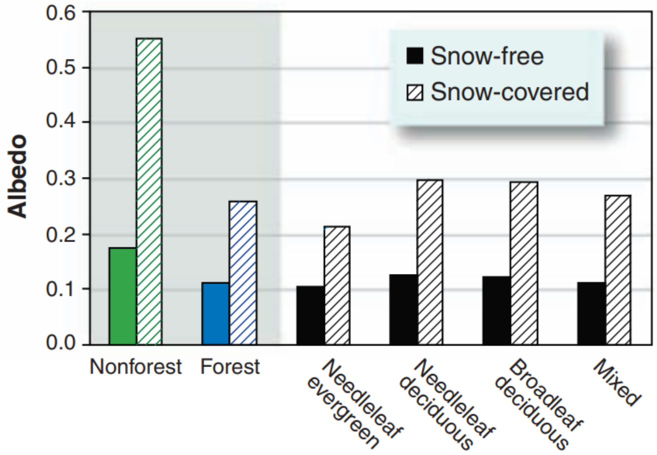

Figure 2: Satellite derived values of albedo for snow-covered and snow-free non forest and forest biomes (Bonan, 2008).

To conclude, LAI links biogeochemical and biogeophysical processes (carbon cycle, albedo and evapotranspiration) at different spatial and temporal scales and is a key variable for understanding how vegetation influences the climate (Song et al., 2021).

1.5. Past and future changes in LAI

The Leaf Area Index influences the climate, but it is also subject to change. Global satellite LAI products show an increase in global average growing season (April to October) between 2001 and 2017, with higher positive trends in Eurasia, particularly in China. Satellite data shows positive trends in most of the world, especially in Europe and Asia, as shown in *Figure 3*.

The mean global LAI has been increasing since the preindustrial period, consistently with the increase in global temperatures, and it is projected to increase during the 21st century. However, the trend is projected to be different in different regions: a study using different models showed that the increase is projected to be larger in high and mid-latitude regions, the Tibetan plateau and the tropics, while LAI is projected to decrease in Australia, due to a decrease in precipitation. Studies showed that LAI variations are more heavily impacted by temperatures at high and mid-latitudes, while in tropical regions they are mainly influenced by moisture levels (Fang et al., 2019).

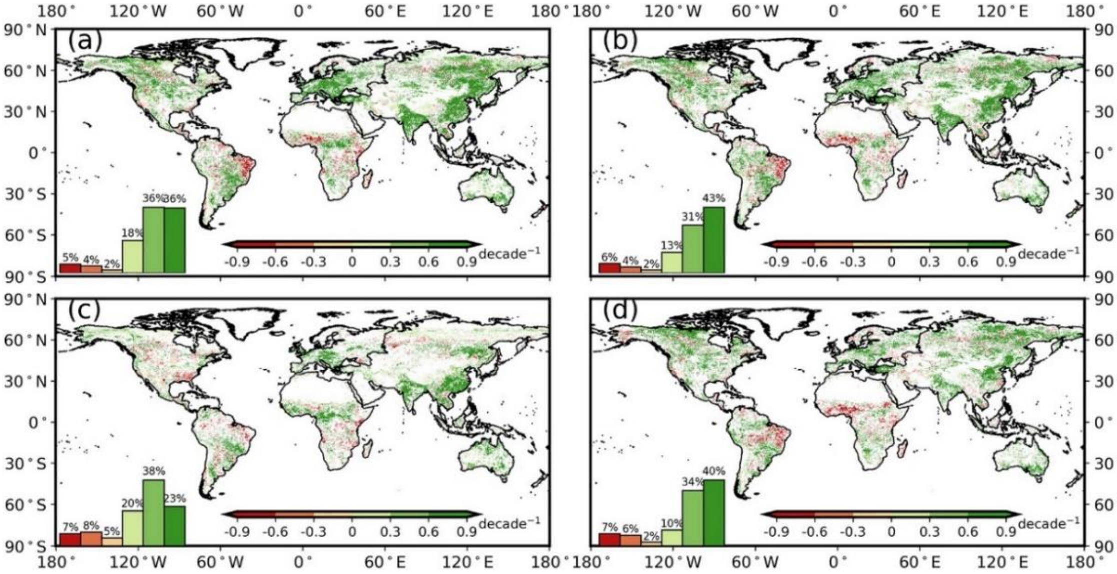

Figure 3: Maps of linear trends of LAI calculated from Moderate Resolution Imaging Spectroradiometer (MCD15A2H, C6) between 2001 and 2017. (a) shows yearly average. (b) growing season April to October, (c) December-January-February and (d) June-July-August. Histograms show the percentage of pixels for different trend values. Pixels with p 0.1 were excluded. Source: (Fang et al., 2019).

These changes in vegetation are caused by different drivers, which can be grouped under two categories: biogeochemical drivers and land-use related drivers. The biogeochemical drivers include regional effects of climate change (changes in precipitations, temperature and radiation), and fertilization effects due to increasing CO$_2$ concentration. Land-use related drivers include changes in land cover and land management, for example changes in irrigation and cultivation practices or changes in fertilization. Biogeochemical drivers are mainly responsible for the observed LAI increase at the global scale, while land-use drivers play a significant role at the regional scale. The vegetation change is the result of different interacting factors, but CO2 fertilization and climate change are the dominant ones. The former gives the biggest contribution to observed LAI trends, and it is the dominant driver over 23.2% of the global vegetated area, while the latter gives the main contribution to the greening trend over 28.4% of the area. The contribution of climate change to the change in LAI varies across different regions: at high latitudes and in the Tibetan plateau, the temperature increase contributes to enhanced photosynthetic activity and an increase in length of the growing season, while increasing precipitations are responsible for the greening in South America and in the Sahel region. Climate change can contribute to negative trends in LAI in some region, and its effects are not always consistent between models (Zhu et al., 2016).

1.6. LAI in numerical climate models

Numerical climate models are crucial for understanding and simulating the climate dynamics of Earth. They are used to investigate the response of the climate system to different forcing, to predict climate patterns over seasonal and decadal time scales and to forecast future climate changes. Many types of models are employed in climate science, ranging from more complex Earth System Models, which are the most advanced tool to simulate climate, to Regional Climate Models and simple conceptual models (Flato et al., 2013). Many climate models rely on parametrizations, which are simplified representations of chemical and physical processes, typically used to incorporate complex small-scale processes into the models.

Land Surface Models (LSMs) are key components of climate models, as they simulate fluxes of energy and water exchanged between Earth surface and atmosphere. In some land surface models, vegetation is parametrized using a LAI that does not vary seasonally, which causes an overestimation of LAI and soil moisture during atypically dry seasons. Overall, seasonally varying LAI presents a more realistic climatology.

In land surface models, the simulation of processes such as transpiration, energy absorption, and ecosystem productivity at interannual and seasonal scales can be improved with the integration of LAI observations from remote sensing datasets. The integration can be performed either through a simple direct forcing mode or through a more complex data assimilation mode.

In the direct forcing mode, remote sensing data is used as input data or as initial condition, to ensure more realistic model runs. On the other hand, the direct assimilation mode bounds the model to the satellite observations to improve the estimated variables, thus enhancing the modelling of water, energy and vegetation dynamics. The assimilation can be performed in different ways, but generally the best constraint is obtained from the estimated measurement errors and model forecast errors through an assimilation approach. This mode is based on the assumption that remotely sensed LAI has greater accuracy than the simulated one, and that uncertainties can be quantified. Errors in LAI products can however potentially propagate in model simulations (Fang et al., 2019).

2. The Planet Simulator and its dynamical vegetation module (SimBA)

2.1. Planet Simulator: an Earth system Model of Intermediate Complexity

The Planet Simulator (PlaSim) is a model of intermediate complexity that can be used to simulate the climate on Earth, Mars, and other planets (Universitat Hamburg, 2022).

As Global Climate Models are becoming increasingly more complex, Earth-system Models of Intermediate Complexity (EMICs) remain more attractive, given their ability to represent the climate system in a simplified way. EMICs allow to bridge the gap between simple conceptual models and more complex Global Climate Models, as they replicate the Earth system, along with almost all Earth components and their interactions, rather completely. With the increase in computational power, this class of models will advance in terms of resolution and complexity in the future (Shi et al., 2019).

Earth-system Models of Intermediate Complexity include many Earth system components, such as land, atmosphere, ocean, vegetation and cryosphere. Compared to numerical Global Climate Models (GCMs), Earth-system Models of Intermediate Complexity describe the interactions between climate component in a more simplified, parametrized form. Moreover, Earth-system Models of Intermediate Complexity have coarser resolution which allows to simulate longer time scales with significantly lower computational time. For these reasons, they have been used for methodological studies and to support scientists in understanding how specific processes work. For instance, PlaSim has been used for a wide variety of applications: it has been used to simulate exoplanetary atmospheres, to study past climatic conditions, such as the snowball Earth, and to investigate the global entropy budget (Angeloni et al., 2020; Lunkeit et al., 2011; Angeloni, 2022).

All EMICs include an atmosphere and an ocean module (either three-dimensional or zonally averaged), and a representation of sea ice in various degrees of complexity. Some EMICs may also include vegetation dynamics, an inland ice sheet module, carbon dynamics and atmospheric and oceanic chemistry (Angeloni, 2022).

The conceptual scheme of PlaSim and all its sub-components is shown in *Figure 4*. The core is a General Circulation Model: The Portable University Model of Atmosphere (PUMA). PUMA exchanges surface data with both sea components and land surface. It is based on moist primitive equations, namely divergence, vorticity, thermodynamic, continuity and hydrostatic equation, which represent the conservation of momentum, mass and energy. These equations are numerically solved in PlaSim using spectral methods. Along the vertical direction, terrain-following coordinates are used, and the equations are solved using finite-differences method (Angeloni et al., 2020; Fraedrich et al., 2009).

All the unresolved subgrid-scale processes and their impacts are incorporated in the model through different parametrizations, which are used in many models, from weather prediction to Earth system models (Gettelman, 2023). The parametrized processes in PlaSim are surface fluxes, shortwave and longwave radiations, clouds, oceanic vertical and horizontal diffusion among many others (Angeloni et al., 2020).

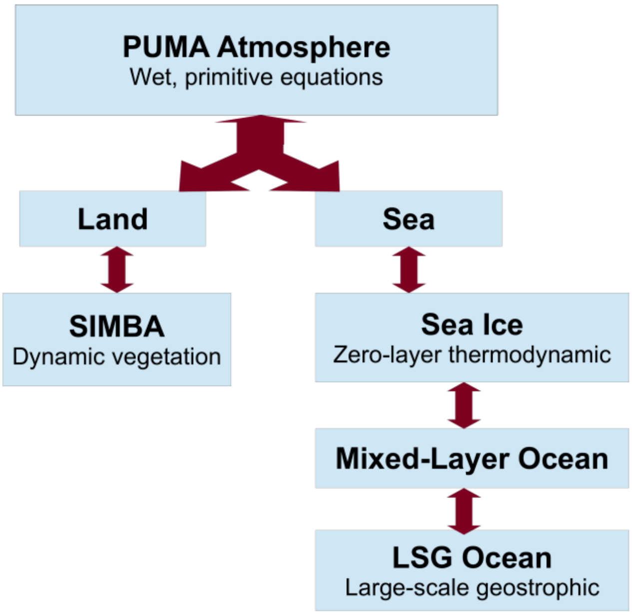

Figure 4: Scheme of PlaSim and all its sub-components. Source: (Andres & Tarasov, 2019).

In PlaSim, sea surface temperatures are simulated through a Mixed-Layer ocean model (ML) with constant thickness. This model is comprised of an equation that allows to calculate the oceanic temperature in each grid point, determined by the net atmospheric heat flux into the ocean. The oceanic transport and deep-water exchange are represented by the heat convergence at the base of the mixed layer, derived from climatology. Additionally, the horizontal and vertical diffusion terms in the temperature equation can be optionally switched on. The sea-ice is also present, and it can either be prescribed by climatology or simulated with a thermodynamic sea-ice module. The ice model allows to reduce incoming radiation from the atmosphere based on sea ice thickness, the resulting heat flux and wind stresses are then passed to the mixed-layer ocean model (Andres & Tarasov, 2019; Angeloni et al., 2020; Lunkeit et al., 2011).

The Large Scale Geostrophic (LSG) ocean circulation model was later implemented into PlaSim to introduce a representation of ocean circulation (Maier-Reimer et al., 1993). The model is built upon primitive equations in a three-dimensional system, including the continuity equation to depict conservation of water and salinity, the momentum equation and thermodynamic equation with salinity. PlaSim and LSG are coupled via exchange of surface fluxes for momentum, heat and freshwater, and the interpolation between atmospheric and ocean grid maintains the global conservation of water and energy (Angeloni et al., 2020).

Lastly, the land component allows to estimate land surface temperatures in 5 soil layers, using local energy balance. The runoff is included through a bucket depth approach. The bucket depth depends on vegetation; the excess water exits the cell through runoff and is transported to the ocean (Andres & Tarasov, 2019). A simple terrestrial global vegetation model, the Simulator for Biospheric Aspects (SimBA), is used in PlaSim. SimBA estimates changes in vegetation induced by surface atmospheric conditions, shortwave radiation, carbon dioxide concentration and other factors. The changes in vegetation, in turn, affect the climate (Lunkeit et al., 2011; Andres & Tarasov, 2019).

All physical processes are calculated in PlaSim on reduced Gaussian grids with resolutions of 5.6º and 2.8º, which correspond to T21 and T42 horizontal spectral resolutions. On the vertical dimension, the model is typically configured with 10 layers (Angeloni et al., 2020). The work in this thesis was carried out using a T21 resolution.

2.2. SimBA and its parametrization in PlaSim

As previously said, SimBA, which is derived from Kleidon (2006), is the simplified dynamic parametrization of terrestrial vegetation used in PlaSim. It allows to predict land surface properties that are impacted by dynamically changing vegetation, which is estimated from climatic conditions. The climate model simulates atmospheric and land surface conditions, which define the constraints for the Gross Primary Productivity (GPP) of vegetation. GPP is the rate of carbon absorbed by terrestrial vegetation through photosynthesis, also called gross carbon uptake, and it gives an indication of the amount of energy available for ecosystem functioning (Pandey et al., 2024; Xu & Chen, 2024; Kleidon, 2006). Gross Primary Productivity is the cause of biomass growth, and it defines the SimBA variable called Vegetative Biomass (GM), which is quite significant as it represents the amount of plant material present. The other three SimBA variables that define vegetation are forest cover, vegetation cover and leaf area index; these three variables depend on vegetation biomass and on other two global variables: soil moisture content (W_{soil}) and snow depth (z_{snow}) (Kleidon, 2006) (Lunkeit et al., 2011). The vegetation variables influence the climate through four land surface variables for non-glaciated grid cells, which are surface albedo (A), roughness length (z_0), surface conductance for the latent heat flux (C_w) and bucket depth for the soil (W_{max}) (Lunkeit et al., 2011). These consequently affect energy and mass exchanges with land surface in the climate model, which are calculated at every PlaSim time step (Kleidon, 2006).

The following subsections will give a description of the above-mentioned variables and their respective equations.

2.2.1. Vegetation Biomass (BM)

Vegetation Biomass, the main state variable in SimBA, is produced from the balance between carbon deposited through photosynthesis, which converts sunlight into sugars (Qin et al., 2018), and carbon released by respiration, which breaks down sugars to release energy used for plant growth and maintenance (Golovko & Garmash, 2022). The vegetative biomass (BM) in SimBA depends on the Net Primary Productivity (NPP) through *Equation 1*, which is a fundamental governing equation in the vegetation model.

$$\frac{\partial BM}{\partial t} = NPP - \frac{BM}{\tau_{veg}} \tag{1}$$

The Net Primary Productivity (NPP) is defined as the difference between GPP and the carbon lost by autotrophic respiration, and it is equal to the increment in biomass per unit surface and time (Chapin & Eviner, 2007). The model assumes NPP to be equal to $0.5 * GPP$, as 50% of GPP is used though respiration for maintenance. The biomass evolution is thus obtained from the balance between NPP and litter production, which is proportional to BM and characterized by a residence time (τ_{veg}) of 10 years (Lunkeit et al., 2011; Kleidon, 2006).

2.2.2. Gross Primary Production (GPP)

The Gross Primary Production is defined as the minimum between light-limited ($GPP_{light-limited}$) and water-limited ($GPP_{water-limited}$) rate, as shown in *Equation 2* (Lunkeit et al., 2011; Kleidon, 2006). Its unit of measure is generally mass per unit surface and time (Xu & Chen, 2024).

$$GPP = \min(GPP_{light-limited}, GPP_{water-limited}) \tag{2}$$

The light-limited rate, shown in *Equation 3,* is defined using a light-use efficiency approach.

$$GPP_{light-limited} = \epsilon_{\mathrm{luemax}} * \beta(\mathrm{CO_2}) * f(\mathrm{T_{sfc}}) * f\mathrm{PAR} * SW \downarrow \tag{3}$$

The light-limited rate depends on different variables:

- $\epsilon_{\mathrm{luemax}}$, the maximum light-use efficiency parameter, which is globally constant. It represents the light-use efficiency compared to the total shortwave radiation absorbed by the plant ($f\mathrm{PAR} * SW \downarrow$). It is equal to $3.4 * 10^{-10}\ kgC/J$.
- $\beta(\mathrm{CO_2})$ links productivity to CO_2 concentration in the atmosphere, and it accounts for the deviation from 360ppm. The rate of carbon dioxide assimilation is directly linked to its atmospheric concentration, and an increase in atmospheric concentration has been linked to an increase in plant and forest growth (Franks et al., 2012). This parameter accounts for the increase in productivity for increasing CO2 concentration.
- $f(\mathrm{T_s})$, where T_s is the surface temperature in degrees Celsius. This function accounts for the decrease in plant productivity for cold temperatures: its value is 0 when temperature decreases below 0°C, thus bringing the light-limited GPP to zero, while it is equal to 1 when temperature increases above 5°C, as shown in *Equation 4*.

$$f(\mathrm{T_s}) = \begin{cases} 0 & if\ T_s \leq 0°C \\ \dfrac{T_s}{5°C} & if\ \ 0°C \leq T_s \leq 5°C \\ 1 & if\ T_s \geq 0°C \end{cases} \tag{4}$$

- $f\mathrm{PAR}$ is the fraction of Photosynthetically Active Radiation (PAR) absorbed by the photosynthesizing parts of vegetation (the green leaves), where PAR is the fraction of solar radiation, between 400 and 700 nm, that can be used in photosynthesis (Qin et al., 2018). $f\mathrm{PAR}$ is a dimensionless number that varies between 0 and 1, based on how much PAR is absorbed by the vegetation. It is also referred to as vegetation cover (f_{veg}) and it can be approximated as a function of Leaf Area Index, as shown in *Equation 5,* where k_{veg} is the light extinction coefficient, equal to 0.5.

$$fPAR = 1 - e^{-k_{veg} * LAI} \tag{5}$$

- $SW \downarrow$, which is the downward flux of shortwave solar radiation absorbed at the surface. Its unit of measure is W/m^2.

The water-limited rate is defined through *Equation 6.* It follows a “big leaf” diffusivity approach, in which the canopy is treated as if it were a large single leaf coupled to the atmosphere, to neglect conductance at the leaf boundary layer.

$$GPP_{water-limited} = \frac{8.3 * 10^{-4} * P * f_{veg} * ET * 0.3 * co_2}{VPD} \tag{6}$$

The water-limited rate depends on different variables:

- P, which is atmospheric pressure in Pa.
- co_2, the atmospheric carbon dioxide concentration in ppmv.
- f_{veg}, the vegetation cover.
- ET, which is evapotranspiration in $m^3 * m^{-2} * s^{-1}$. Evaporation from both intercept water in the canopy and dry soil is neglected in the model, which assumes the evaporative flux on land to be strictly governed by vegetation.
- VPD, the water vapor pressure deficit between saturated leaf surface and atmosphere, in Pa.

The water limited rate increases with an increasing CO_2 concentration in the atmosphere, this is because high carbon dioxide availability causes the plant stomata (where carbon absorption happens) to partially close, thus limiting water losses (Franks et al., 2012). This consequently increases the plant water-use efficiency. On the other hand, the water limited rate decreases with the increase in the specific humidity gradient at the leaf-air boundary; an increase in VPD has been linked to a decrease in plant growth and photosynthetic rate, due to a decrease in stomata aperture to limit water losses (Du et al., 2018).

Table 1 summarizes the dependency of water and light limited rates.

Table 1: Summary of GPP dependency on different variables.

	Variable it depends upon	Brief description of the variable
$GPP_{light-limited}$	$\beta(\mathrm{CO_2})$	Function of atmospheric CO_2 concentration
	$f(\mathrm{T_{sfc}})$	Function of surface temperature
	$fPAR$	Fraction of PAR absorbed by leaves, equal to f_{veg}
	$SW\downarrow$	Shortwave radiation absorbed at surface
$GPP_{water-limited}$	f_{veg}	Vegetation cover
	ET	Evapotranspiration
	co_2	Atmospheric CO_2 concentration
	VPD	Vapor pressure deficit between leaf surface and atmosphere

Both water and light limited rate depend on the vegetation cover or $fPAR$, which is a function of LAI, as shown in *Equation 5*.

2.2.3. Vegetation in SimBA: LAI, forest cover and vegetation cover

Vegetation in PlaSim is described by different variables: vegetation biomass (BM), leaf area index (LAI), vegetation cover (f_{veg}) and forest cover (F) (Kleidon, 2006; Lunkeit et al., 2011).

Vegetation biomass is used to define both vegetation structure and Leaf Area Index, which accounts for the leaf display on land, and it is computed as a function of both biomass and soil water availability (Kleidon, 2006). The Leaf Area Index is also linked to vegetation cover through *Equation 5*. It is worth noting that changes in LAI produce changes in vegetation cover and vice versa.

LAI follows a drought-deciduous phenology. The term 'phenology' refers to intra-annual variations in LAI. Therefore, a drought-deciduous phenology indicates that the seasonal variations in LAI are exclusively controlled by water availability (Dahlin et al., 2015). Plants leaves desiccate under water-stress conditions; in plants adapted to droughts the leaf loss is a way to avoid water stress, as it reduces the transpiring surface on plants (Estiarte & Peñuelas, 2015). LAI does not follow a winter-deciduous phenology, which is the seasonal variation in LAI characterized by leaf fall in the winter, a process mainly controlled by temperature changes and light availability (Estiarte & Peñuelas, 2015; Fadón et al., 2020). The lack of multiple phenological patterns is a clear limitation of the LAI parametrization in SimBA. However, it allows to simplify the representation of vegetation and to neglect Plant Functional Types, which are not included in the model to represent vegetation. Leaf Area Index and Vegetation Biomass are used to compute vegetation cover and forest cover.

Vegetation cover (f_{veg}) is the fraction of land covered by green biomass i.e. leaves. It is a dimensionless variable, and it varies between 0 and 1. Vegetation cover is determined as the minimum between a water-limited value ($f_{veg,w}$) and a structurally limited value ($f_{veg,s}$).

The water-limited value depends on soil moisture content (W_{soil}) and the biomass-dependent soil bucket depth (W_{max}) as shown in *Equation 7*.

$$f_{veg,w} = \min\left(1, max\left(0, \frac{W_{soil}/W_{max}}{0.25}\right)\right. \tag{7}$$

The structurally limited vegetation cover is derived from a structurally limited maximum leaf area index (LAI_{m}), as shown in *Equation 8*.

$$f_{veg,s} = 1 - e^{-k_{veg} * LAI_m} \tag{8}$$

LAI_{m} depends on the amount of biomass (BM) available to sustain the leaves, as shown in *Equation 9*.

$$LAI_m = 0.1 + \frac{18}{\pi} * \arctan(0.25 * BM) \tag{9}$$

Forest cover (F) is fraction of soil covered by non-prostrate woody vegetation, which indicates the woody vegetation characterized by an upright structure, sticking out above the snowpack. Its parametrization depends both on biomass and on a biomass threshold above which the forest cover begins to rise above zero ($1\ kg * m^{-2}$).

2.2.4. Land surface variables: Surface roughness, albedo, conductance and soil water holding capacity

In PlaSim, simulations can be run with either an interactive or a non-interactive vegetation. In the interactive mode, the vegetation simulated through SimBA influences the climate via four land surface variables mentioned in section 2.2: surface roughness, surface albedo, surface conductance and soil water holding capacity. Conversely, when the non-interactive mode is used, the simulated vegetation does not influence the climate. This chapter will provide a description of the aforementioned land-surface variables.

Soil water holding capacity (W_{max}), also called soil bucket depth, is a measure of how much water can be held in soil at total saturation, and it is measured in meters (Koviessen et al., 2023; Lunkeit et al., 2011). The soil bucket depth is determined through a non-linear relationship with biomass, due to the non-liner dependence of an intermediate variable (V_{soil}) on biomass. The underlying idea is that the bucket depth increases with an increase in root biomass.

The linear relationship of soil water holding capacity with the intermediate variable is shown in *Equation 10*. As biomass increases, the V_{soil} increases and W_{max} increases as well. For interactive vegetation, the soil water holding capacity is a value that varies between 0.05 m and 0.5 m.

$$W_{max} = 0.5 * V_{soil} + 0.05 * (1 - V_{soil}) \tag{10}$$

The soil water holding capacity is linked to the soil water reservoir W_{max}, which is a variable that defines the quantity of water in the soil, measured in meters. The water in the soil is represented by a bucket model, a simplified description of the most important processes in the water cycle. The soil is represented by a bucket, which retains the water until its maximum capacity is reached. This model does not consider the precipitation intensity and how it influences infiltration rates (Romano et al., 2011). Soil water is increased by precipitations (P) and snow melt (M), and it decreases with surface evaporation (E_{surf}), as shown in *Equation 11.*

$$\frac{\partial W_{soil}}{\partial t} = P + M + E_{surf} \tag{11}$$

Soil water is limited by the soil water holding capacity. In the non-interactive mode, soil water holding capacity has a fixed value at each grid point, which is given to the model as a boundary condition

(Lunkeit et al., 2011). If the soil water exceeds the soil water holding capacity, the excess is converted into runoff, which is carried by rivers to the ocean.

The surface wetness, or surface conductance for the latent heat flux (C_w), is used to compute surface evaporation; it can be defined as the rate at which water vapor is transferred from the land surface to the atmosphere, measured in m/s (Kelliher et al., 1995). It depends on both soil water holding capacity and soil water reservoir through *Equation 12*.

$$C_w = \frac{W_{soil}}{0.25 * W_{max}} \tag{12}$$

In the SimBA parametrization, Surface conductance is directly proportional to:

- A water stress factor ($f_{veg,w}$), which accounts for low soil moisture content. This factor depends on the soil water holding capacity, as shown in *Equation 7*.
- A parameter accounting for surface conductance in non-water stress conditions, which is set to 1.

Surface conductance can vary between 0 and 1m; it is set to 1 when snow is present.

Surface roughness (z_0) is a measure of roughness at the surface and it is measured in meters. Surface roughness in SimBA is a non-linear combination between roughness due to orography ($z_{0,oro}$) and roughness due to vegetation ($z_{0,veg}$), which is a function of forest cover (F). The parametrization of $z_{0,veg}$ is shown in *Equation 13*.

$$z_{0,veg} = 2 * F + 0.05 * (1 - F) \tag{13}$$

As forest cover increases, roughness increases as well. The vegetation roughness varies between $0.05\,m$ in the absence of forest, and $2\,m$ in fully forested areas. In the non-interactive mode, vegetation roughness has a fixed value at each grid point, which is given to the model as a boundary condition.

Surface roughness for a grid cell is defined through *Equation 14*.

$$z_0 = \sqrt{z_{0,veg}^2 + z_{0,oro}^2} \tag{14}$$

Lastly, surface albedo is computed differently based on the presence of snow. In its parametrization, some dependencies are neglected; for example, its dependency on solar zenith angle and the dependence of bare soil albedo on moisture content are overlooked.

Snow-free albedo ($A_{snow-free}$) is calculated through *Equation 15.*

$$A_{snow-free} = A_{fully-leaved} * f_{veg} + A_{bare} * (1 - f_{veg}) \tag{15}$$

The snow free albedo is linearly dependent on vegetation cover (f_{veg}), which in turn depends on LAI through . In the non-interactive mode, when vegetation does not influence the climate, snow-free albedo is defined using the Leaf Area Index data that comes from observations, specifically the Land Surface Parameter dataset of the US Geological Survey (Lunkeit et al., 2011; Hagemann, 2002). The dataset provides 12 monthly mean fields of LAI, which means that albedo does not display interannual variability as vegetation changes in time, it only shows intra-annual monthly variations. On the other hand, albedo in the interactive mode is calculated from the SimBA simulated LAI, therefore it changes both seasonally and interannually, following the change in LAI.

Snow free albedo also depends on $A_{fully-leaved}$ and A_{bare}, which are two constant fields. The first stands for conditions of infinite LAI, while the second corresponds to zero LAI. Since snow-free albedo is solely dependent on vegetation cover and it is independent from forest cover, branches and stems are considered to have the same albedo as bare soil.

To parametrize albedo in the presence of snow, the grid cell is divided into a forest-covered and non-forest covered part. This reflects the decrease in albedo in snow covered areas due to the presence of forests (Bonan, 2008). As shown in *Equation 16,* albedo in snow covered areas is a linear combination of forest-covered albedo ($A_{snow,f}$) and non-forest covered albedo ($A_{snow,nf}$), and it depends on forest cover (F). When snow is present, non-forested but vegetated land acts the same as bare soil in terms of albedo.

$$A_{snow-covered} = A_{snow,f} * F + A_{snow,nf} * (1 - F) \tag{16}$$

The forest-covered albedo is given a constant value ($A_{snow,f} = 0.2$), which is independent from both surface temperatures and snow accumulation. The non-forest covered albedo is linearly dependent on deep snow albedo, function of temperature and snow depth, and non-forest covered snow-free albedo.

To summarize, *Figure 5* shows the dependency of the four land surface variables on vegetation variables (in dark green), global variables (blue), Gross Primary Production (in light green) and on other variables (grey).

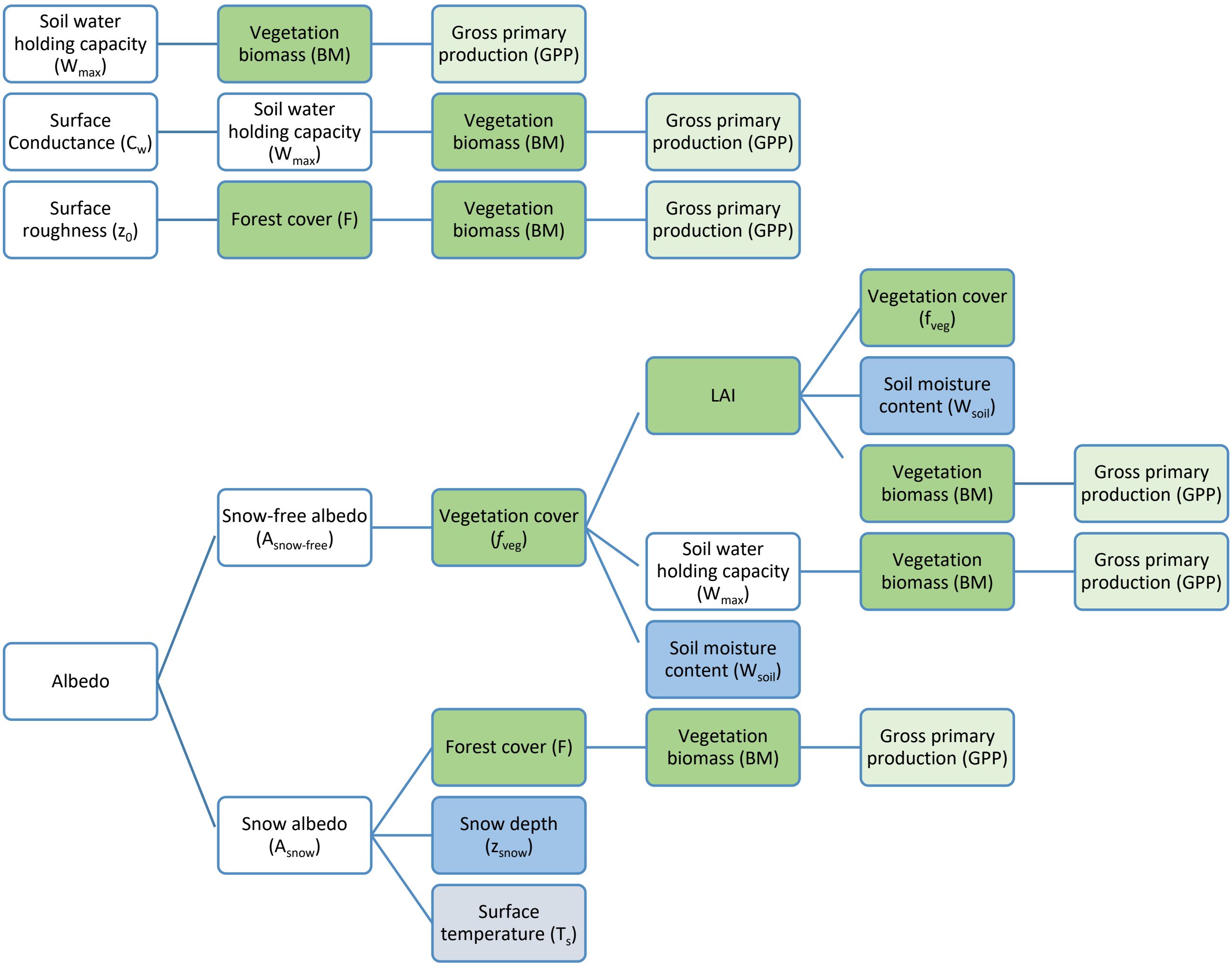

Figure 5: PlaSim dependency of land surface variables, which influence climate in the interactive vegetation mode.

2.3. Concluding remarks

This chapter describes the Planet Simulator, an Earth system Model of Intermediate Complexity, and SimBA, the simple terrestrial dynamic vegetation model embedded within the model. This description is necessary to provide the foundations necessary to explain the tuning applied to SimBA in the interactive vegetation mode, which is explained in detail in the following chapter. Tuning was necessary, as activating vegetation in the interactive mode with the default setup produced important biases compared to observations.

3. Tuning and validation of SimBA

In climate models, parametrizations are used to represent small-scale processes, either to reduce computational costs or, more importantly, because they are needed to simplify complex multi-scale processes. Parametrizations in SimBA have been extensively explained in *Chapter 2.2.* Each one consists of a set of equations that depend on parameters whose values are often poorly constrained by observations. Tuning is the process of estimating these parameters to reduce discrepancies between the real world, represented by observations, and the modelled one.

The classical definition of tuning, reported in (Hourdin et al., 2017) is the process of selecting parameter values to minimize, within an acceptable range, the deviation of the modelled climate from observations or theory.

The tuning process is often poorly detailed in literature; this is because it is often considered not worth recording, an unavoidable but flawed component of climate modelling, closer to the domain of engineering than to science, a way to compensates for errors in the model. Nonetheless, tuning is a significant part of the modelling process as it can be considered a scientifically based optimization procedure. It is also a way to improve the understanding of certain climate mechanisms. Moreover, tuning can compensate for errors or deficiencies in model formulations, which otherwise could remain unknown.

Climate model tuning is characterized by a certain degree of subjectivity, due to model complexity and to the different priorities each climate model has, for example groups focused on European climate may tune the model to prioritize a better representation of heat transport in the North Atlantic. Priorities and targets often vary based on the group objectives (Hourdin et al., 2017).

A survey was carried out in 2014 on 23 modelling groups involved in the Coupled Model Intercomparison Project (CMIP) to provide insights on how the tuning process was carried out (Hourdin et al., 2017). Tuning was generally performed by minimizing the bias of a decisive metric, which was generally either the globally averaged net top of the atmosphere flux or the mean global surface temperature. It often involved specific parametrizations, the most common were clouds in the atmosphere, snow and ice albedo, soil and vegetation properties. Atmospheric convection and cloud physics were thought to produce the largest biases.

Different tuning methods can be used, the simplest approach is the trial-and-error method, which consists of tuning one or two parameters at a time. The other option is the use of more complex objective methods, which fall under two categories:

- Optimization of a cost function, which quantifies the distance between model and observations to minimize the bias.
- A Bayesian approach, based on quantification of uncertainty sources.

These complex methods help make the tuning process reproducible, as they require the modeler to translate subjective judgment into formulas and numerical values, therefore creating an objective algorithm.

In this work, tuning was performed on the interactive vegetation mode of SimBA to improve the modelled climate. This procedure was necessary, since PlaSim was tuned to reproduce present day climate only with vegetation in the non-interactive mode. Activating vegetation in the interactive mode with the default setup produced a significantly lower mean global temperature compared to both observations and to the non-interactive vegetation mode. The biases will be explained further in *Chapter 3.1*.

The tuning method used in this work was relatively simple; it consisted of running six different simulations with changes in the snow-free albedo and in the soil water holding capacity parametrization. Some modelled variables were then compared to observations, specifically the ECMWF Reanalysis v5 (ERA5) dataset (European Centre for Medium-Range Weather Forecasts (ECMWF)). The variables considered were two-meter air temperature, precipitation, evaporation and leaf area index.

The simulations were performed with constant atmospheric CO_2 concentrations, equal to 354 ppm, while the reanalysis data considered were between the years 2005-2015. This choice aligns with the work carried out in (Angeloni, 2022), which focused on tuning the PlaSim-ML and the PlaSim-LSG configurations. A CO_2 concentration of 354 ppm was measured in 1990, while the concentrations between 2005 and 2015, were 380 ppm and 401 ppm respectively, with a value of 389 ppm in 2010 (Lan & Keeling). This discrepancy in CO2 concentrations between simulations and observations was necessary to ensure a valid comparison.

The current climate is characterized by a net radiative flux at the top of the atmosphere equal to 0.5 W/m^2 (Forster et al., 2021). To reach equilibrium, if the forcing is assumed to be constant, the surface temperature will increase, and energy will be released through longwave radiation (von Schuckmann et al., 2023); the net flux at the top of the atmosphere will eventually tend to zero. The increase in temperature due to current CO_2 concentrations will be observed in the future, and if present levels of CO_2 concentration were to be used in the simulations, the final simulated global temperature would be higher than observations of the same year.

The CO_2 concentration used in the simulations was determined through *Equation 17*, which expresses the change in forcing (F) as a function of the change in atmospheric CO_2 concentration. In the equation, C_0 represents the initial atmospheric concentration in ppm, to be used in the simulations, while C represents the final concentration that causes the increase in forcing (Myhre et al., 1998; Intergovernmental Panel on Climate Change (IPCC), 1990).

$$\Delta F = 5.35 * \ln\left(\frac{C}{C_0}\right) \tag{17}$$

The radiative forcing was set to 0.5 W/m^2, to correct the imbalance in the total heat flux at TOA. The considered value for C was 389 ppm, corresponding to the year 2010 (the central year of the observation interval); the resulting C_0 was equal to 354 ppm.

3.1. Need for tuning: bias between modelled and observed climate

Two 500-year simulations were initially run using SimBA in the interactive and in the non-interactive vegetation mode. The time series of globally averaged annual near-surface air temperature are shown in *Figure 6*. The blue line represents the non-interactive vegetation, while the orange line represents the interactive vegetation. These values are compared to the mean global temperature from ERA5 reanalysis averaged between 2005 and 2015, represented by the dashed black line. In both the interactive and non-interactive run, the globally average near-surface temperature stabilizes after about 300 years, when the system reaches equilibrium.

In the interactive mode, the simulated globally averaged temperature is colder than the temperature simulated in the non-interactive mode, which instead aligns with observations. The average temperature for non-interactive vegetation stabilizes around 287.5 K, whereas interactive vegetation stabilizes around 286.5 K, resulting in a 1 K difference between the two. This bias was corrected by tuning the snow-free albedo parametrization, as will be explained in *Chapter 3.2.*

A comparison between the modelled climate in the interactive and non-interactive modes was carried out to evaluate further discrepancies. Apart from the global average temperature, the climate in the two simulations was found to be qualitatively similar. However, two significant discrepancies were observed in the values of soil water holding capacity and in the collapses of LAI in specific grid points.

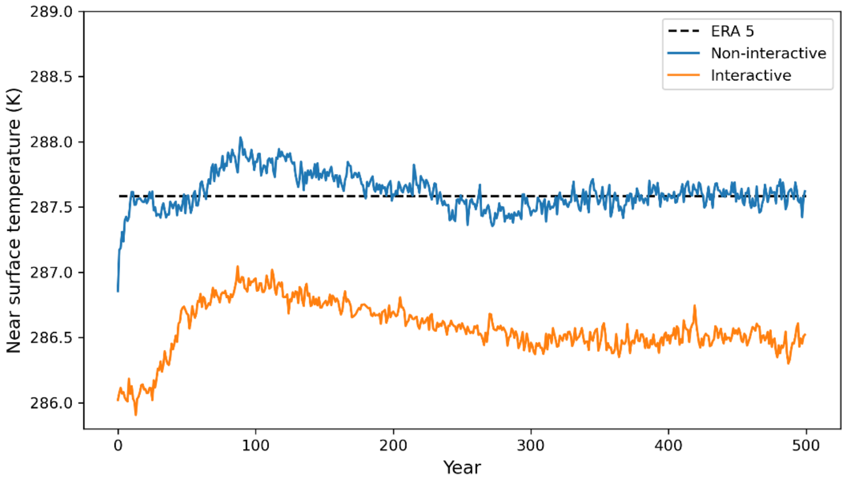

Figure 6: Time series of near-surface air temperature for simulations run with interactive (orange line) and non-interactive vegetation (blue line). The dotted black line represents near-surface air temperature from the ERA5 reanalysis dataset averaged between 2005 and 2015.

The difference in soil water holding capacity between interactive (VEG2) and non-interactive (VEG1) vegetation is shown in *Figure 7*. The map was obtained by averaging the last 50 years of simulations, after equilibrium had been reached. Except for limited areas in North America, the soil water holding capacity in the interactive vegetation mode was found to be lower everywhere. This bias was corrected by tuning the soil water holding capacity parametrization, which will be explained in *Chapter 3.3*.

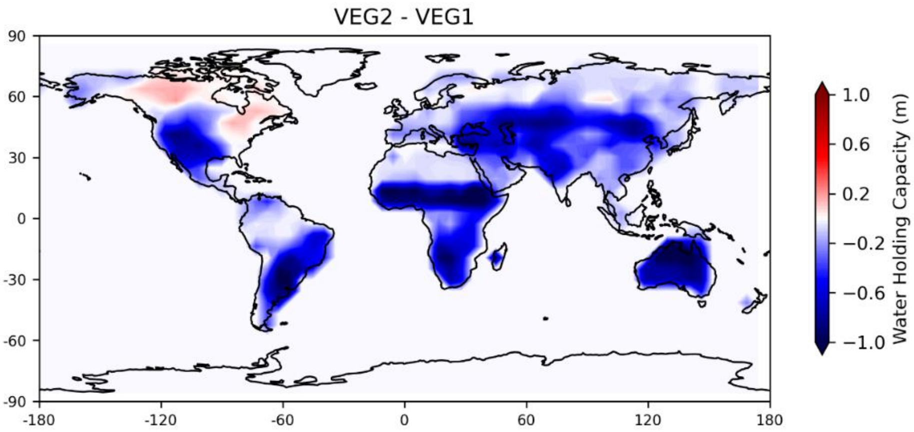

Figure 7: Anomaly in soil water holding capacity between Interactive (VEG2) and non-interacting vegetation (VEG1), both averaged over the last 50 years of simulations.

Moreover, the time series of LAI in the interactive vegetation mode shows collapses in specific grid points located in Europe and Amazonia, which in the non-interactive mode either do not happen or they are not as frequent. An example is shown in *Figure 8*, which represents the time series of yearly average LAI in two grid points: one in Europe, specifically in Poland, and one in Amazonia, specifically in Brazil. The LAI simulated in the interactive mode (orange line) displays collapses throughout the time series in both locations. These collapses do not happen in the non-interactive mode (blue line). This behaviour will be partially improved by tuning the soil water holding capacity parametrization.

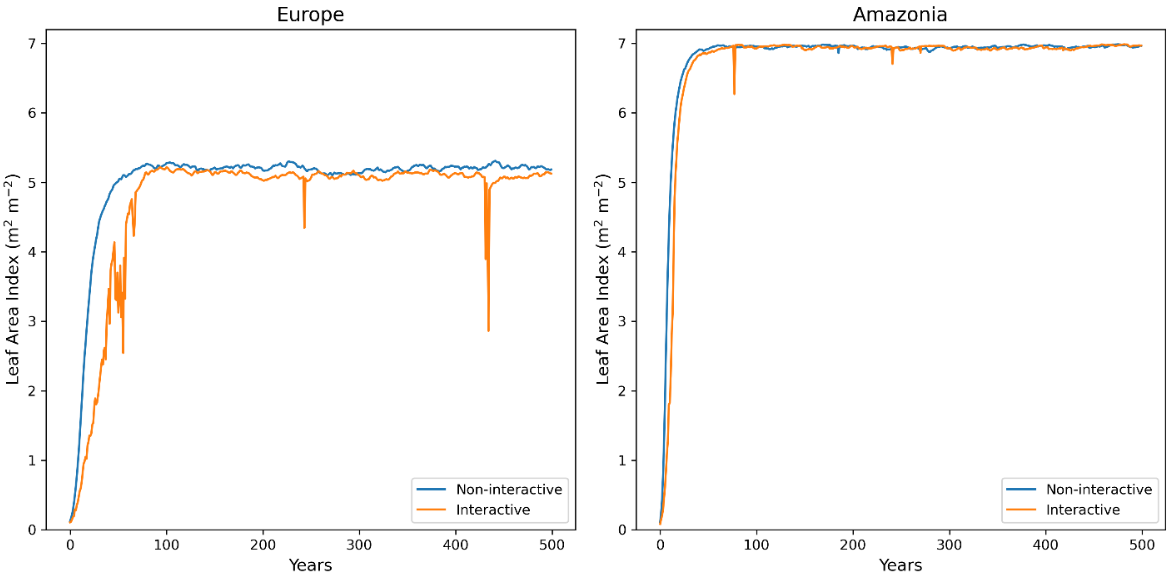

Figure 8: Time series of yearly average Leaf Area Index in two grid points. The coordinates are latitude 52.6°, longitude 16.9° in Europe and latitude -2.8°, longitude 298.1° in Amazonia.

3.2. Tuning of Snow-free albedo

As previously mentioned, tuning was performed by running six 500-year simulations with changes in parametrization of snow-free albedo and soil water holding capacity. The first parametrization considered was snow-free albedo.

Snow-free albedo is computed differently in the interactive and non-interactive vegetation mode:

- In the non-interactive mode, snow-free albedo varies between a minimum of 0.12 and a maximum of 0.2. The parametrization is shown in *Equation 18*.

$$A_{snow-free}(x,y) = A_{fully-leaved}(x,y) * f_{veg}(x,y) + A_{bare}(x,y) * (1 - f_{veg}(x,y)) \qquad (18)$$

In the non-interactive mode, the bare soil albedo and fully-leaved albedo are two fields that were obtained from MODIS satellite data between 2001 and 2004. Moreover, the value of albedo changes in space with vegetation cover (f_{veg}), which changes with the location. As explained in *Chapter 2.2.4*, snow free albedo in the non-interactive mode does not display interannual variability: since vegetation cover is estimated from a dataset of 12 LAI fields, albedo varies only with the simulated month.

- In the interactive mode, snow-free albedo varies between 0.12 and 0.3, which are the values of fully leaved and bare soil albedo, respectively. The parametrization is shown in *Equation 19*, with its dependency on space and time.

$$A_{snow-free}(x,y,t) = 0.12 * f_{veg}(x,y,t) + 0.3 * (1 - f_{veg}(x,y,t)) \qquad (19)$$

Snow-free albedo is a function of vegetation cover, which changes with simulated LAI. As opposed to non-interactive mode, interactive albedo displays both seasonal and interannual variation.

The discrepancy between the two albedo ranges explains why the globally averaged temperature in the interactive mode is lower compared to the non-interactive simulation (shown in *Figure 6*). Since the range of snow-free albedo in the interactive simulation is higher, the near-surface air temperature is lower.

Three 500-year simulations were run with lower values of bare soil albedo (A_{bare}) for interactive vegetation: 0.2, 0.23 and 0.25. The fourth 500-year simulation was run by replacing the fixed values with two spatially variable fields of bare soil albedo and fully-leaved albedo. This new parametrization of snow-free albedo, with explicit dependencies on space and time, is shown in *Equation 20.*

$$A_{snow-free}(x,y,t) = A_{fully-leaved}(x,y) * f_{veg}(x,y,t) + A_{bare}(x,y) * (1 - f_{veg}(x,y,t)) \qquad (20)$$

The bare soil albedo and fully-leaved albedo fields used in this parametrization were retrieved from a set of data available in PlaSim (listed with codes 1740 and 1741 respectively), which were obtained from MODIS satellite data of the years 2001-2004 (Lunkeit et al., 2011).

The time series of globally averaged annual snow-free albedo for the different simulations are shown in *Figure 9*, with a summary of the simulations provided in *Table 2*.

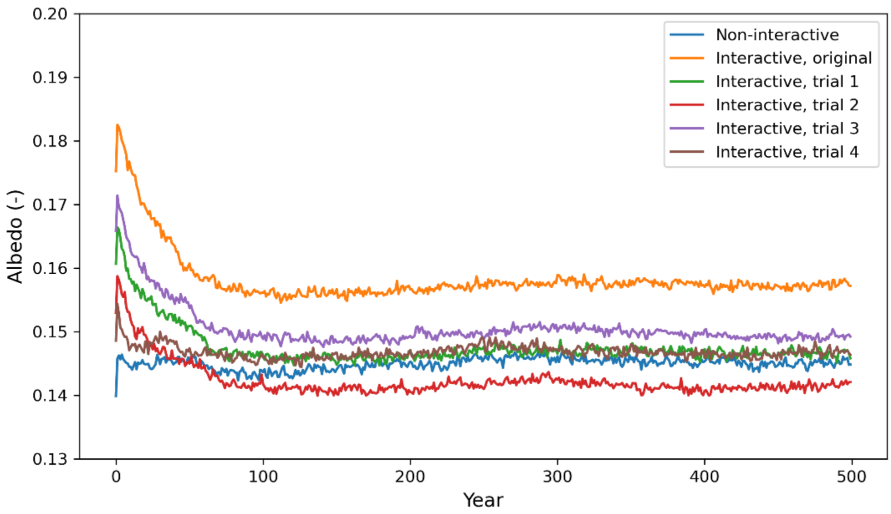

Figure 9: Time series for globally average albedo for simulations run with original interactive (orange) and non-interactive vegetation (blue), compared to simulations run with changes in parametrization of snow free albedo, explained in Table 2. The dotted black line is near surface temperature from the ERA5 reanalysis dataset.

Table 2: Description of simulations for tuning of snow-free albedo parametrization.

Simulation name	Description
Trial 1	$A_{bare} = 0.23$
Trial 2	$A_{bare} = 0.20$
Trial 3	$A_{bare} = 0.25$
Trial 4	$A_{fully-leaved}$ and A_{bare} are fields

Globally average albedo for the interactive original simulation (orange line) is higher than the non-interactive albedo (blue line). The first and fourth trials show a globally averaged albedo at equilibrium similar to the non-interactive value. The second trial shows lower values, while the third shows higher ones.

The time series of globally averaged near-surface air temperatures for the simulations, summarized in *Table 2*, are shown in *Figure 10*. The black dotted line represents the mean global temperature from observations.

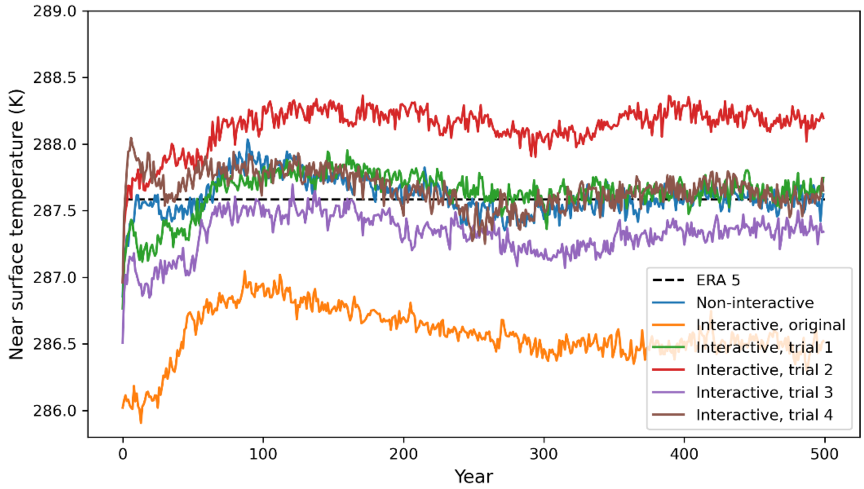

Figure 10: Time series for globally average yearly near surface temperature for simulations run with original interactive (orange) and non-interactive vegetation (blue), compared to simulations run with changes in parametrization of snow free albedo, explained in Table 2. The dotted black line is near surface temperature from the ERA5 reanalysis dataset.

The average near-surface air temperatures at equilibrium in the first and fourth trials are similar to both the observations and the non-interactive value. The second simulation run exhibits a temperature that is 0.5 K higher, while the third shows a temperature that is 0.25 K lower. These results are consistent with the remarks made on average global albedo.

Among all the runs, the first and fourth trials showed improved values for both average global temperature and albedo. Ultimately, the parametrization used in the fourth trial was the one selected, as it improved the simulated global average temperature, by improving the representation of albedo, while also implementing field values of bare soil and fully vegetated albedo, rather than reducing them to a single constant value for the whole domain.

3.3. Tuning of soil water holding capacity

The second parametrization to be tuned was the soil water holding capacity for interactive vegetation, which is the focus of this chapter. The goal was to obtain more realistic soil water holding capacity values compared to observations, while simultaneously improving the simulation of the climate.

The soil water holding capacity has different value ranges in the interactive and non-interactive modes:

- In the non-interactive mode, it varies between 0.001 m and 1 m, and it is derived from observations. Specifically, it is part of the Land Surface Parameter dataset of the US Geological Survey, identified by code 229 on the reference manual (Lunkeit et al., 2011; Hagemann, 2002).
- In the interactive mode, it ranges between 0.05 m and 0.5 m.

The parametrization in the interactive mode causes the soil water holding capacity to be lower compared to the observational data in most areas of the world, as shown in *Figure* 7. The interactive parametrization, shown in *Equation 21*, was therefore changed.

$$W_{max} = W_{max,max} * V_{soil} + 0.05 * (1 - V_{soil}) \tag{21}$$

$W_{max,max}$, which is the theoretical soil water holding capacity as biomass becomes infinitely large, was raised from the original value of 0.5 m to 1 m, and then to 1.5 m in two 500-year simulations. Both simulations were run with the tuned parametrization of snow free albedo. The ranges of soil water holding capacity used in the different simulations are summarized in *Table 3*.

Table 3: Soil water holding capacity ranges for different experimental configurations. The non-interactive range comes from observations, while the remaining three ranges are a result of different parametrizations.

Simulation	Range of soil water holding capacity values
Non - interactive	$W_{max} = (0.001\ m - 1\ m)$
Interactive, original parametrization of W_{max}	$W_{max} = (0.05\ m - 0.5\ m)$
Trial 1	$W_{max} = (0.05\ m - 1\ m)$
Trial 2	$W_{max} = (0.05\ m - 1.5\ m)$

Table 4 shows the mean global value of soil water holding capacity, averaged over the last 50 years of simulations, after reaching equilibrium. The second trial simulates a mean global value closer to observations, while the first trial simulates a slightly lower value.

Table 4: Average global values of soil water holding capacity for the different simulations.

Simulation	Average global soil water holding capacity
Non interactive	$W_{max} = 0.522\ m$
Trial 1	$W_{max} = 0.474\ m$
Trial 2	$W_{max} = 0.527\ m$

Figure 11 shows the anomaly in soil water holding capacity between the trials and the non-interactive simulation. Compared to the original parametrization, shown in *Figure 7*, both trials indicate an increase in soil water holding capacity in various places (mainly Europe, South-East Asia, the Amazon region and Canada). Moreover, while the first trial (map on the left) exhibits moderate regional anomalies, the second trial (map on the right) shows more pronounced anomalies in the same areas.

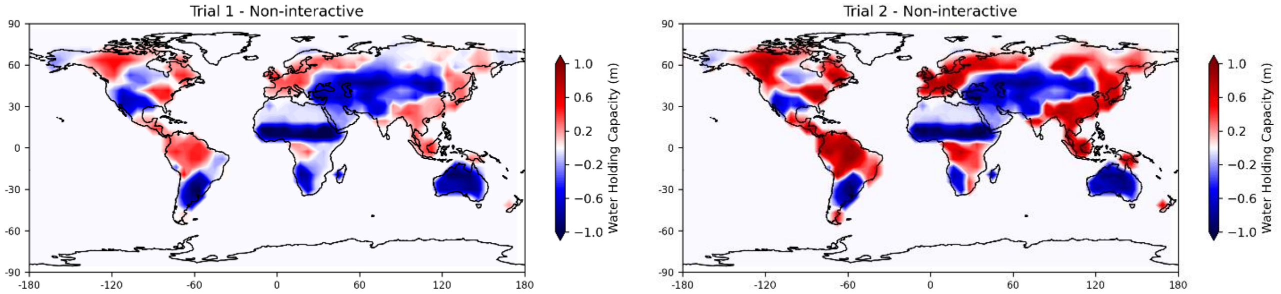

Trial 1 - Non-interactive

Trial 2 - Non-interactive

Figure 11: Anomaly in soil water holding capacity between interactive and non-interacting mode for Trial 1 (on the left) and Trial 2 (on the right), explained in Table 3. The values were averaged over the last 50 years of the simulation, after equilibrium was reached.

To choose the best soil water holding capacity parametrization, the bias between modelled climate and observations was evaluated as well. Overall, the change in parametrization did not significantly impact the simulated climatology.

The Root Mean Square Error (RMSE) was calculated for four climate variables on land: leaf area index, near-surface air temperature, evaporation and precipitation. The variables were evaluated on land because the changes in soil water holding capacity did not significantly influence their values on the ocean. The Root Mean Square Error was calculated using *Equation 22*, where y_k represents the observed values and $\hat{y}_k$ represents the simulated values at the position in space defined by k. The results are shown in *Table 5*.

$$RMSE = \sqrt{\frac{1}{n}\sum_{k=1}^{n}(y_k - \hat{y}_k)^2} \tag{22}$$

Table 5: Root Mean Squar Error on land for temperature, evaporation, precipitation and LAI, calculated for the two trials (see Table 3). The RMSE was calculated by considering the last 50 years of simulation, after equilibrium was reached.

Variable	RMSE
Temperature	$RMSE_{trial\ 1}$ =2.75
	$RMSE_{trial\ 2}$ =2.72
Evaporation	$RMSE_{trial\ 1}$ =0.59
	$RMSE_{trial\ 2}$ =0.60
Precipitation	$RMSE_{trial\ 1}$ =0.79
	$RMSE_{trial\ 2}$ =0.80
Leaf Area Index	$RMSE_{trial\ 1}$ =1.03
	$RMSE_{trial\ 2}$ =1.04

The RMSE for the first trial is lower than that of the second trial across all variables, except temperature. The difference in RMSE between the two trials is around 1% for all evaluated variables, meaning that the global difference between the two is minimal. Nonetheless, there are some regional differences between the two configurations; the most noticeable is a slight change in evaporation, temperature and precipitation over Russia, particularly during summer.

The chosen parametrization was the one used in trial 1, with the maximum value of soil water holding capacity set to 1 m. In this case, the regional variations of soil water holding capacity, shown in in *Figure 11,* are less extreme, although the mean global value is slightly smaller than observations. Overall, the difference in simulated climate variables did not significantly influence the decision, as the RMSE differences between the two trials was negligible.

It is interesting to note that, with tuning of the soil water holding capacity, the collapses in LAI in specific grid points discussed in *Chapter 3.1.* either do not occur or they are less frequent. This could be due to the changes in soil moisture caused by changes in soil water holding capacity. When the soil water holding capacity increases, which happens in both Amazonia and Europe (see *Figure 11*), the amount of water in the soil available for plants increases as well, since more water can be stored in the soil.

The plot in *Figure 12* shows the yearly LAI in two grid points, one in Europe and one in Amazonia, for the non-interactive (blue line), the original interactive (orange line) and the tuned interactive simulation (green line). In the tuned simulation, the collapses are not observed.

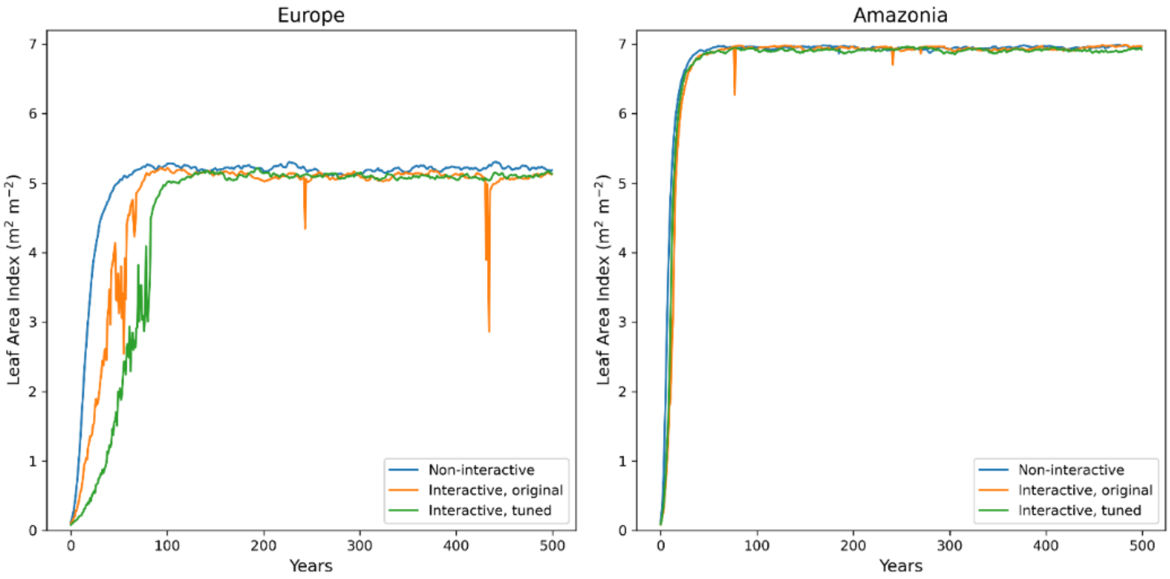

Figure 12: Time series of yearly average Leaf Area Index in two grid points. The coordinates are lat 52.6°, lon 16.9° in Europe and lat -2.8°, lon 298.1° in Amazonia

3.4. Modelled climate with tuned interactive vegetation and non-interactive vegetation

After tuning the model, the climate simulated with interactive vegetation was compared to both the non-interactive version and observations. The objective was to understand how the interactive vegetation affects the climate, and to analyse biases with observations. This section begins with a brief description of the data used for the analysis, followed by a comparison of the simulated climate at global and regional scales.

3.4.1. Description of the data

As previously mentioned, the observation data were retrieved from ECMWF Reanalysis v5 (ERA5), the dataset used was the monthly averaged data on single levels (Hersbach et al., 2023). Reanalysis combines data from models with observations from around the world, to create a comprehensive and consistent dataset that describes the state of the climate throughout the years.

The downloaded data consisted of the monthly average values of three variables:

- Two-meter temperature, which is the air temperature 2m above the surface.
- Total precipitation, which is the rate of precipitation on the Earth surface obtained as a sum of large-scale and convective precipitation.
- Evaporation, which is the water evaporated from Earth surface, including a simplified representation of plant transpiration.

The data was downloaded on a regular lat-lon grid with a resolution of 0.25 degrees. The datasets were then regridded to the PlaSim T21 grid, in order to produce meridional profiles and maps. As explained at the beginning of *Chapter 3*, the years considered for observations were 2005-2015.

The simulated climate from PlaSim was obtained by running two 500-year simulations: one with tuned interactive vegetation and one with non-interactive vegetation. As explained at the beginning of this chapter, the CO_2 concentration in the atmosphere was set to 354 ppm. The output, given as monthly averaged values, was produced on a T21 grid. The variables considered were two-meter temperature (var 167), convective precipitation (var 143), large scale precipitation (var 142), evaporation (var 182) and leaf area index (var 200).

3.4.2. Global simulated climate

Table 6 shows the global integral of total precipitation, evaporation and of the difference between total precipitation and evaporation.

Table 6: Global integral of total precipitation, evaporation, and of the difference between total precipitation and evaporation, averaged over the last 50 years of simulations, after stabilization was reached. The global integral for observations was calculated considering the years 2005-2015.

Dataset / Model	Precipitation (m^3/day)	Evaporation (m^3/day)	Precipitation-Evaporation (m^3/day)
ERA 5	$1.51 * 10^{12}$	$1.50 * 10^{12}$	$4.07 * 10^{9}$
PlaSim, non-interactive	$1.43 * 10^{12}$	$1.43 * 10^{12}$	$-3.36 * 10^{7}$
PlaSim, interactive tuned	$1.44 * 10^{12}$	$1.44 * 10^{12}$	$-2.65 * 10^{7}$

In terms of global integral, the interactive vegetation does not produce significant changes compared to non-interactive vegetation: the discrepancies in both evaporation and precipitation between the two configurations (second and third row in the table) are lower than 1%.

The water cycle is the main source of uncertainties in both observations and climate models, therefore an accurate representation of the water cycle is crucial (Liepert & Previdi, 2012). The global integral of precipitation and evaporation is an important indicator of how well the model simulates the global water balance. At equilibrium, precipitation must be approximately equal to evaporation, as water cannot continuously accumulate in the atmosphere. Likewise, there cannot be a persistent excess of precipitation over evaporation. As shown in *Table 6*, the differences between total precipitation and evaporation (last column on the right) are small compared to the global integral of precipitation. Specifically, this difference is less than 1% of total precipitation in PlaSim simulations and about 0.27% in observations. This suggests that the model simulates the water cycle reasonably well, as the quantities are largely balanced. Moreover, the simulated global integrals of total precipitation and evaporation, in both interactive and non-interactive modes closely match observed estimates, reinforcing PlaSim ability to represent the large-scale hydrological cycle effectively.

The meridional profiles of total precipitation, evaporation, temperature and the difference between precipitation and evaporation over both land and ocean are shown in *Figure 13*.

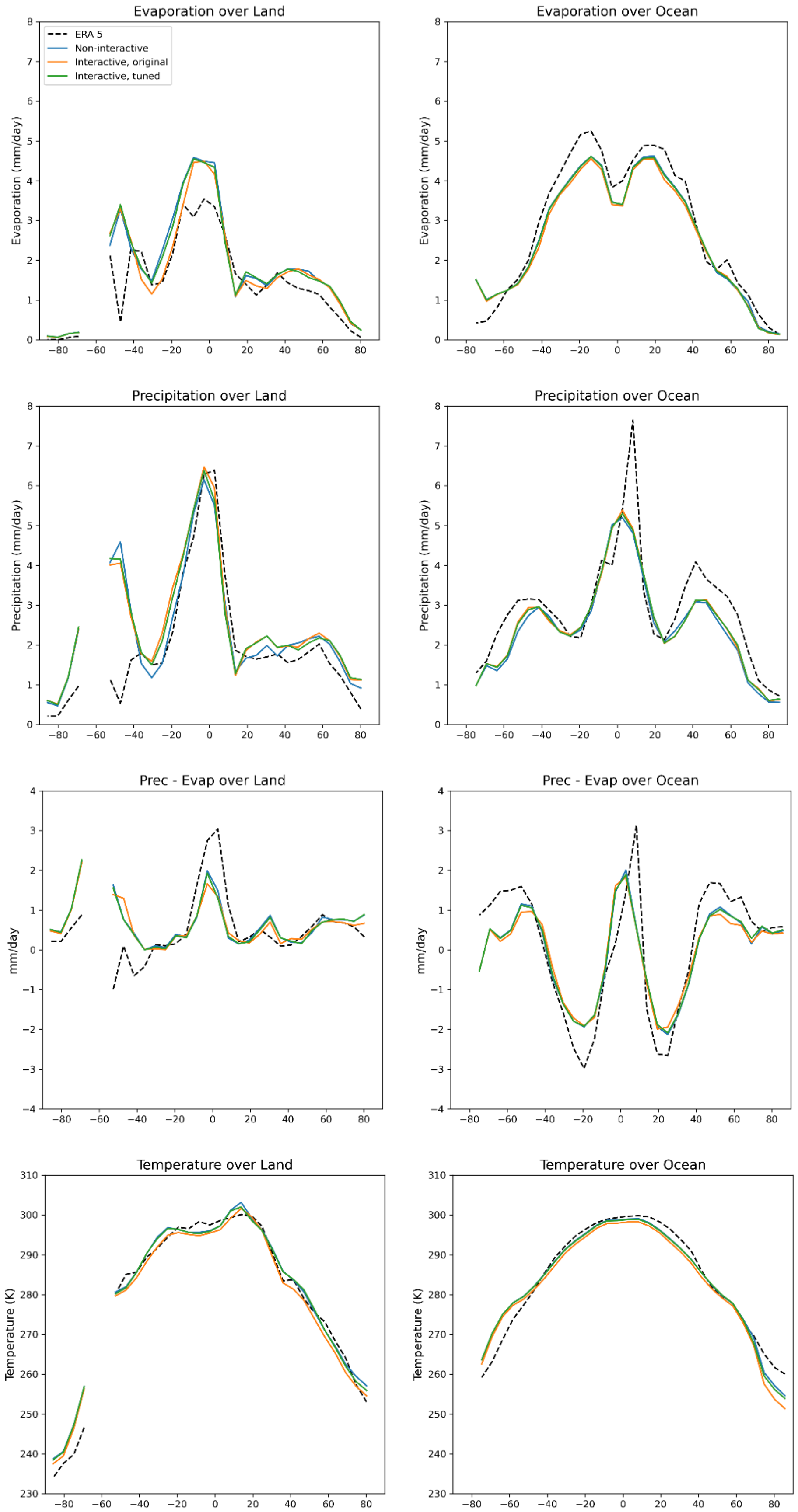

Figure 13: Meridional profiles of evaporation, precipitation, the difference between precipitation and evaporation, and near-surface air temperature. The black dotted lines represent observations, the blue lines represent the non-interactive simulation, orange lines represent the original interactive simulation, and the

green lines represent the tuned interactive simulation. They were all obtained by averaging the last 50 years of simulation, while observations were averaged over the years 2005-2015.

The plot shows meridional profile of observations (black lines) and simulations for non-interactive vegetation (blue lines), original interactive vegetation (orange lines) and tuned interactive vegetation (green lines).

As previously said, the tuning of interactive parametrization did not significantly change the global simulated climate: there is no significant difference between the tuned and original interactive parametrization (green and orange lines). Moreover, an interactive vegetation does not significantly alter the global simulated climate, although there are some differences in precipitation and evaporation in specific regions, which will be better discussed in the next chapter. The meridional profiles on the ocean are not significantly altered by an interactive vegetation, as vegetation mainly influence precipitation and evaporation on land.

It is important to note that between latitudes of -60 and -40, oceans dominate over land, which could explain the high bias over land in this region for precipitation and evaporation.

The biases of the modelled climate compared to observations vary across different variables:

- Evaporation over land is overestimated, with the highest bias below the equator, in the tropical regions of the Southern Hemisphere, and another lower bias at mid-latitudes in the Northern Hemisphere. Conversely, evaporation on the ocean is underestimated.
- The meridional profile of simulated precipitation matches observations, especially over land, where a slight positive bias can be observed at mid and high latitudes in the Northern Hemisphere. Over the ocean, precipitation is slightly underestimated, but the general behaviour is as expected, with the highest peak at the equator and two smaller peaks at mid latitudes, due to global atmospheric circulation.
- The difference between precipitation and evaporation is generally consistent with observations. The simulated climate shows a similar profile to observations: there is a positive peak over the ocean at the equator, where precipitation exceeds evaporation, and negative values in subtropical regions, where evaporation prevails.
- Meridional profile of near-surface air temperature is generally well represented, although there are biases up to 5 K over the ocean at high latitudes, where the simulated temperature is underestimated in the Northern Hemisphere and overestimated in the Southern Hemisphere.

3.4.3. Regional changes in the simulated climate

Regional changes in LAI, near-surface air temperature, precipitation and evaporation due to interactive vegetation will be discussed in this section, through different maps. *Figure 14* shows the average annual, summer (June-July-August) and winter (December-January-February) anomaly between the tuned interactive vegetation and the non-interactive vegetation.

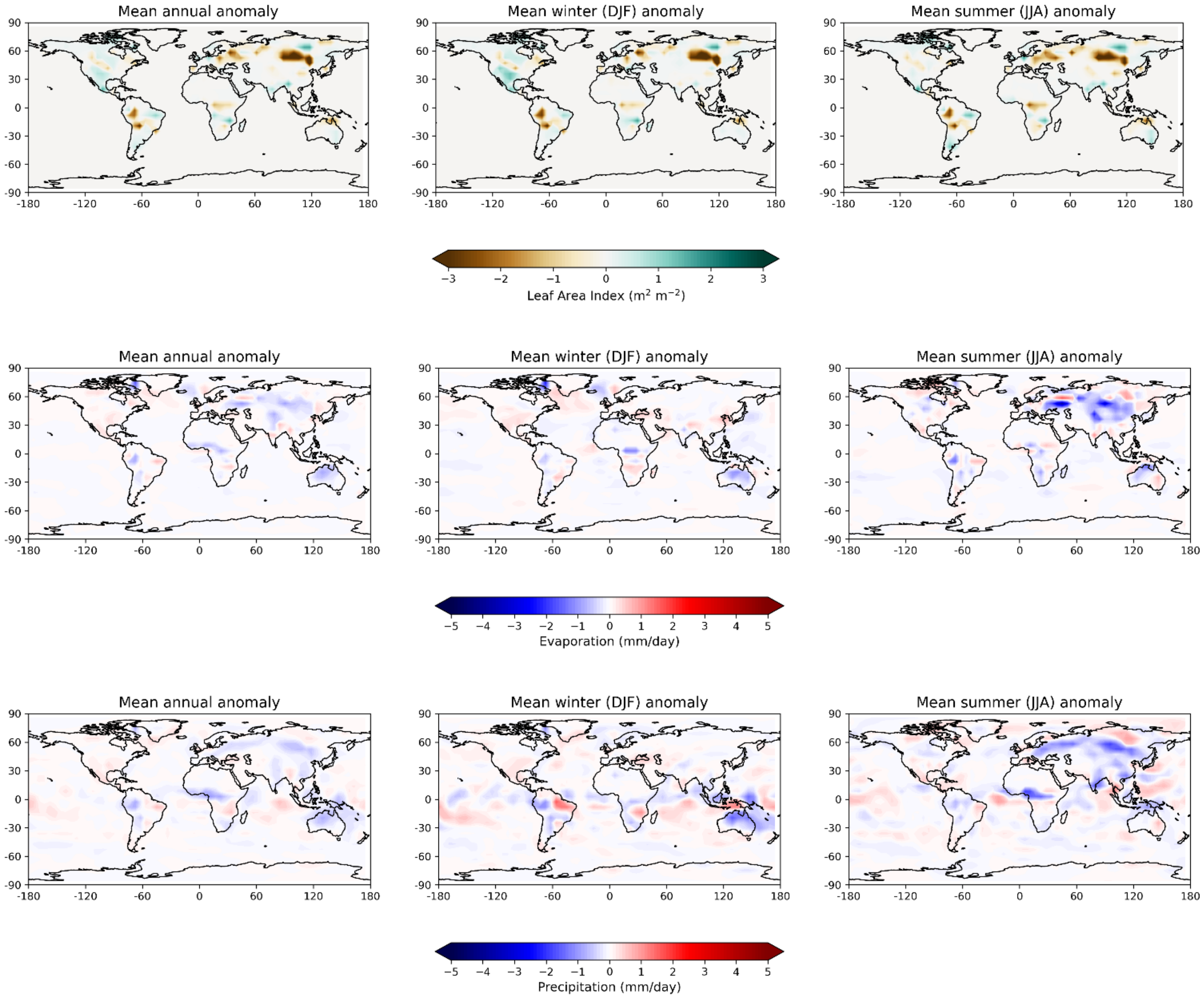

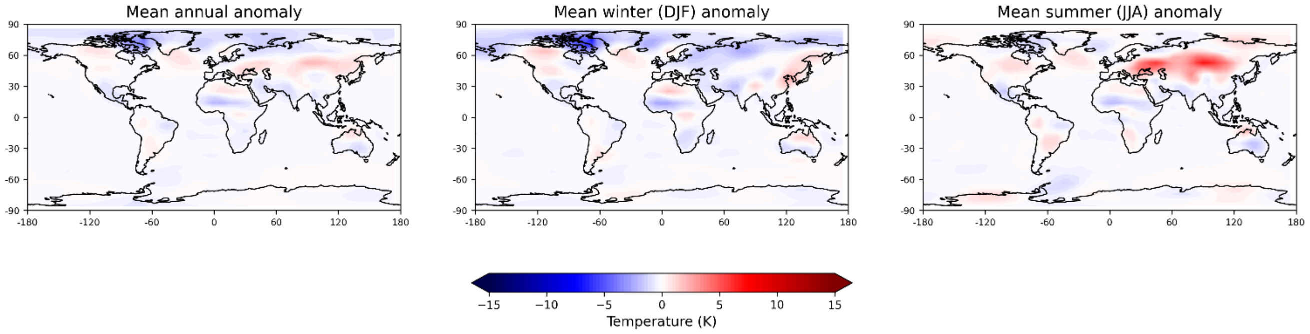

Figure 14: Annual, winter and summer anomalies between tuned interactive vegetation and non-interactive vegetation for leaf area index, evaporation, precipitation and near-surface air temperature. The maps were obtained by averaging the last 50 years of simulation, after equilibrium was reached.

Interactive vegetation produces regional changes in LAI. These changes are localized in specific areas: North-East Asia, mainly Russia, and South America experience the highest decrease in LAI, around 70% of the non-interactive value. A moderate increase is observed in North and Central America, as well as in the eastern parts of South America. The variation is mostly constant throughout the seasons, especially in the Southern Hemisphere; in the Northern Hemisphere, seasonal variations are slightly higher, although still modest, with greater negative variations. The moderate seasonal variation in LAI is due to the absence of winter deciduous phenology, and to the dependency of LAI on biomass, which is characterized by a long response time (the residence time is 10 years, as shown in *Equation 1)*.

Overall, most regions show moderate to low anomalies in evaporation. The anomalies are mostly localized in specific regions, and they mainly happen on land. Moreover, the highest variation in evaporation happens during the summer months, while winter months show weaker anomalies.

A reduction in evaporation is observed in regions where LAI shows a decrease, this phenomenon can be observed especially in South America, central Africa and Central Asia, with the highest evaporation anomaly observed in Central Asia during summer.

Variations in precipitation due to interactive vegetation have a strong seasonality, and anomalies on the ocean are higher for precipitation than for evaporation. Moreover, the anomalies on land are localized in the same regions of evaporation anomalies, and they generally increase were evaporation increases and decrease where evaporation decreases. Similarly to evaporation, the largest anomaly occurs is in Central Asia during the summer, where a decrease in precipitation is observed. Overall, precipitation and evaporation are strongly linked to leaf area index, and where leaf area index changes, evaporation and precipitation change as well. We can conclude that an interactive vegetation induces changes in the hydrological cycle, which are linked to changes in LAI. Areas where precipitation decreases are characterized by a reduction in evaporation, and the lower amount of water in the soil likely produces a decrease in leaf area index. It is also important to note that changes in LAI also affect the Gross Primary Production, which in turn affects the climate through the four land surface variables explained in *Chapter 2.2.4.* Therefore, precipitation and evaporation are influenced by LAI changes in return.

The last row in *Figure 14* shows anomalies in temperature, the highest variations are observed in the Northern Hemisphere. Temperature decreases at high latitudes especially during the winter. A strong positive anomaly is observed during the summer in central Asia, where LAI shows a decrease. It can be noted that the locations with a negative anomaly in LAI generally experience a positive anomaly in temperature, and vice versa.

Figure 15 shows the bias between non-interactive vegetation and observations. Using these maps, we can assess whether the interactive vegetation (in *Figure 14*) improves or worsens the original bias. The variables in both *Figure 14* and *Figure 15* use the same scale, to allow visual comparison.

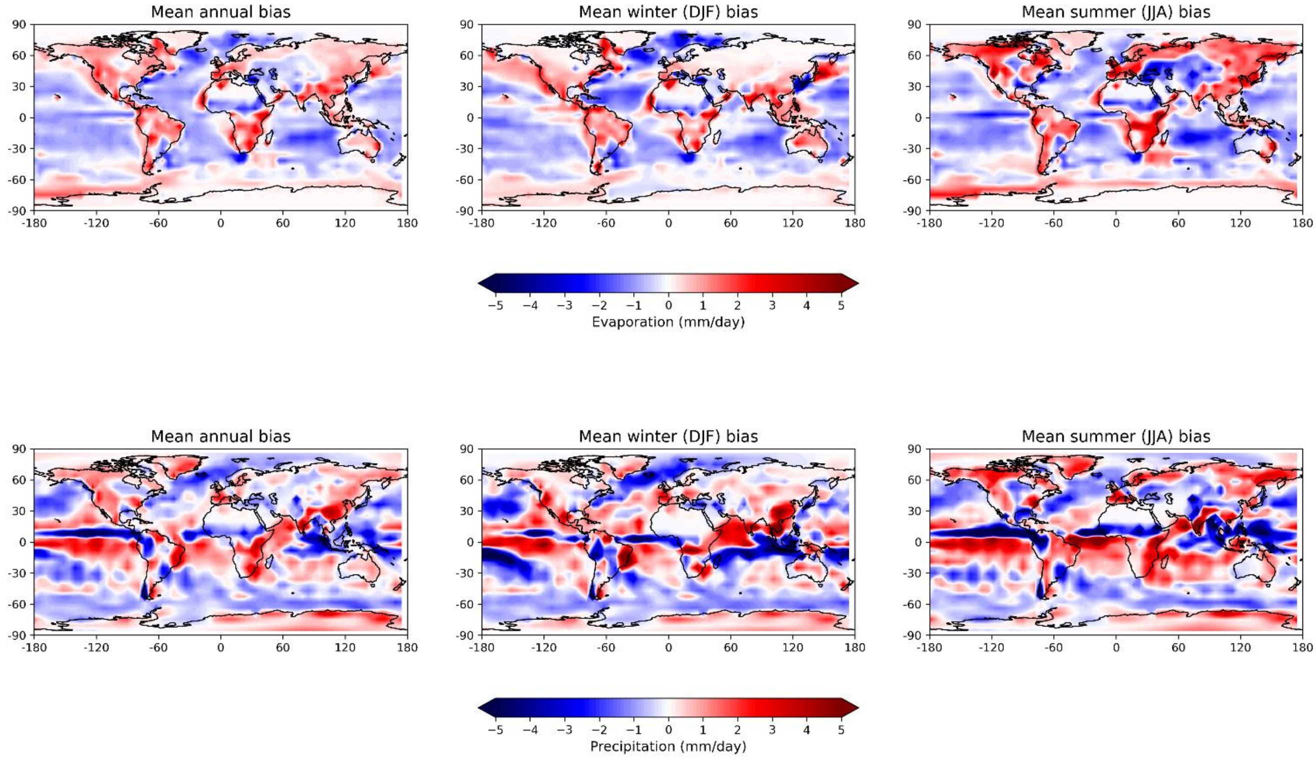

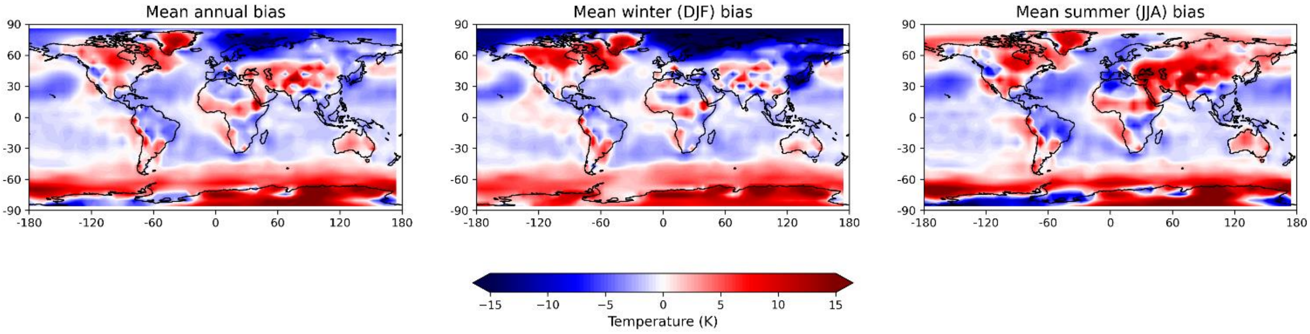

Figure 15: Annual, winter and summer bias between non-interactive vegetation and observations for evaporation, precipitation and near-surface air temperature. The values of non-interactive vegetation were obtained by averaging the last 50 years of simulation, after equilibrium was reached, while observations were averaged between 2005 and 2015.

The anomalies in evaporation, precipitation and near-surface temperature induced by interactive vegetation are much lower than the bias with observations. Therefore, an interactive vegetation cannot significantly impact these biases. In *Figure 15,* evaporation, precipitation and near-surface temperature present important regional bias with observations, while at the global scale the biases are quite low, as shown in *Chapter 3.4.2*.

Evaporation, shown in the first row of *Figure 15*, exhibits a systematic overestimation over land, particularly in the tropical regions south of the equator and at high latitudes in the Northern Hemisphere. Conversely, underestimations are prominent over oceans, as observed in *Figure 13*.

By comparing evaporation in *Figure 14* and *Figure 15*, it is evident that interactive vegetation slightly reduces the bias in some areas, such as Central Asia, Australia, and the western parts of South America, while it slightly increases the bias in North America.

Precipitation, in the second row, shows the highest negative bias in the intertropical convergence zone, a low-pressure band located around the equator, where trade winds converge. The bias is particularly high during summer. A negative bias is also observed at mid-latitudes, especially over the ocean. Interactive vegetation improves the bias over Australia and Central Asia, while it generally exacerbates biases at the tropics, particularly in South America and Africa.

Near surface air temperature show generally cold biases over the ocean, and warm biases over land areas, with strong seasonal variations. These biases are higher in polar regions at high latitudes, with a cold bias in the Northern Hemisphere and a warm bias in the Southern Hemisphere. Interactive vegetation mainly influences biases over land, while near-surface temperature over the ocean remains mostly unchanged. In general, the interactive vegetation reduces biases over land by decreasing the warm bias in Canada and Australia and mitigating the bias over the Sahara Desert. However, some exceptions are observed: interactive vegetation exacerbates the warm bias over Central Asia, particularly during the winter, and the cold bias over Northern Europe and Russia.

Overall, interactive vegetation leads to slightly lower biases in evaporation and temperature, particularly in certain regions of the Earth, although some areas experience worse bias. The main changes in evaporation, precipitation and temperature were observed in Russia, where an interacting vegetation, which led to a decrease in LAI, increases the warm temperature bias and corrects the precipitation bias, particularly during summer. The interactive vegetation improved the evaporation bias on the eastern areas of Asia, while worsening it in the west.

3.5. Concluding remarks

This chapter provided an in-depth explanation of the tuning process applied to the interactive vegetation mode. The parametrizations of both snow-free albedo and soil water holding capacity were adjusted. Specifically, the snow-free albedo parametrization was modified to substitute $A_{\text{fully-leaved}}$ and A_{bare} with two fields retrieved from MODIS observations, instead of using constants. Tuning improved the representation of the climate system, particularly global average temperature and soil moisture, which in turn mainly affects the water cycle, precipitation and evaporation.

An analysis of the simulated climate was then carried out to evaluate the changes in the climate induced by an interactive vegetation, compared to a non-interactive one, and to assess the bias with observations. To summarize, compared to a non-interactive vegetation, an interactive one:

- Does not significantly alter global climatology, as meridional profiles (*Figure 13*), global average near-surface air temperature and global integrals of evaporation and precipitation (*Table 6*) remain nearly unchanged.
- Induces regional changes in leaf area index, evaporation, precipitation and near-surface temperature (*Figure 14*). The changes in temperature, precipitation and evaporation are primarily observed in specific regions of the Earth, mainly on land, where the LAI is also varying. The highest variations were observed in Central Asia, where a decrease in LAI is accompanied by a decrease in precipitation and evaporation, which indicates a change in the water cycle, and an increase in temperature, especially during the summer. Changes in temperature are also noticeable over the North Pole, especially in winter.

The biases of the simulated climate with observations can be summarized as follows:

- At the global scale, the global average temperature is well represented. The water balance is also represented reasonably well, as the global integrals of evaporation and precipitation match (*Table 6*). The meridional profiles (*Figure 13*) are generally similar to observations, although evaporation is overestimated over land and consequently underestimated over ocean. Precipitation is also underestimated over the ocean, while the meridional profile of temperature aligns with observations, except for biases at high latitudes.

- Regional biases in evaporation, precipitation and near-surface temperature exhibit complex patterns. As previously mentioned, evaporation is underestimated over the ocean and overestimated over land, although negative biases are observed in some land regions, like Central Asia. A negative precipitation bias is observed over the ocean in the intertropical convergence zone, especially in the summer, and at mid latitudes. The most pronounced temperature bias is observed at high latitudes, with strong cold bias at the Northern Hemisphere, which is exacerbated by interactive vegetation, and a strong warm bias in the Southern Hemisphere. Overall, interactive vegetation does not significantly alter the biases, as the changes are significantly lower than the biases.

4. Comparison of LAI simulated by PlaSim-SimBA with CMIP6 ensemble and observational benchmarks

Evaluating the vegetation simulated in PlaSim is essential to assess potential shortcomings and limitations of the model. For this reason, the vegetation simulated through PlaSim was compared to that of more complex models, specifically four Earth System Models (ESMs) involved in the sixth phase of the Coupled Model Intercomparison Project (CMIP6). Additionally, these simulated vegetation outputs were compared to observations derived from both satellite data and ECMWF Reanalysis v5, which served as a benchmarks. The goal of this comparison was to assess the ability of PlaSim to simulate vegetation in comparison to observation and to evaluate its performance against more complex models. The analysis was carried out both at global level and in two specific regions: Europe and Amazonia.

As previously mentioned, vegetation in PlaSim is represented through different variables (leaf area index, forest cover, vegetation cover and biomass). However, the variable considered in the comparison was the leaf area index (LAI) which, as explained in the first chapter, is a key indicator for vegetation. It is one of the main variables used for modelling forest growth and it is used in many ESMs to represent both canopy and vegetation structures.

In this chapter, the LAI was evaluated by comparing the global average, spatial distribution, interannual variability and seasonal cycle. The interannual variability was assessed in the two regions, while seasonal cycle was analysed both in these regions and at the hemispheric levels.

4.1. Data description

This section will provide a brief description of the datasets used for the analysis, including how vegetation, evaluated through LAI, is simulated in different CMIP6 models, with a focus on phonology and plant functional types.

4.1.1. Satellite data

The satellite dataset used in this analysis is the fourth generation GIMMS Leaf Area Index product (GIMMS LAI4g), version 1.2 (Cao et al., 2023). The dataset was derived from Advanced Very High

Resolution Radiometer (AVHRR), which offers the longest available time record of data, starting in the early 1980’s. This database was produced using machine learning models built upon NDVI product and high-quality Landsat LAI samples, while the data consolidation method was based on reprocessed MODIS data. This allowed to solve major uncertainties in global LAI products: AVHRR sensor degradation, orbital drift and insufficient LAI reference to build robust LAI data, particularly prior to the late 1990’s.

The dataset exhibits overall high accuracy and minimal underestimation, compared to its predecessor (GIMMS LAI3g) and the other two mainstream datasets (GLASS and GLOBMAP). It also ensures consistent trends before and after the year 2000, allowing long-term assessment (Cao et al., 2023).

The dataset provides LAI values with 15-day temporal frequency and 1/12º spatial resolution. These data were averaged monthly and converted to 1º spatial resolution through bilinear interpolation, to match the other datasets. The time period considered for the analysis was 1980-2014.

4.1.2. Reanalysis data

A second benchmark for the comparison was obtained from ECMWF Reanalysis v5 (ERA5), the dataset consists of monthly averaged data on single levels (Hersbach et al., 2023). Since LAI is not directly provided, it was derived from four variables:

- Leaf area index for high vegetation (LAI_{high}), which represents half the total leaf surface area present over an area of land classified as high. High vegetation consists of evergreen trees, forests and deciduous trees. These values were estimated from daily satellite data.
- Leaf area index for low vegetation (LAI_{low}), which represents half the total leaf surface present over an area of land classified as low. Low vegetation consists of crops, short and tall grass, tundra, evergreen and deciduous shrubs. These values were estimated from daily satellite data.
- High vegetation cover ($f_{veg,high}$), which is the fraction of the grid box covered with high vegetation. It varies from 0 to 1 and it is constant in time.
- Low vegetation cover ($f_{veg,low}$), which is the fraction of the grid box covered with low vegetation. It varies from 0 to 1 and it is constant in time.

The total LAI was estimated using *Equation 23* as a function of the aforementioned variables (Duveiller et al., 2023).

$$LAI = LAI_{low} * f_{veg,low} + LAI_{high} * f_{veg,high} \tag{23}$$

The main issue with the reanalysis dataset is that LAI is prescribed at the grid cell level, following a fixed seasonal cycle based on satellite information. As a result, since high and low vegetation cover are fixed in time, LAI exclusively represents the monthly climatology. Inter-annual variability is not captured, while seasonal variability is (European Centre for Medium-Range Weather Forecasts (ECMWF), 2025). This justifies the need to use satellite data as an additional benchmark.

The data were downloaded as daily values and then averaged to obtain monthly means. The original regular lat-lon grid with a resolution of 0.25 degrees was regridded to a 1° spatial resolution using bilinear interpolation.

4.1.3. CMIP6 models

The Coupled Model Intercomparison Project (CMIP) is an international scientific collaboration created by the United Nations World Climate Research Programme. It was established to facilitate the realization of experiments on past and future climate among different modelling teams. This ensures that differences in simulated climate are ascribed to model differences rather than variations in the experimental setup. CMIP provides a framework for performing experiments, allowing different climate modelling centres to produce standardized outputs, and it offers scientists a comprehensive database of model simulations. The sixth phase of the Coupled Model Intercomparison Project includes 53 climate modelling centres that run over 100 climate models (Miller et al., 2021; European Centre for Medium-Range Weather Forecasts (ECMWF), 2023). CMIP includes different scenarios for climate model experiments. In this analysis, the historical scenario (between 1850 and 2014) was used, and the output of this experiment was compared to both PlaSim and observations.

The four CMIP6 models considered in this analysis are listed in *Table 7*. Two of them, the AWI-ESM1-1-LR and MPI-ESM1-2-LR, use the same land model to simulate vegetation, while the other two employ different ones.

Table 7: Description of the four CMIP6 models used in the comparison and general characteristics of their implemented vegetation models.

Model	Institute	Land Surface Model	Plant functional types	Number of phenological types
AWI-ESM1-1-LR	AWI (Germany)	JSBACH 3.2	12	5
EC-Earth3-Veg	EC-Earth-Consortium (Europe)	LPJ-GUESS	10	3
MPI-ESM1-2-LR	MPI (Germany)	JSBACH 3.2	12	5
UKESM1-0-LL	MOHC (UK)	JULES-ES-1.0	9	2

All the chosen models simulate the plant type distribution dynamically, rather than using prescribed distributions based on land use and land cover change, which is the case in many other CMIP6 models (Song et al., 2021). Unlike PlaSim, these four models include Plant Functional Types (PFTs) to describe vegetation, which allow to represent the wide variety of plant species present in the world in a simplified way. Plant functional types account for different responses based on vegetation type. Each PFT is characterized by distinct properties, which vary depending on the model, such as photosynthetic pathway type (C3 or C4), parameters of the photosynthesis models, type of phenology (e.g. grass, raingreen). For example, they can account for different responses in albedo and surface conductance based on morphological differences in leaf types (Duveiller et al., 2023; Reick et al., 2021).

Both the AWI-ESM1-1-LR and MPI-ESM1-2-LR models use the same land surface model, called JSBATCH. The model represents the vegetation using 12 Plant Functional Types, whose spatial distribution is dynamic, and changes with the climate (Shi et al., 2020). The phenology model present in JSBATCH is directly linked to the climate, requiring climatic variables as input, specifically temperature, soil moisture, and Net Primary Productivity (NPP). It distinguishes between five phenological types: evergreen, summergreen, raingreen, grasses and crops. Evergreen and summergreen phenologies depend on temperature, which changes with season, while raingreen phenology depends on soil moisture, with higher soil moisture levels linked to lower shredding rates. Grass phenology depends on temperature, soil moisture and NPP, as grasses grow in all types of climates only when certain conditions (fPAR, CO2 concentration etc.) are within a suitable range, these conditions are reflected by NPP. Finally, crop phenology depends on temperature, soil moisture and NPP as well. Each PFT is linked to one of these phenological types (Reick et al., 2021).

EC-Earth3-Veg uses the LPJ-GUESS model for dynamic vegetation, which simulates the size, age, structure, temporal dynamic and spatial heterogeneity of vegetation (Döscher et al., 2021). It comprises 10 Plant Functional Types, which categorize vegetation based on climatic conditions, growth form (tree or herb), photosynthetic pathway and leaf phenology type (Smith, 2007). The model defines three types of phenologies, which are similar to the previous vegetation model. These phenologies are:

- Drought deciduous (raingreeen), common in drier parts of the tropics, where plants shed their leaves during dry season. This phenology depends on soil moisture and transpirative demand.
- Winter deciduous (summergreen), for plants that shed the leaves in winter; these plants are characteristic of cool temperate and boreal biomes. Winter deciduous phenology depends on temperature.
- Evergreen, the plants with this phenology do not shed their leaves, and this phenology does not depend on climate variables.

Lastly, UKESM1-0-LL uses 9 Plant functional Types, which are competing for space and change dynamically (Sellar et al., 2019; Clark et al., 2011). These PFTs include two phenological types:

- Cold deciduous, which depends on temperature. The leaves start dying when temperature drops below a threshold, which varies for different PFTs.
- Drought deciduous, which is simulated as the cold-deciduous, but it depends on soil moisture instead of temperature.

As already mentioned, the LAI for the four models was obtained from historical simulations, which span from 1850 to 2014. The historical simulations cover years in which observations are available, these observations are used to represent the historical variability of external forcing. The historical forcing data includes GHG concentrations, stratospheric aerosol concentrations, emission of aerosol and GHGs, sea surface temperatures and sea-ice concentrations, solar forcing, time varying gridded ozone concentrations and time varying gridded land-use forcing datasets. Some models may need additional forcing datasets (Eyring et al., 2016). For the comparison presented in this chapter, the years between 1980 and 2014 were considered. The data was downloaded in 1° spatial resolution.

4.1.4. PlaSim

The LAI data were obtained from the simulations explained in Chapter 3.4.1 for both interactive and non-interactive vegetation modes. The data were transformed from a T21 grid into a to 1° spatial resolution, using bilinear interpolation. As opposed to CMIP6 models, SimBA does not use PFTs, and its phenology is exclusively drought deciduous, which results in a considerably simpler model in comparison. Its characteristics are summarized in *Table 8*.

Table 8: Description of PlaSim and summary of SimBA characteristics, as opposed to CMIP6 models reported in Table 7.

Model	Institute	Land Surface Model	Plant functional types	Number of phenological types
PlaSim	University of Hamburg	SimBA	0	1

4.2. Spatial pattern and global average

The global distribution of LAI for all the datasets considered is shown in *Figure 16*. The time intervals considered for the analysis were 1980-2014 for both satellite observations and CMIP6 models. This interval allows to consider long-term vegetation dynamics and their interaction with the climate. These data were then compared to the LAI simulated by PlaSim, which was obtained from a simulation with constant CO_2 concentration of 354 ppm, a value that corresponds to the observed concentration within the time interval considered. Additionally, only the last 50 years of PlaSim data were considered, after equilibrium was reached.

All models are generally able to replicate the global distribution of LAI. They successfully represent high values in tropical forests in Central Africa, in the Amazon and in Southeast Asia. Moderate values of LAI can be observed in boreal and temperate forests in Europe, Asia and North America as well as in the tropical savannas of Africa and South America. Low LAI values are found over deserts, in shrublands and sparsely vegetated regions, such as North Africa, Middle East and Australia.

Both AWI-ESM1-1-LR and MPI-ESM1-2-LR models accurately capture the spatial distribution of LAI across the world, without significantly overestimating LAI in specific regions. In contrast, PlaSim, EC-Earth3-Veg and UKESM1-0-LL tend to overestimate vegetation in the tropical regions of Central Africa, the Amazon and Southeast Asia compared to the benchmarks, as well as in boreal and temperate forests. Notably, the vegetation model used in AWI-ESM1-1-LR and MPI-ESM1-2-LR features the highest number of PFTs and types of phenology out of all the models, as shown in *Table 7*.

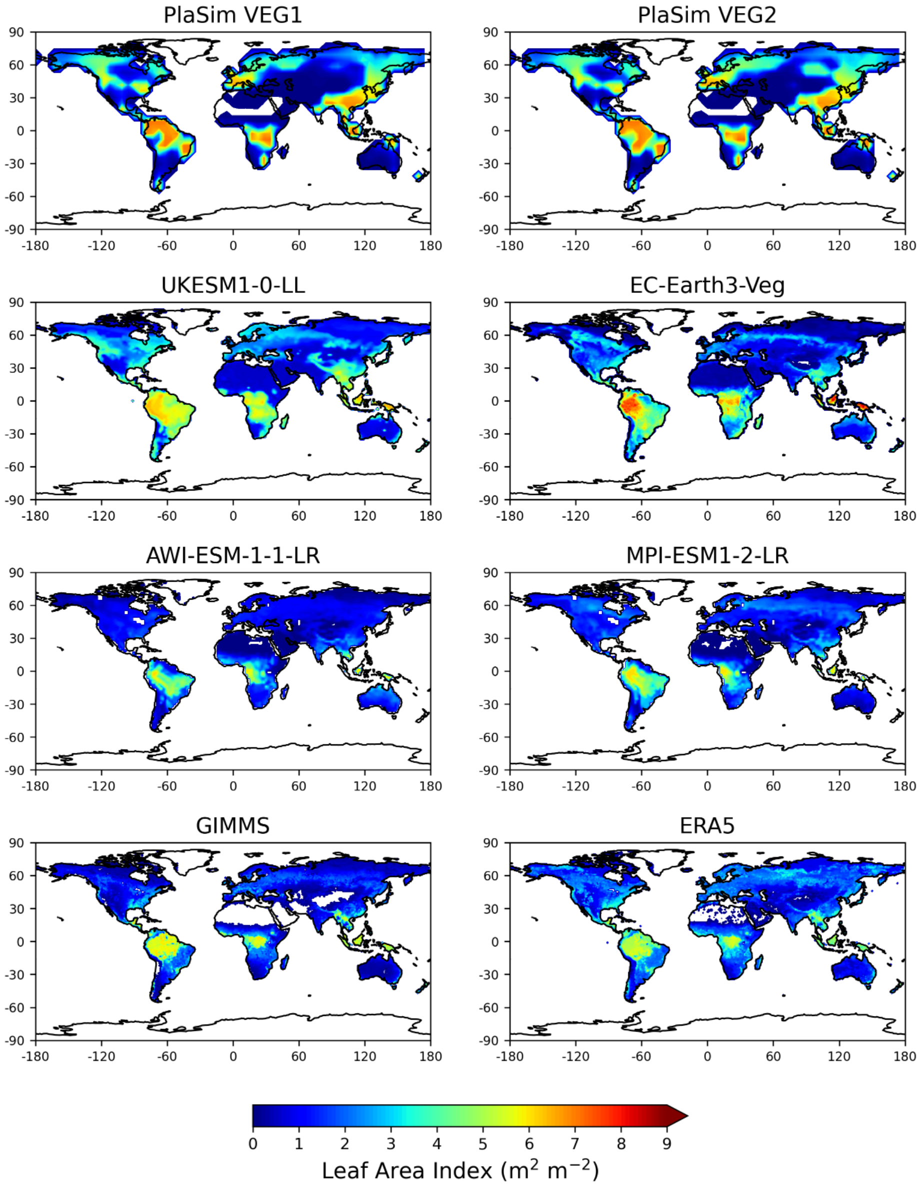

Figure 16: Global distribution of multi-year averaged LAI. The first row represents PlaSim results in the non-interactive (VEG1) and interactive tuned (VEG2) vegetation modes. The second and third row represent the LAI simulated in four CMIP6 models (see Table 7), while the last row shows spatial distribution of LAI from satellite (GIMMS) and ERA5 reanalysis.

The maps in *Figure 17* show the bias in simulated LAI from the models compared to the satellite-derived (GIMMS) observations. It is evident that different models exhibit distinct biases in different locations. EC-Earth3-Veg and UKESM1-0-LL show an overall positive bias over most land areas, with stronger overestimations in tropical regions in South America, Africa and Asia and in boreal and temperate regions in North America, Europe and Asia. EC-Earth3-Veg shows an underestimation of LAI in Eastern Amazonia and Russia, while UKESM1-0-LL shows low underestimation. Both AWI-ESM1-1-LR and MPI-ESM1-2-LR models tend to underestimate LAI in equatorial regions, but their overall bias is lower compared to the other models.

In PlaSim, the areas affected by biases exhibit significantly higher values compared to other models, where biases are more uniformly distributed on land. On the other hand, PlaSim accurately represents LAI in some regions characterized by low LAI, such as Australia, North Africa and parts of Asia, where biases are not observed, as opposed to other models. In PlaSim, LAI is overestimated in Europe, Southeast Asia and Canada, while it is underestimated in some regions of Central Africa and South America. Overall, while models can capture broad spatial patterns, discrepancies are present in specific regions. These regional biases are more pronounced in PlaSim compared to other models.

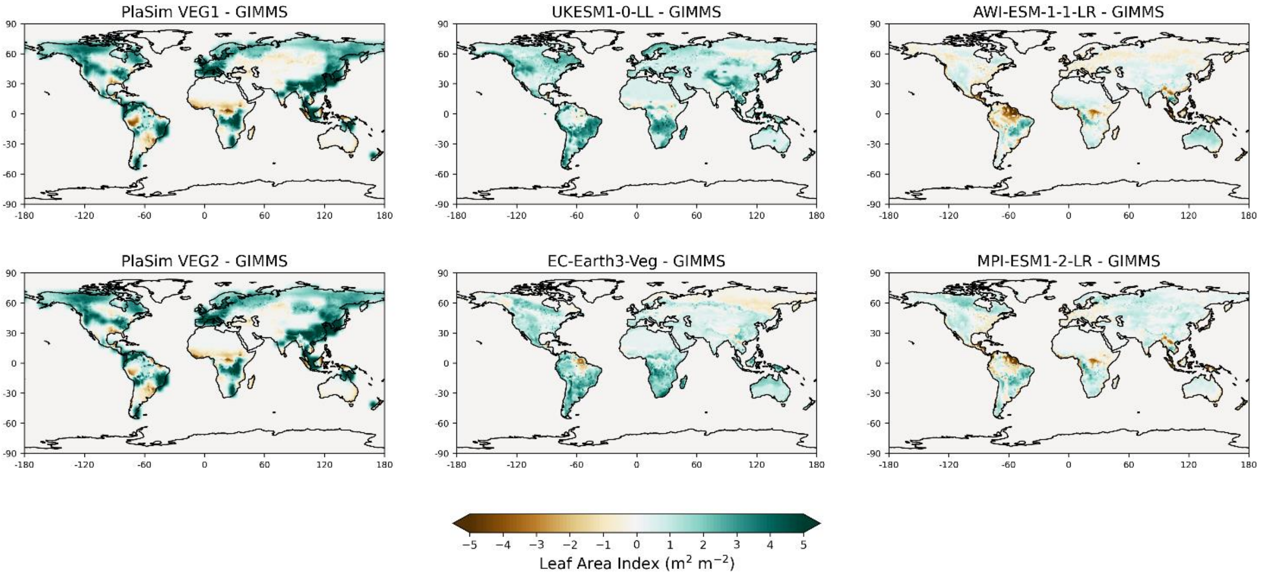

Figure 17: Global distribution of biases in multi-year averaged LAI compared to satellite data (GIMMS). The first column represents PlaSim simulations in the non-interactive (VEG1) and interactive tuned (VEG2) vegetation modes. The second and third column represent LAI simulated in four CMIP6 models (see Table 7).

The globally averaged LAI is shown in *Figure 18*. Compared to observation, PlaSim overestimates the global mean in both interactive and non-interactive modes, which are show similar values. Both AWI-ESM1-1-LR and MPI-ESM1-2-LR underestimate this value, while the remaining models overestimate it. EC-Earth3-Veg shows the closer values to benchmarks. Notably, the values estimated by PlaSim fall within the range of globally averaged LAI from the CMIP6 models, which are 1.18 m^2m^{-2} and 2.46 m^2m^{-2}, respectively.

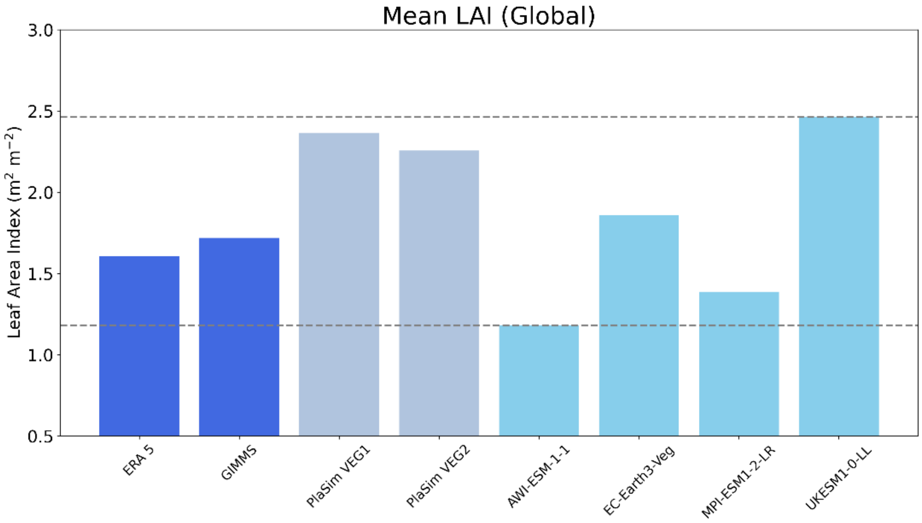

Figure 18: Globally averaged LAI of multi-year mean for the observations (in dark blue), PlaSim (in grey), and the four CMIP6 models (in light blue). The dotted lines represent the range of global average LAI across the CMIP6 models, from minimum to maximum.

4.3. Seasonality

4.3.1. Areas considered for the analysis

The seasonality in LAI was evaluated over different regions of the world: Europe, Amazonia, and at the hemispheric level. The first two regions considered are represented within the red boxes in *Figure 19*. Specifically, the European region is represented by an area located in Germany, while the Amazonian region is divided into two areas: Eastern and Western Amazonia. The former is located between Peru, Colombia and Brazil, while the latter is located in Brazil. This selection allows to focus on seasonal variability in two different climate zones: tropical regions near the equator and temperate areas in mid-latitudes. These are typically associated with different phenological patterns, with drought-deciduous vegetation common in tropical regions and winter-deciduous vegetation predominantly present in temperate and boreal areas. The boxes were chosen in areas exhibiting homogeneous LAI.

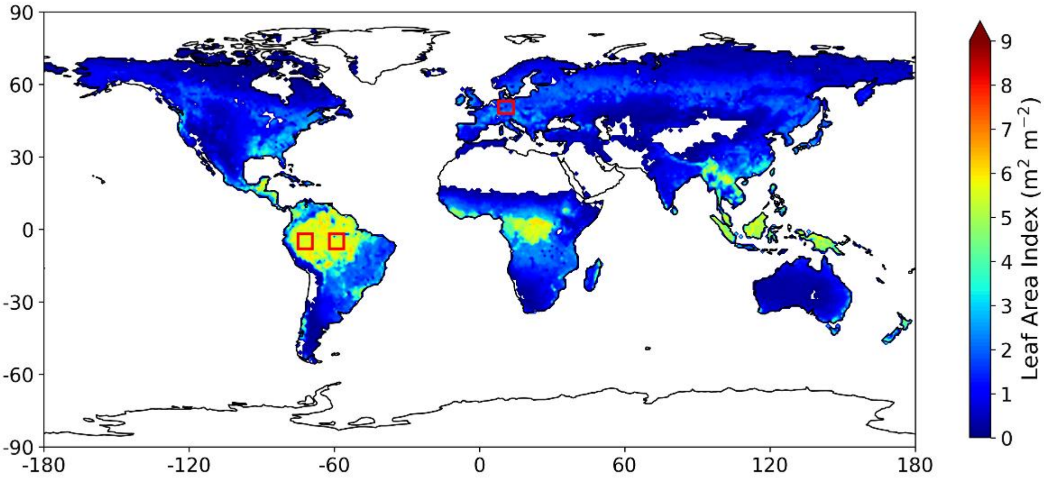

Figure 19: Map of multi-year averaged LAI from satellite observations (GIMMS). The three red squares represent the areas considered to evaluate the seasonal cycle of LAI.

4.3.2. Results

The seasonal cycle of LAI normalized by mean is shown in *Figure 20* for the three different areas. In Europe, the seasonality of CMIP6 models follows the seasonality of the benchmark datasets. Both CMIP6 and observations exhibit high values of LAI in June-September and lower values in December-February. However, CMIP6 models show a 1-2 month delay in the LAI peak compared to observations, which could cause biases in energy and water cycle (Song et al., 2021). On the other hand, PlaSim shows opposite seasonality to both benchmark and CMIP6 models, with high values of LAI in December-February and lower values in June-September. The seasonal cycle without normalization is shown in *Figure 21,* clearly indicating that PlaSim overestimates LAI in every month compared to both observations and CMIP6 models. Moreover, the amplitude in LAI seasonal variance is lower in PlaSim compared to benchmarks and observations, as values only slightly vary throughout the year. CMIP6 models show similar amplitude compared to satellite observations.

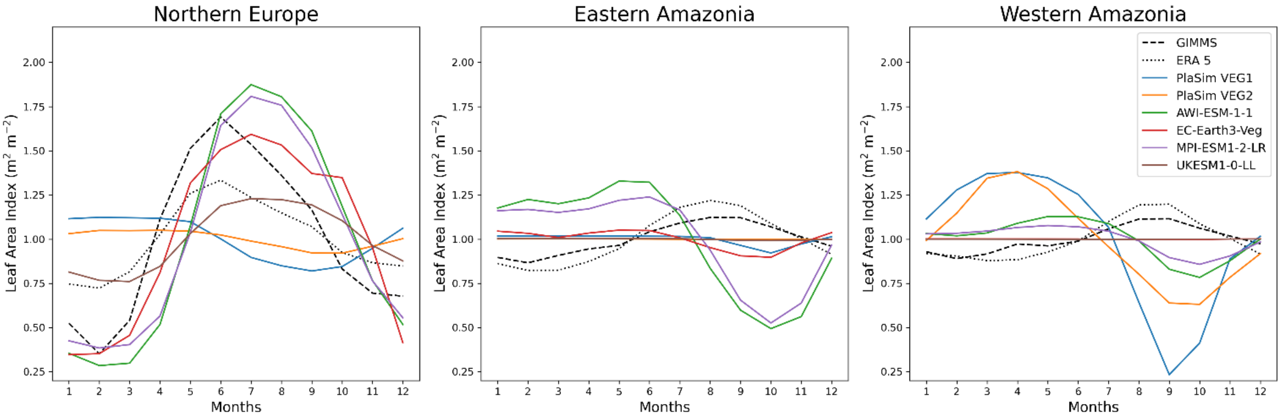

Figure 20: Seasonal cycle of LAI normalized by mean averaged over the years. The plots show values for CMIP6 models, PlaSim, satellite (GIMMS) and ERA5 reanalysis in the three different regions. The benchmarks are represented by dotted lines.

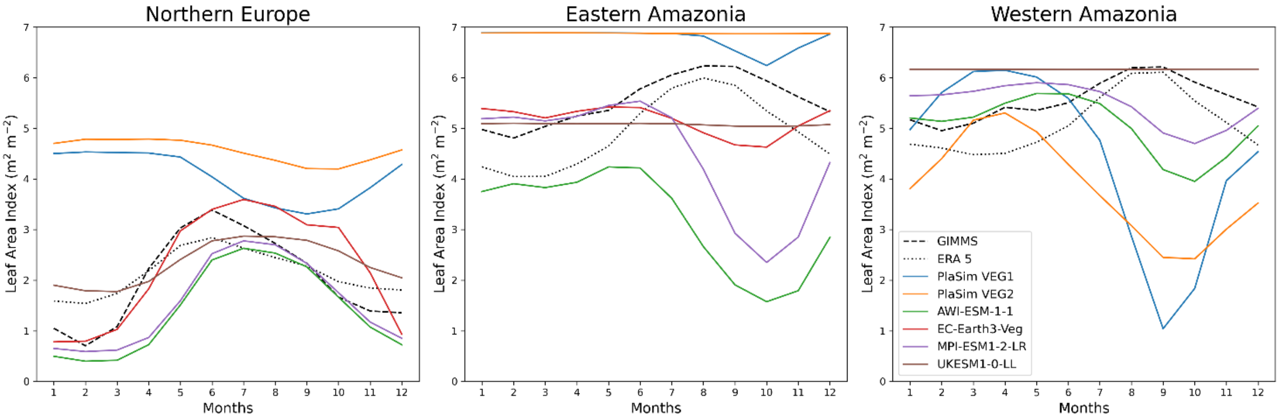

Figure 21: Seasonal cycle of LAI averaged over the years. The plots show values for CMIP6 models, PlaSim, satellite (GIMMS) and ERA5 reanalysis in the three different regions. The benchmarks are represented by dotted lines.

Observations indicate similar seasonality patterns in Eastern and Western Amazonia, with peaks during July-September. Both regions are characterized by lower amplitude and higher average values compared to Europe. However, models show significant variations between the Eastern and Western regions. Moreover, in all regions, the interactive mode of PlaSim shows higher amplitude of seasonality compared to the non-interactive mode.

In Eastern Amazonia, both PlaSim and CMIP6 models fail to capture the seasonality, which is weaker than in Europe, as shown in *Figure 20*. Both AWI-ESM1-1-LR and MPI-ESM1-2-LR exhibit seasonal cycle that is opposite to that of the benchmark datasets, and they overestimate the amplitude of seasonality, while the other models exhibit a nearly constant LAI throughout the seasons. When models exhibit a negative peak, the peak happens in October, while benchmark data show maximum values in August-September and lower values in December-February. The plot in *Figure 21* for

Eastern Amazonia reveals that different models produce varying mean LAI; both interactive and non-interactive PlaSim modes overestimate the mean LAI compared to benchmark datasets.

In Western Amazonia PlaSim, AWI-ESM1-1-LR and MPI-ESM1-2-LR show opposite seasonality patterns compared to benchmark datasets, with lowest values in August-October, whereas observations show a peak during this period. UKESM1-0-LL and EC-Earth3-Veg do not exhibit seasonal variations. Moreover, PlaSim overestimates the amplitude of seasonality compared to observations, while CMIP6 models exhibit similar values to the benchmark. As shown in *Figure 21*, PlaSim shows different seasonal patterns compared to the rest of the models, with a general underestimation of mean LAI.

Overall, PlaSim does not represent the seasonal cycle well in the three regions analysed. In comparison, CMIP6 models are good at capturing the seasonal cycle in Europe, although they delay the time of maximum LAI by 1-2 months. The inability of PlaSim to represent seasonal variations in Europe is likely due to the lack of winter-deciduous phenology in SimBA, which can only model drought-deciduous phenology. This absence prevents PlaSim from capturing seasonal vegetation dynamics accurately in temperate and boreal regions.

Both CMIP6 models and PlaSim significantly struggle in depicting the seasonal cycle in the Amazon. This could be due to the dependency of phenology on solar radiation in this region, which is not represented in most models, as many of them primarily rely on soil moisture and temperature to represent phenology. The main abiotic factors driving plant phenology in tropical regions are irradiance and water stress. Cloudiness near the equator can greatly reduce available light, while peak in radiation is registered during the dry season, when cloud cover is lower. Furthermore, evidence suggests that both understory plants and canopy trees in tropical regions may be light-limited (Schaik et al., 2003). Therefore, a drought-deciduous phenology may not be sufficient to replicate observed phenological patterns.

While CMIP6 models can capture the seasonal dynamics in certain regions, their ability to reproduce seasonality in tropical climates remains limited, highlighting the need of improved phenology.

The seasonal cycle of temperature, evaporation and precipitation in PlaSim was analysed in Europe and Amazonia and compared to ERA5 observations between 2005 and 2015. The result is shown in *Figure 22*.

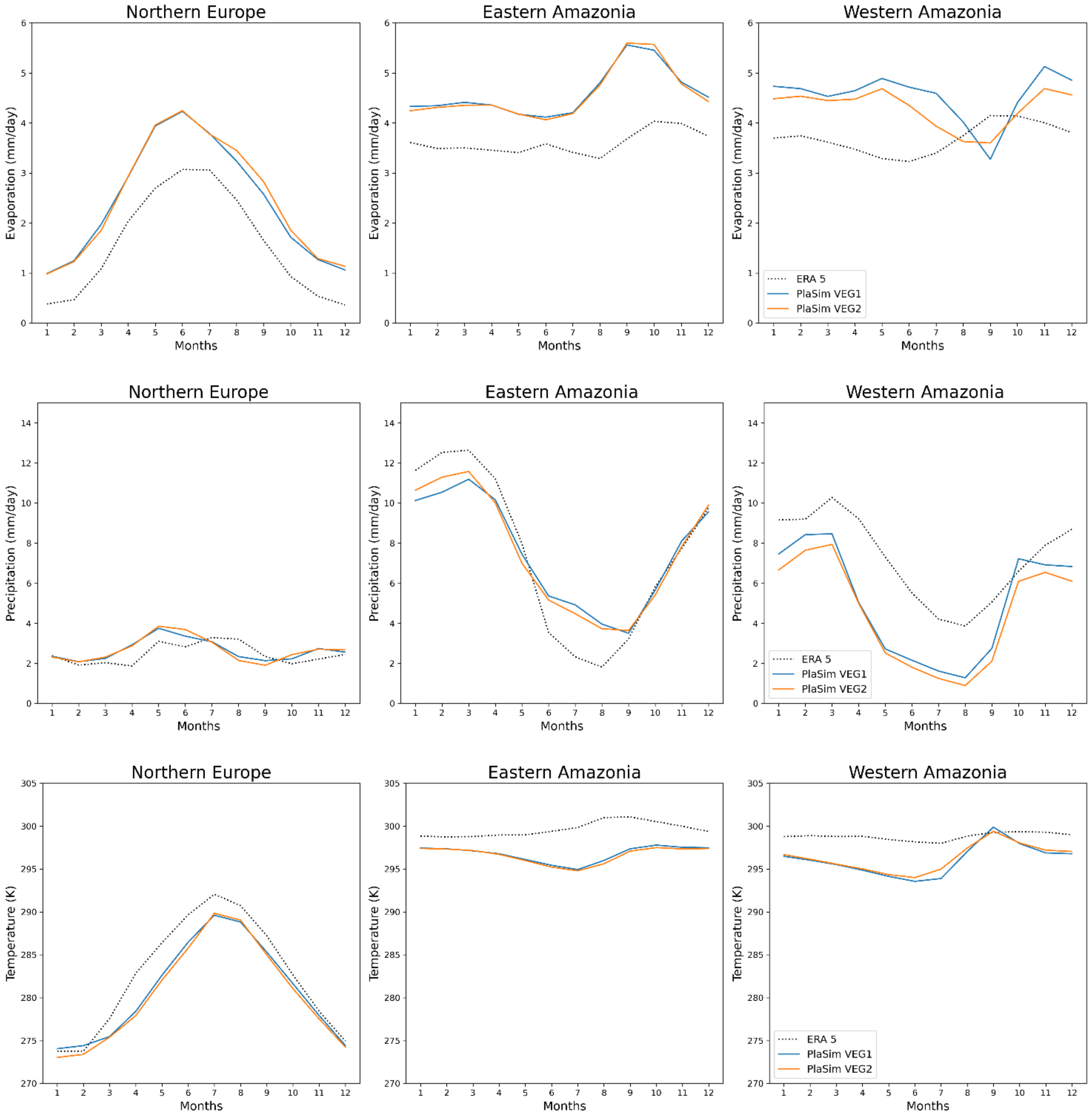

Figure 22: Seasonal cycle for temperature, evaporation and precipitation in Northern Europe, Eastern Amazonia and Western Amazonia. The plots show values PlaSim, in both interactive (VEG2) and non-interactive (VEG1) vegetation mode and ERA5 reanalysis. The ERA5 data was averaged between the years 2005 and 2015.

Temperature and evaporation in Northern Europe exhibit similar seasonal variability to observations, while precipitation shows slightly different patterns, with an underestimation of precipitation during July-September. In all areas, the model overestimates evaporation on land, while temperature is slightly underestimated. In Amazonia, PlaSim cannot exactly reproduce the seasonal patterns, particularly in Western Amazonia, although average yearly values remain comparable. This highlights that the issue in reproducing seasonal variations in LAI is likely due to how vegetation is modelled in PlaSim and to an incomplete phenology in the model, which does not consider temperatures.

The seasonal cycle was also analysed in the Northern and Southern Hemispheres at large. *Figure 23* and *Figure 24* show the seasonal cycles of LAI for both hemispheres.

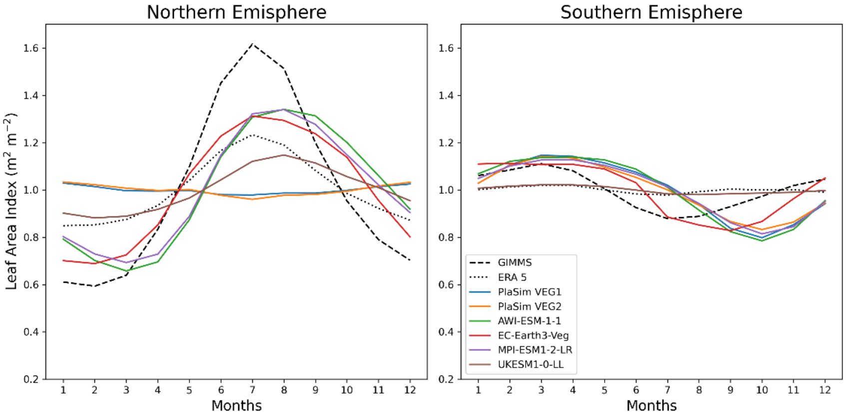

Figure 23: Seasonal cycle of LAI normalized by mean averaged over the years. The plots show values for CMIP6 models, PlaSim, satellite (GIMMS) and ERA5 reanalysis in two hemispheres. The benchmarks are represented by dotted lines.

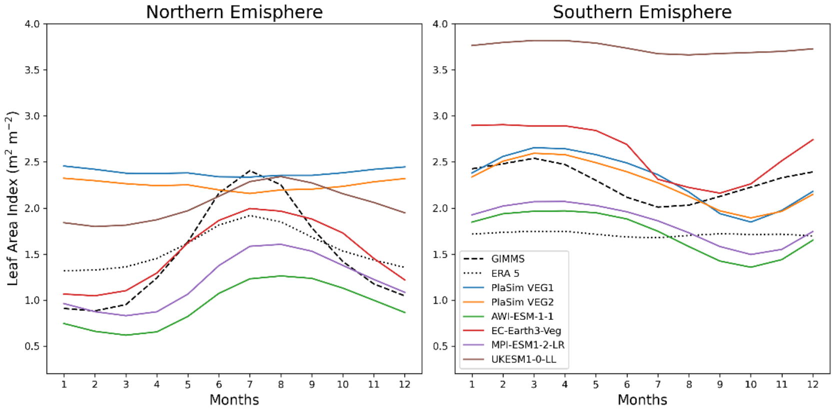

Figure 24: Seasonal cycle of LAI averaged over the years. The plots show values for CMIP6 models, PlaSim, satellite (GIMMS) and ERA5 reanalysis in the three different regions. The benchmarks are represented by dotted lines.

The comments previously made for seasonality in Europe also apply to the Northern Hemisphere. This could be explained by the large spatial extent of boreal and temperate zones in the Northern Hemisphere. In this region, CMIP6 models depict seasonality reasonably well, with a shift in the peak LAI of 1-2 months, while PlaSim does not accurately represent the seasonality, and overestimates the mean value of LAI (see *Figure 24*).

In the Southern Hemisphere, the behaviour differs from that observed in Eastern and Western Amazonia, as the minimum in LAI from satellite observations occurs during June-September. Moreover, the average value for observations, shown in *Figure 24* is significantly lower than the one observed in Amazonia. This difference can be explained by the fact that only a fraction of the Southern Hemisphere is covered by tropical forest, while a substantial portion is composed of shrublands, deserts and semi-arid lands (Olson et al., 2001). All the models, except UKESM1-0-LL, have similar amplitude, which is comparable to ERA5, but the peaks are shifted by 2-3 months. PlaSim can represent the average value of LAI in this hemisphere surprisingly well, even compared to the other CMIP6 models, as shown in *Figure 24*. While PlaSim fails to capture the seasonal cycle in the Northern Hemisphere, its behaviour in the Southern Hemisphere is fairly similar to observations, although it exhibits 2-3 months shift in the timing of the peak value, a pattern also observed in other CMIP6 models.

To conclude, PlaSim cannot accurately represent the seasonality in Europe and in the Northern Hemisphere at large, compared to CMIP6 models. The behaviour is likely due to the absence of a winter-deciduous phenology in PlaSim, which is included in the other four CMIP6 models. In the Amazon rainforest, PlaSim also fails to accurately represent seasonality. However, CMIP6 models struggle with seasonality in this region as well. This highlights the complexity of representing the phenology in the Amazon, which remains challenging even for more complex models. In the Southern Hemisphere, PlaSim behaviour is more similar to that of other models and observations, but it still does not fully capture seasonality due to a time shift in the peak LAI value.

4.4. Interannual variability

The coefficient of variation (CV) for detrended data was calculated for the three areas considered in *Chapter 4.3*. This metric is used to assess the spatial variance and the interannual variability of LAI, and it is calculated as the ratio of standard deviation over mean LAI for each year, then averaged over time. The formula is shown in *Equation 24*.

$$CV = \frac{\sigma}{\mu} \tag{24}$$

This value provides an indication of interannual variability in LAI due to natural oscillations of the system, as it was calculated for detrended data. The results are shown in *Figure 25*.

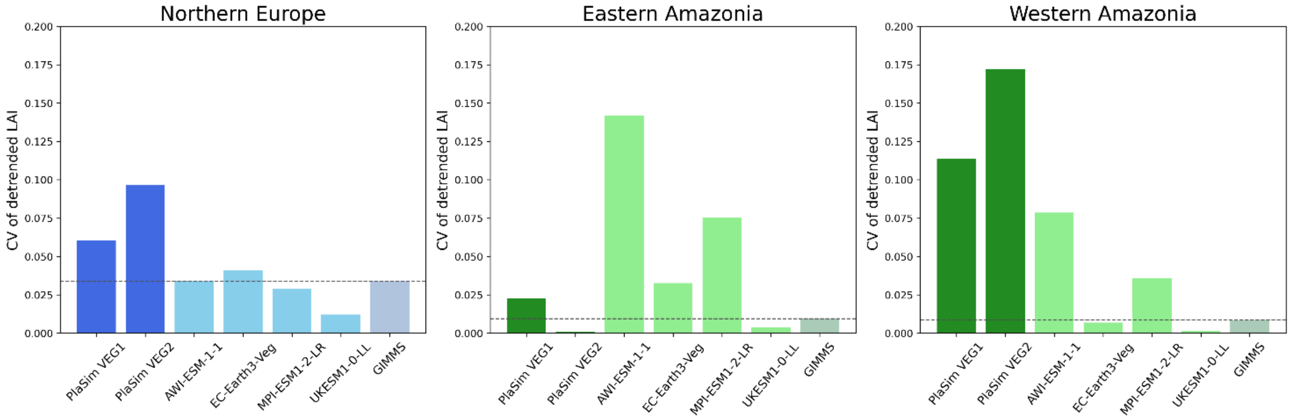

Figure 25: Coefficient of variation calculated over three different areas: Northern Europe, Eastern Amazonia, and Western Amazonia. The plots show values for PlaSim in non-interactive (VEG1) and interactive (VEG2) vegetation mode, the four CMIP6 models and satellite observations (GIMMS).

PlaSim overestimates interannual variability in Europe and Western Amazonia compared to satellite data. In Eastern Amazonia, the interactive vegetation mode reduces interannual variability compared to the non-interactive mode. Conversely, in the other two regions, the opposite is observed, suggesting that the feedback mechanisms in the interactive mode can either dampen or amplify variability depending on the local climatic conditions and vegetation responses.

In both Eastern and Western Amazonia, CMIP6 models struggle to capture the observed interannual variability, except for UKESM1-0-LL, which shows similar values to observations. This suggests the complexity in modelling the interannual variability in this regions, likely due to complex interaction between soil moisture, precipitation and vegetation. In Northern Europe, all CMIP6 models outperform PlaSim in reproducing observed values, which indicates better representation of higher-latitude systems in CMIP6 models.

Overall, a study showed that most CMIP6 models cannot reproduce the interannual variability of LAI at the global scale. Most models cannot capture interannual variability in the Amazon rainforest, where CV is underestimated compared to satellite data (Song et al., 2021). Although PlaSim fails in capturing the interannual variability, CMIP6 models also struggle, particularly in certain regions.

4.5. Concluding remarks

This chapter aimed at evaluating how LAI is simulated in PlaSim compared to observations, and to contextualize its performance in the framework of more complex Earth System Models in the CMIP6 project. The main conclusions are summarized in the following points:

- PlaSim successfully reproduces the global spatial pattern of annual mean LAI, with the spatial distribution of high medium and low LAI generally comparable to observations.
- The average global LAI in PlaSim is higher than observations, but it falls within the range of values in CMIP6 models.
- PlaSim does not accurately reproduce seasonality in Europe, Amazonia or the Northern Hemisphere at large. CMIP6 models can reproduce seasonality in Europe and in the Northern Hemisphere, although they delay the time of maximum LAI by approximately 1-2 months. However, they struggle to represent seasonal patterns in Amazonia. This highlights the need for all models to improve the parametrization of phenology, potentially including its dependency on light.
- PlaSim fails in capturing interannual variability of LAI, although CMIP6 models also struggle, particularly in certain regions.

Overall, the issue of reproducing seasonality in PlaSim is likely due to the absence of winter-deciduous phenology, as the model can exclusively represent drought-deciduous phenology, which depends on soil moisture. To improve PlaSim performance and its ability to reproduce seasonality at mid-latitudes, phenology should be incorporated as a function of both soil moisture and temperature. However, the model must remain simple enough to align with medium complexity-models.

The results presented in this chapter show that PlaSim can be used to investigate variability in vegetation properties, and how they interact with the climate system over long time scales (decades and beyond), where seasonal changes play a minor role.

5. Climate tipping of vegetation at the regional scale

This chapter explores the effects of increasing atmospheric CO_2 concentration on vegetation, using a PlaSim simulation run with the tuned interactive vegetation mode. The goal is to understand how vegetation responds to rising CO_2 concentrations, and how, in turn, vegetation might influence regional climate. Specifically, this chapter explores the interdependencies between vegetation and the local hydrological cycle, by analysing the time series of LAI, evaporation, precipitation, soil moisture and other variables. The focus will be on two locations: Europe and the Amazon rainforest. The analysis aims to detect abrupt changes in LAI within these regions and assess their relationship with the hydrological cycle.

5.1. Experimental setup

The simulation was performed using PlaSim with the tuned interactive vegetation mode for a 3000-year run. The simulation was performed with all modules enabled, including the Large-Scale Geostrophic Ocean model (LSG). The atmospheric CO_2 concentration was increased from an initial value of 354 ppm, starting from the final conditions of the previous simulations, which ensured that the climate had already reached stability at the beginning of the simulation. The atmospheric CO_2 concentration was increased by 0.2 ppm each year, a rate lower than the current rate (an increase of 2.8 ppm was observed between 2022 and 2023) (Lan & Keeling). By the end of the simulation, the CO_2 concentration reached 954 ppm.

The gradual increase in atmospheric carbon dioxide concentration helped maintain near-equilibrium conditions for vegetation. An abrupt change in forcing, caused by a steep increase in CO_2 concentration, would cause a transient state, requiring time for the system to adjust to a new equilibrium, as explained in *Chapter 3*. Different components of the climate system respond in different time scales. Vegetation has a response time of 10 years in PlaSim, as defined in *Equation 1.* Ideally, after each increase in CO_2, the new equilibrium would have to be reached before further increasing the CO_2. However, given the impracticability of this approach, the slow increase in atmospheric CO_2 allows the vegetation to continuously adapt, reaching a new equilibrium state within the year, preventing it from lagging behind the forcing.

The model outputs were provided as monthly averaged values, produced on a T21 horizontal grid. The variables considered for the analysis were two-meter air temperature (var 167), convective precipitation (var 143), large scale precipitation (var 142), evaporation (var 182), leaf area index (var 200), soil water holding capacity (var 229), soil moisture (var 140) and runoff (var 160).

5.2. Regions considered

This subsection will provide a brief analysis on the two regions considered for the analysis of vegetation tipping, focusing on their key characteristics and significance within the climate system.

5.2.1. Amazon

The Amazon rainforest is the largest tropical forest on Earth, covering an area of 7 million km^2 across nine countries: Colombia, Peru, Brazil, Venezuela, Ecuador, Bolivia, Guyana, Surinam, and French Guaina. The majority of the forest, around 60%, expands over Brazil. (Siqueira Silva et al., 2010). It is a key component of the Earth system, given its importance as a biodiversity hotspot and as a carbon sink, storing approximately 120 Pg ($1.2 * 10^{17} g$) of carbon within its biomass. For this reason, even relatively limited changes in the forest dynamics can affect the atmospheric CO_2 concentration and influence climate change (Phillips et al., 2009).

Tropical forests play a crucial role in regulating the globate climate, and their disappearance could trigger widespread consequences across the Earth system (Staal et al., 2020). The Amazon rainforest has a significant impact in both South America and global climate by regulating hydrological feedback processes. Moisture is transported in Amazonia from the Atlantic Ocean through trade winds. At the regional scale (between 100 and 1000 km), tropical forests enhance rainfall, as trees absorb moisture from the ground, and they release it in the atmosphere during photosynthesis. This process allows trees to photosynthesise even during droughts, up to a certain limit, while simultaneously mitigating the drought conditions themselves (Staal et al., 2020).

In the Amazon rainforest, between 30-50% of the rainfall in the area is returned to the atmosphere through plant evapotranspiration (Marengo et al., 2009). In some parts of the basin, especially during dry season, up to 70% of precipitation is recycled through vegetation-driven transpiration fluxes (Armstrong McKay et al., 2022). Additionally, moisture originated from the basin is transported to other regions within the continent, influencing rainfall in distant regions from the rainforest itself (Marengo et al., 2011).

The recycling of atmospheric moisture in the Amazon is driven by various feedback mechanisms, acting at different scales, that both influence and depend on the presence of the tropical forest. At the local level, these feedback processes lead to two possible stable states for vegetation: either a forested landscape or a savanna. In this bistable system, the current distribution of tropical forest is not solely a consequence of the present climate, but it is also determined by the past forest extent. This reflects the hysteresis of tropical forests (Staal et al., 2020).

The amazon rainforest is one of the possible tipping elements of the climate system, as it is at risk of crossing a tipping point, defined by the IPCC as "a critical threshold beyond which a system reorganizes, often abruptly and/or irreversibly". Due to rising global temperatures, the rainforest could pass the tipping point, leading to vegetation loss (Chen et al., 2021). Moreover, this forest dieback could act as a positive feedback, as it would release carbon dioxide into the atmosphere, leading to further increase in temperature (Parry et al., 2022).

Several factors can contribute to the Amazon dieback, the main ones being a prolonged dry season, increased fire frequency and reduced rainfall. With global warming, the number of extreme hot and dry days is expected to increase, along with an intensification of both severity and duration of the dry season. This is expected to produce an increase in tree mortality. Moreover, as the rainforest becomes dryer, its vulnerability to fire will increase. Human-driven deforestation exacerbates these changes by reducing evapotranspiration, which is critical for maintaining moisture levels in the region, thereby reducing rainfall during dry season and weakening the forest resilience to climate change. The loss of resilience is more pronounced in regions with lower precipitation and higher deforestation due to human activity (OECD, 2022; Parry et al., 2022). To summarize, the main cause of vegetation dieback are the mechanisms which produce the drying of the Amazon rainforest (Parry et al., 2022). The shift into a savanna-like state could be irreversible even when the climate forcing is reversed (Nian et al., 2023).

The southeastern region of the Amazon is expected to be particularly vulnerable to a transition toward a non-forest-covered state. This is because the southern and eastern regions are expected to face precipitation decrease and more frequent extreme drought events as a consequence of climate change. Additionally, these regions are strongly affected by other important drivers such as deforestation (and extensive agriculture), road infrastructure projects and the lack of environmental policies, which contribute to reduced forest resilience (Wunderling et al., 2022).

The consequences of the shift into a savanna state in the Amazon would be widespread and severe, impacting biodiversity, which is mostly endemic to the region, causing the loss of ecosystem functions. Moreover, it would negatively impact local communities, specifically indigenous populations, by reducing food availability and increasing exposure to air pollution and diseases. Finally, as previously mentioned, forest dieback would release carbon into the atmosphere, further exacerbating global warming (OECD, 2022).

As demonstrated in *Chapter 4*, PlaSim can capture the annul vegetation dynamics surprisingly well, when compared to CMIP6 models and observation. Moreover, the LAI in SimBA has a direct dependency on water availability, which is one of the main factors driving tropical forest dieback. For these reasons, PlaSim was used to study vegetation tipping in this area through the 3000-year simulation explained in *Chapter 5.1*.

5.2.2. Europe

While the Amazon rainforest is considered a tipping element of the climate system, vegetation in Europe is not. However, the simulation performed with increasing CO_2 shows that Europe experiences an important decrease in leaf area index, similar to what is observed in South America. Therefore, in addition to this tropical region, a mid-latitude area in Europe, characterized by different climatic and hydrological conditions, was analysed to explore the dynamics behind abrupt changes in vegetation.

Increased atmospheric CO_2 leads to increasing plant productivity and water-use efficiency, up to a saturation point. This fertilization effect promotes plant growth by increasing the gross primary productivity (GPP) and tree cover in regions with favourable climatic conditions (e.g. high latitudes and Central Asia). Nevertheless, in areas where water stress occurs due to higher temperature and reduced precipitation, the benefits of CO_2 fertilization are diminished, as water becomes a limiting factor for plant growth (Port et al., 2012).

The response of vegetation is not expected to be uniform in Europe. Higher temperatures in Northern Europe are expected to produce longer growing seasons, as plant growth in this region is primarily limited by temperature (Port et al., 2012). In contrast, rising temperature and increased drought events in Southern Europe could lead to increased tree mortality and to lower nutrient availability and uptake (Penuelas et al., 2020). In these areas, low soil water availability produced by droughts could outweigh the fertilization effect. Moreover, the increase in frequency and intensity of heatwaves has been exacerbating fire risk in southern and central Europe, contributing to further vegetation loss (Bednar-Friedl et al., 2022). Although vegetation in Europe is not classified as a tipping element of the climate system, abrupt changes in vegetation could lead to important consequences in the region.

5.3. Results

5.3.1. Average global values

Both the mean global temperature and the mean global LAI are shown in *Figure 26*. The graph shows an increase of approximately 0.25 $m^2\,m^{-2}$ in the mean global LAI over the simulated years, which is consistent with the increase in CO_2 fertilization at the global level. Nonetheless, regional variations include both positive and negative changes. An increase in the global average forest cover is also observed throughout the years.

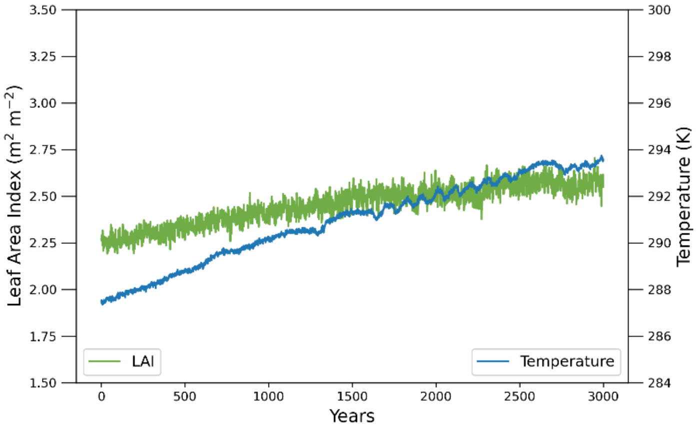

Figure 26: Time series of yearly mean global LAI and yearly mean global temperature.

The temperature shows an increases from 287.5 K to 293.6 K, with a rise of 6.1 K. The mean global temperature shows oscillations after the first 1500 years of oscillations. These coincide with oscillations in the Atlantic Meridional Overturning Circulation (AMOC), which is plotted in red in *Figure 27*.

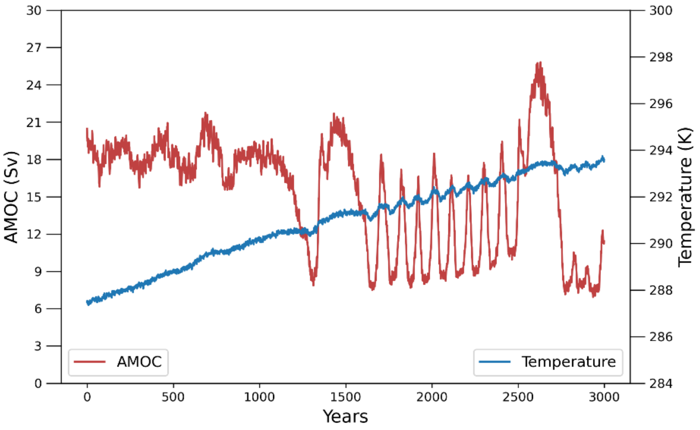

Figure 27: Time series of yearly mean global temperature, measured in K, and AMOC, measured in Sv.

After the first collapse, which occurs around year 1300, the AMOC seems to restart. This is followed by a sequence of oscillations between weak and strong state over the next 1000 years, with a periodicity of approximately a century.

The AMOC is a large-scale circulation pattern in the ocean that transports heath toward the northern regions of the Atlantic Ocean (OECD, 2022). It is a bistable system, meaning that, in addition to the current strong state, a second, weaker circulation mode likely exists. A shift toward this weaker state would influence global temperatures and precipitation patterns (Nian et al., 2023). In the simulation, the AMOC does not stay in a single equilibrium state, but instead it undergoes a series of transitions with a characteristic periodicity. This behaviour suggests that throughout the simulation the system undergoes a series of tipping points, which involve interactions between different climate subsystems. The AMOC oscillations have been observed in models other than PlaSim, such as EC-Earth3.3. The cause of these periodic AMOC oscillations has been attributed to different feedbacks, such as sea ice melt and increased precipitation over the Artic during strong AMOC states. These produce a decrease in Arctic salinity and a positive freshwater anomaly during strong AMOC conditions, eventually triggering a transition to the weaker AMOC state. Conversely, the weak AMOC state leads to an increase in salinity and to negative freshwater anomaly, shifting the system towards a stronger state. The strong AMOC state is associated to warming in the Northern Hemisphere, and changes in precipitation patterns compared to a weaker state (Jiang et al., 2020).

Finally, in *Figure 27*, the AMOC seems to transition into a persistently weak state during the last 300 years of simulation. A weaker AMOC significantly affects the climate system, causing weaker heath transport towards the north, with a cooling effect over the Northern Hemisphere and a warming effect over the Southern Hemisphere. In most scenarios, the cooling effect prevails, leading to a decrease in global mean temperature, with strong regional cooling over Europe and North America (OECD, 2022). Moreover, an AMOC collapse would cause an important disruption of precipitation patterns, specifically in the tropics, with a southward shift of the Intertropical Convergence Zone (ITCZ) (OECD, 2022). As a consequence, significant impacts are to be expected over the Amazon rainforest (Nian et al., 2023).

5.3.2. Maps

Figure 28 shows the difference in LAI and forest cover between the average of the last 50 years of simulation and the last 50 years of the present-day simulation. The leaf area index generally increases at high latitudes in the Northern Hemisphere, across North America, Europe and Asia. This increase can be attributed to rising temperatures, coupled with the CO_2 fertilization effect, which enhances the

Gross Primary Production, as explained in *Chapter 5.2.2*. In specific regions in Canada, which is one of the region with higher positive anomaly, the LAI increases from an average of 1 m^2 m^{-2} in the present-day simulation to 6 m^2 m^{-2} in the last simulated years. On the other hand, the leaf area index decreases in the tropics, specifically in the Amazon rainforest, central America, Africa, southeast Asia and Australia, as well as in central and southern Europe and parts of North America. In regions with negative LAI anomaly located in South America, the LAI decreases from an average of 7 m^2 m^{-2} in the present-day simulation to 4 m^2 m^{-2} during the last simulated year. In Europe, it declines from an average of 6 m^2 m^{-2} to 2 m^2 m^{-2}. Forest cover shows similar behaviour, decreasing in the same areas where LAI declines and increasing where a positive LAI anomaly is observed.

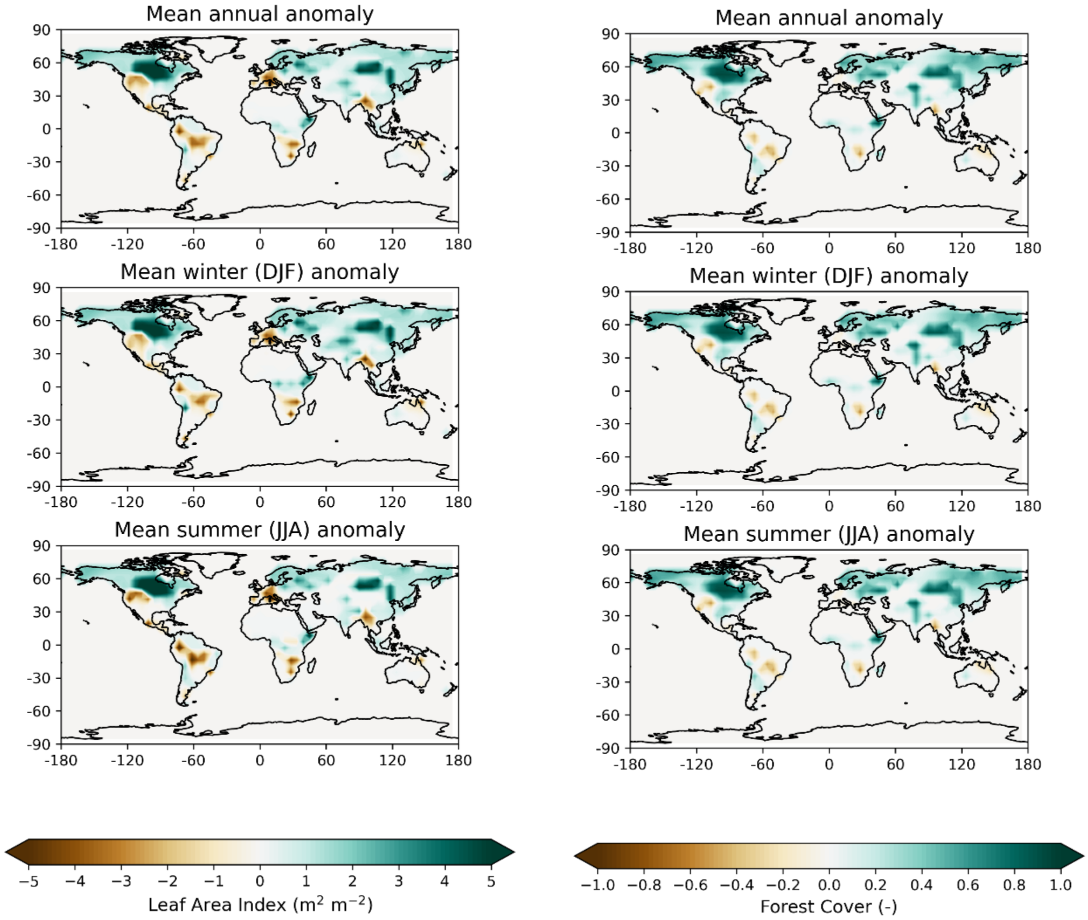

Figure 28: Annual, winter and summer anomaly between the last 50 years of simulation of the 3000-year run and the last 50 years of simulation, after equilibrium was reached, for the 354 ppm run. The figure shows both Leaf Area Index (LAI) and forest cover.

The anomaly in precipitation and evaporation compared to the present-day simulation is shown in Figure 29, while the anomaly in temperature is shown in *Figure 30*.

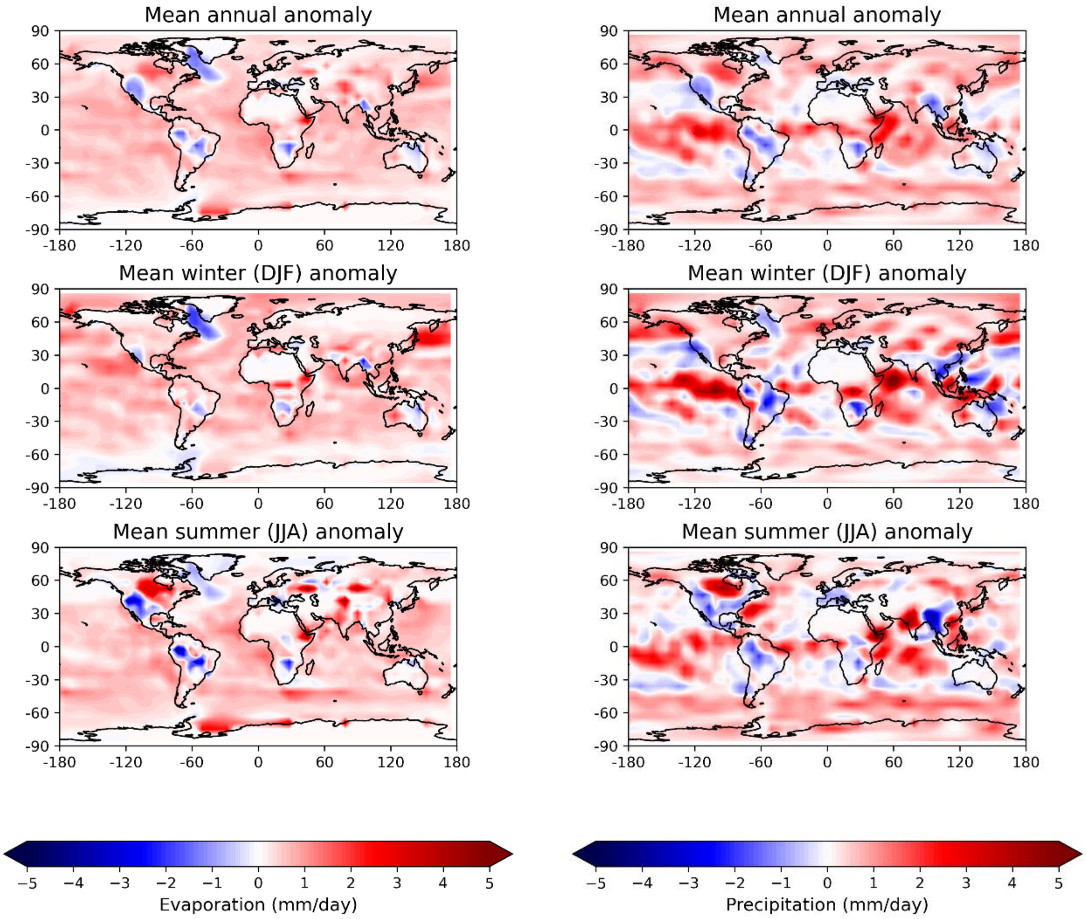

Figure 29: Annual, winter and summer anomaly between the last 50 years of simulation of the 3000-year run and the last 50 years of simulation, after equilibrium was reached, for the 354 ppm run. The figure shows both evaporation and precipitation, measured in mm/day.

Evaporation increases almost everywhere over the ocean and most land areas, except in certain regions. A decrease in evaporation over land is observed over the west coast of North America, over the Labrador Sea, and in tropical regions such as the Amazon rainforest, Africa and parts of southeast Asia and Australia. Apart from the decrease observed over the Labrador Sea, evaporation decreases in regions that also experience a decline in LAI. An exception is Europe, where LAI is decreasing but evaporation shows only a very slight decrease. This behaviour highlights the interdependency between evaporation and vegetation: a decrease in LAI in the Amazon rainforest is linked to a decrease in evapotranspiration, as explained in *Chapter 5.2.1*. Moreover, the observed anomaly in evaporation is higher during June-July-August in America and Africa.

The decrease in evaporation over the Labrador Sea is likely due to the weaker AMOC state, as it only occurs over the last 300 years of simulation and during period of weaker AMOC, when periodic oscillations are observed. Lower temperatures in the area are observed in conjunction to a weaker AMOC, which could explain the decrease in evaporation.

Precipitation anomalies exhibit more complex patterns compared to evaporation. While precipitation increases over most of the surface of Earth, it decreases over mid-latitude oceans and in regions where evaporation and LAI are decreasing as well. A decrease in precipitation is also observed over the Labrador Sea as well, especially during the winter, which coincides with the period of maximum evaporation decline. This behaviour is likely associated to a weaker AMOC state.

In conclusion, regions on land that show a decrease in LAI concurrently show a decrease in evaporation and precipitation, underlining the regional feedback between vegetation and regional hydrological cycle.

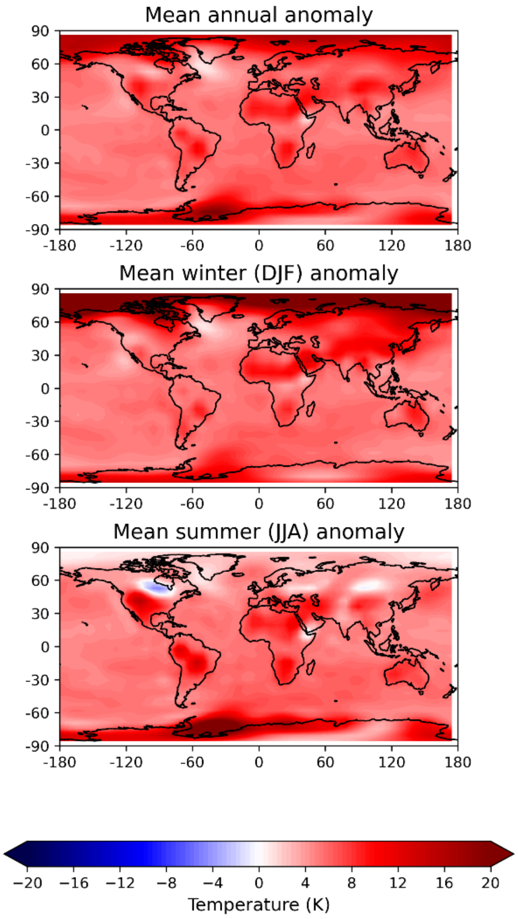

Figure 30: Annual, winter and summer temperature anomaly between the last 50 years of simulation of the 3000-year run and the last 50 years of simulation, after equilibrium was reached, for the 354 ppm run.

As shown in *Figure 30*, temperature increases across all regions of Earth, with higher positive anomalies observed the Arctic during the Winter. However, temperature do not rise in northern latitudes, such as Asia and Canada, during the summer, where an increase in LAI is also observed. Additionally, an increase in evaporation is observed over the same regions in June-July-August, where LAI is rising. The LAI increase could explain the temperature behaviour, as higher evapotranspiration rates in the area, linked to higher LAI, would absorb latent heat.

5.4. Vegetation tipping

The time series of different variables (LAI, evaporation, precipitation, soil moisture, soil water holding capacity and runoff) were analysed in both Europe and the Amazon rainforest, to examine abrupt changes in LAI and its feedback with the hydrological cycle.

5.4.1. Amazon

The time series of LAI was analysed in the grid points shown in black in *Figure 31*. The red points in figure mark locations where abrupt changes were observed.

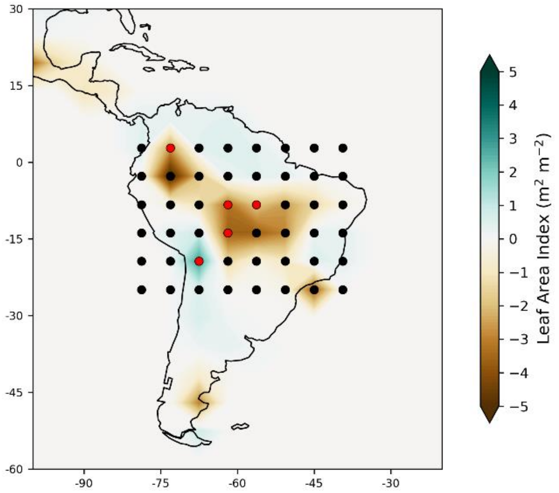

Figure 31: Grid points analysed to identify abrupt changes in LAI, with red points marking locations where such changes were found. The map represents the LAI anomaly, calculated as the difference between the average of the last 50 years of simulation for the 3000-year run and the average over the last 50 years for the 354 ppm run.

The yearly time series of the variables in grid points with abrupt changes are shown in *Figure 32*. The series were plotted using a 25 year running mean, which consists of replacing each value with the average value over a window of 25 years, centred on the year considered. This operation helps reduce noise and attenuate oscillations with a periodicity shorter than 25 years.

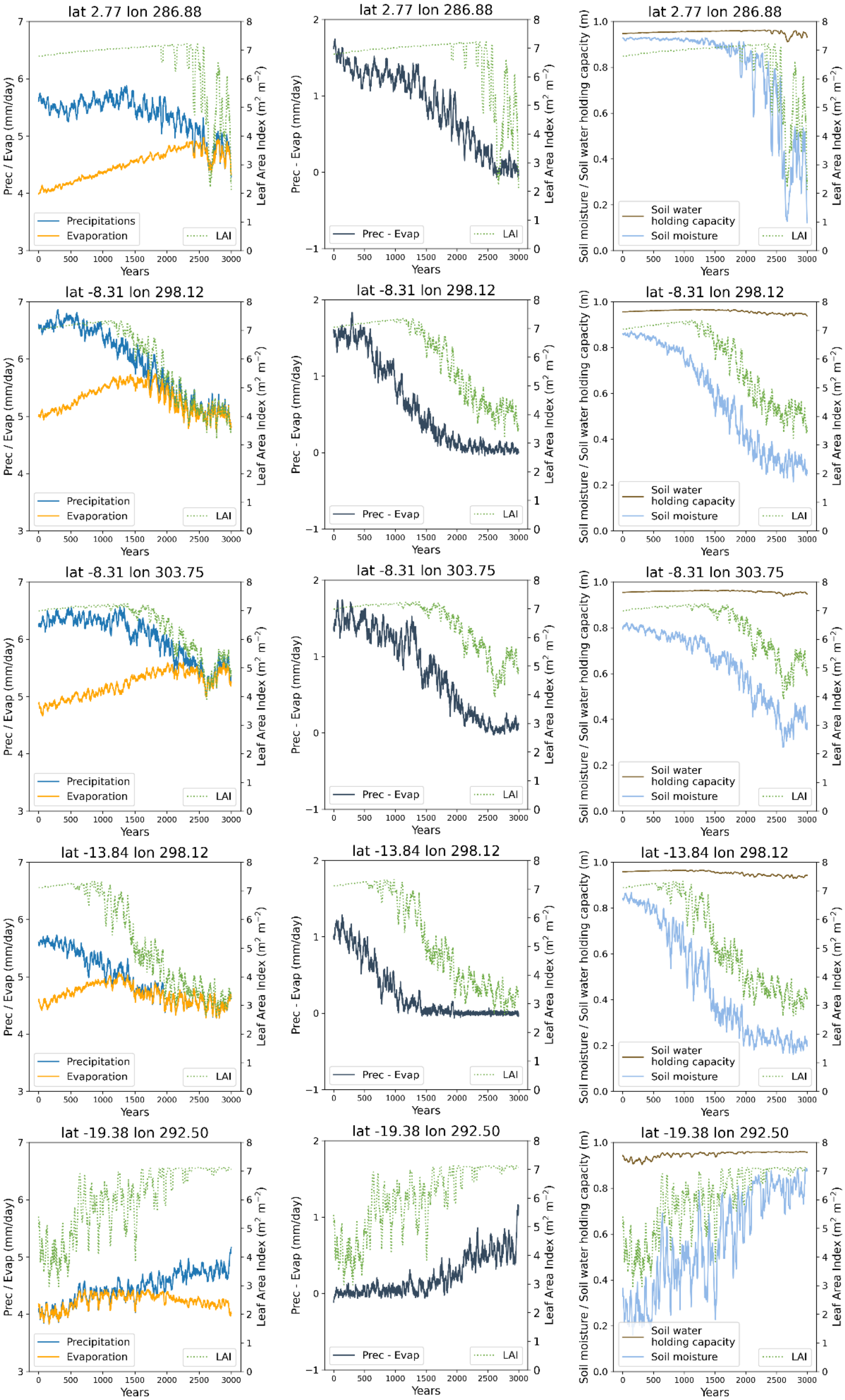

Figure 32: Time series of average yearly values with a 25-year running mean for different grid points. The coordinates, in terms of longitude and latitude, are displayed above each plot. The first column shows LAI,

evaporation and precipitation. The second column shows LAI and the difference between precipitation and evaporation. The third column shows LAI, soil moisture and soil water holding capacity.

Four grid points show a decrease in LAI: one (in the first row) is located in Colombia, two (in the second and third rows) are located in Brazil, close to where the rainforest currently transitions into a savanna, while the fourth grid point (in the fourth row) is centred in Bolivia, near the Brazilian border. Only one grid point (in the last row), centred over the Andes between Bolivia and Chile, shows an abrupt increase in LAI.

The decrease in LAI does not occur simultaneously in all four locations. In the first two points to show a decrease, it happens after approximately 1000 years of simulation, while in the last grid point exhibiting the change, it occurs after about 2500 years.

In the four locations where LAI decreases, before the abrupt change the difference between precipitation and evaporation, shown in the second column, decreases to 0 mm/day. This behaviour is driven by a decline in precipitation and an increase in evaporation, as shown in the first column in *Figure 32*. When precipitation exceeds evaporation, soil moisture increases. when the soil moisture reaches the maximum soil water holding capacity, any water excess produces runoff, which is higher at the beginning of the time series. As shown in the third column, soil water holding capacity on average is higher than soil moisture. As the difference between precipitation and evaporation decreases, water availability is lower, and soil moisture will start to decline. In this case, most of the precipitation is lost to evaporation. The plots clearly show that the reduction in precipitation and the increase in evaporation, which decreases soil moisture, precede the abrupt decline in LAI. Therefore, we can identify the decrease in water availability, caused by changing climatic conditions, as the main cause of the abrupt LAI decrease. A change in climatic conditions, which produces lower precipitation and higher evaporation causes an abrupt decrease in LAI.

In most cases, a delay of several centuries is observed between the initial decrease in soil moisture and the abrupt decline in LAI. As explained in *Chapter 2.2.3*, LAI is a function of vegetation cover. *Equation 25* defines vegetation cover as the minimum between a water-limited parameter, which depends on both soil moisture and soil water holding capacity, and a structurally-limited factor, which depends on biomass. Biomass is derived from Gross Primary Production (GPP), which, as explained in *Chapter 2.2.2*, depends on different variables. The water-limited factor is defined in *Equation 26*, while the structurally limited factor is calculated through *Equation 27.*

$$f_{veg} = \min\left(f_{veg,w}, f_{veg,s}\right) \tag{25}$$

$$f_{veg,w} = \min\left(1, max\left(0, \frac{W_{soil}/W_{max}}{0.25}\right)\right) \tag{26}$$

$$f_{veg,s} = 1 - e^{-0.5*LAI_m} \tag{27}$$

When enough water is available for plants, biomass is the limiting factor for LAI. However, as soil moisture decreases, water availability eventually becomes limiting, triggering a steep decline in LAI. The LAI from the water-limited factor was calculated using *Equation 28*. The resulting plots are shown in *Figure 33.*

$$LAI = -\frac{\ln(1 - f_{veg})}{0.5} \tag{28}$$

From this equation, it is clear that when $f_{veg,w}$ equals 1, LAI cannot be calculated. In this case, the limiting factor is the structurally-limited one, which asymptotically goes to 1 for infinite biomass. To produce the plots in *Figure 33,* the $f_{veg,w}$ was set to 0.98 for all values exceeding this threshold, thus limiting the estimated LAI to a maximum value of 8 m^2 m^{-2}.

Figure 33 shows that LAI from the water-limited factor starts decreasing concurrently with the decline in simulated LAI. At the beginning, the water-limited LAI is higher than the simulated one, indicating that biomass is likely the limiting factor. After soil moisture decreases, water availability eventually becomes limiting. This transition happens several centuries after the simulation begins, when the water-limited LAI becomes similar in values to the simulated LAI.

In some locations, the water-limited LAI remains significantly higher than the simulated LAI, even after the vegetation decline occurs. This is likely due to instances where the water-limiting factor increases to 1 as a result of changes in precipitation and evaporation. In such cases, biomass is the limiting factor. Moreover, following the LAI decline, biomass likely adjusts to lower values due to reduced vegetation cover, which decreases GPP, causing the two limiting factors to alternate over time. It is important to note that the non-linear relationships between LAI, biomass, soil moisture and evaporation complicates the interpretation of relationship between cause and effect.

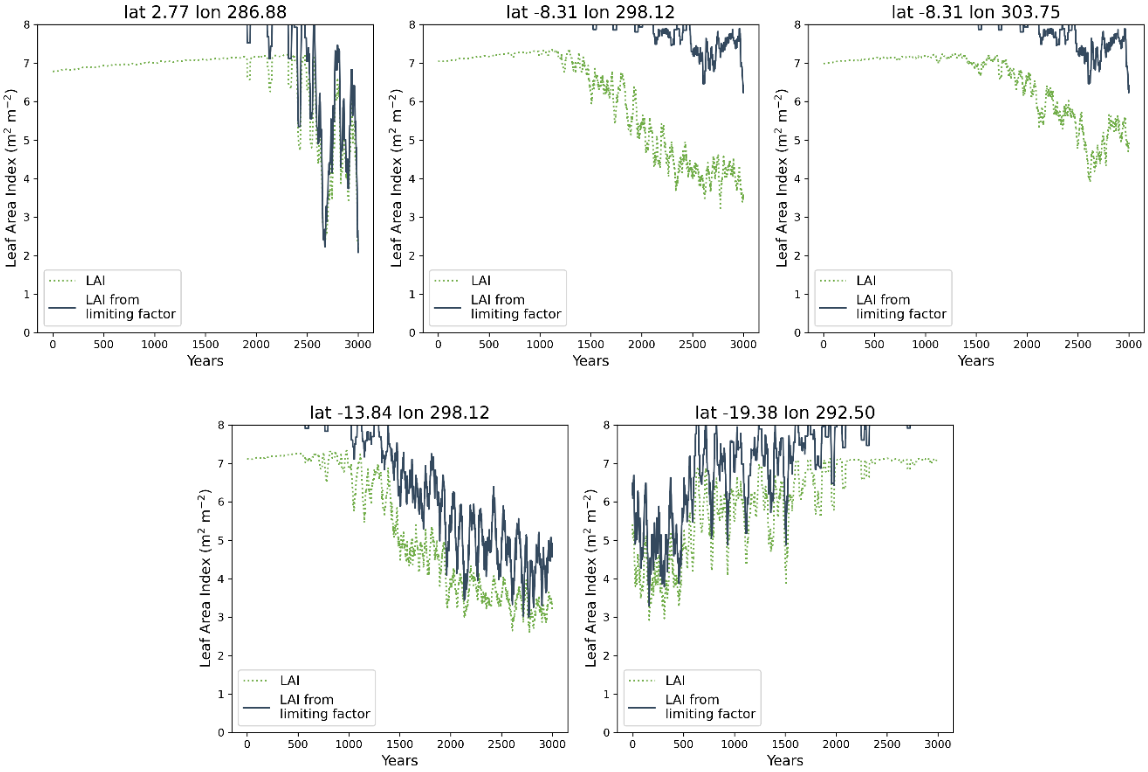

Figure 33: Time series of average yearly values with a 25-year running mean for different grid points. The coordinates, in terms of longitude and latitude, are displayed above each plot. The plots show LAI obtained from PlaSim and the LAI calculated from water-limited factor.

After the decrease in LAI, both evaporation and precipitation decline as well. The response of evaporation to the CO_2 increase is not monotonic. Before the decline in LAI, evaporation increases, which is likely due the growing difference in specific humidity between air and soil, as precipitation decreases. After the LAI declines, evaporation decreases, which can be explained by the lower value of water in soil, which limits evaporation. After the collapse, the variations in evaporation closely follow the variations in both soil moisture and LAI. The soil water holding capacity, shown in *Figure 33*, remains almost constant throughout the years, with values that close to 1 m and a slight decrease for lower LAI values.

In the grid point where an abrupt increase in LAI is observed, the difference between precipitation and evaporation increases from 0 mm/day, the initial value, to a higher value. After the abrupt LAI increase, precipitation shows an increment while evaporation shows a decrease. The soil moisture is continuously increasing throughout the simulation. After the first few centuries, slightly higher precipitation compared to evaporation causes soil moisture to begin rising. After about 750 years the difference between precipitation and evaporation shows a peak, which corresponds to a peak in soil moisture as well. Then, after 1500 years, LAI reaches a higher value, likely driven by higher soil moisture and to the fertilization effect. With the increase in LAI, precipitation and evaporation are decoupled, and the difference increases, thus increasing water availability. As for the other grid points, the change in evaporation is not constant. It increases at the beginning with increasing LAI, but it starts decreasing afterwards, likely due to the decline in the difference in specific humidity between air and soil, as air humidity is increasing.

The abrupt decrease in LAI observed in grid points located in the Amazon rainforest can be explained by a change in the hydrological cycle, which produces a decrease in soil moisture, thus triggering the LAI collapse. This is consistent with what was discussed in *Chapter 5.2.1*. On the other hand, in the location where LAI increases abruptly, the increase precedes the decoupling between precipitation and evaporation. Specifically, precipitation rises while the evaporation decreases, leading to higher water availability.

5.4.2. Europe

As for the Amazon, the time series of LAI was evaluated in Europe as well, and the grid points considered are shown in black in *Figure 34*. The red points in figure mark locations where abrupt changes were observed.

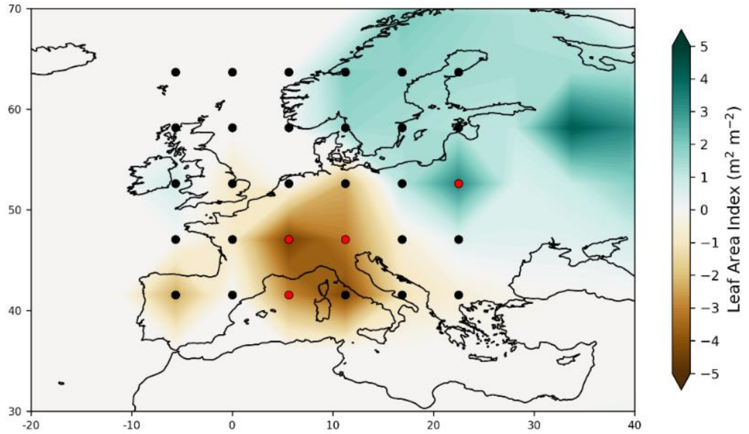

Figure 34: Grid points analysed to identify abrupt changes in LAI, with red points marking locations where such changes were found. The map represents the LAI anomaly, calculated as the difference between the average of the last 50 years of simulation for the 3000-year run and the average over the last 50 years for the 354 ppm run. Some points appear to be over water due to the low resolution of the grid.

The time series of the variables in grid points with abrupt changes are shown in *Figure 32*. In this case as well, the time series were plotted using a 25 year running mean.

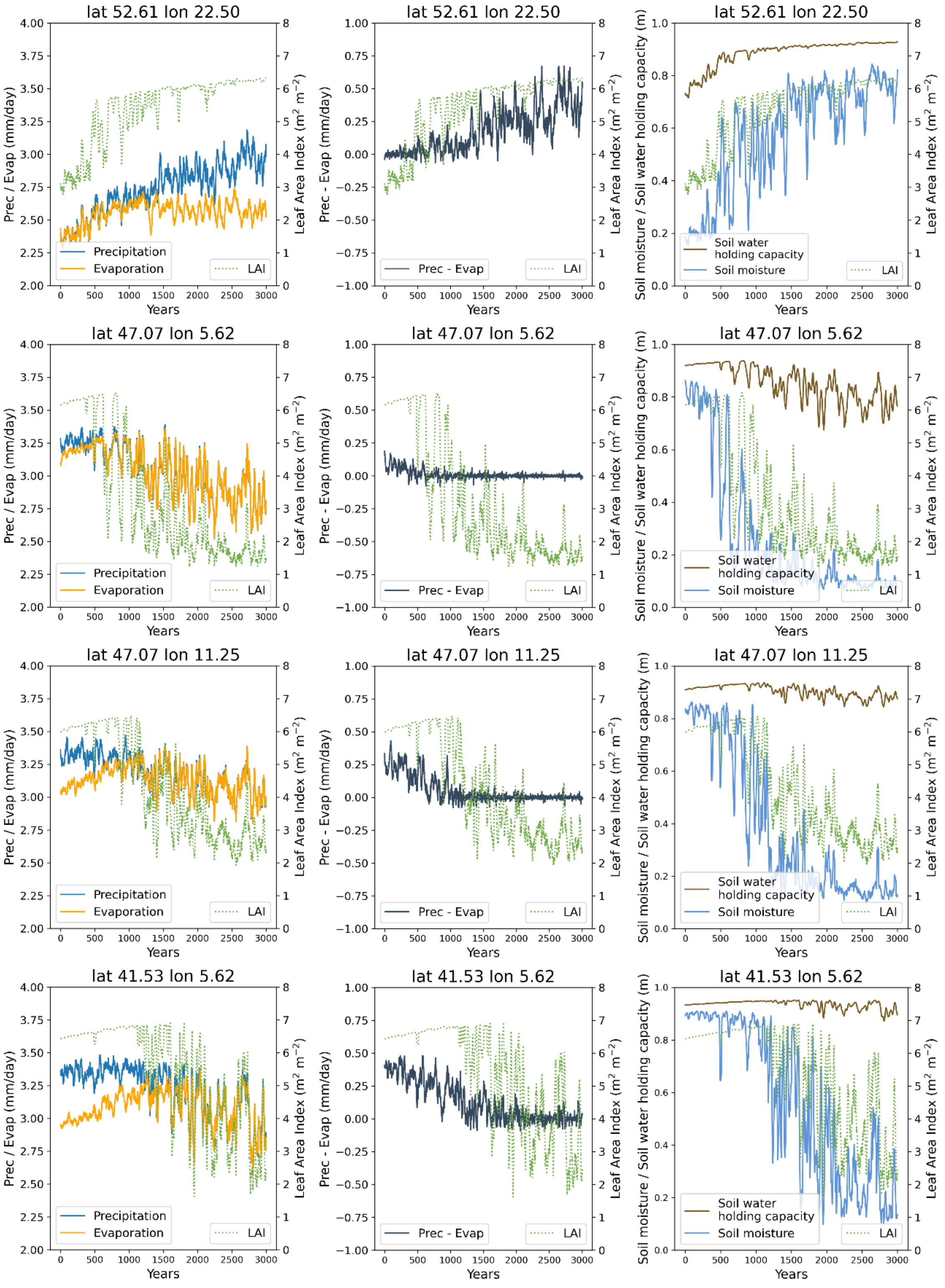

Figure 35: Time series of average yearly values with a 25-year running mean for different grid points. The coordinates, in terms of longitude and latitude, are displayed above each plot. The first column shows LAI, evaporation and precipitation. The second column shows LAI and the difference between precipitation and evaporation. The third column shows LAI, soil moisture and soil water holding capacity.

Three grid points show a decrease in LAI: one (in the second row) is centred in France, close to the border with Switzerland, the second (in the third row) is centred in Austria, while the last one (in the fourth row) is centred in the Mediterranean Sea, near the south of France. Only one grid point, shown in the first row, shows a decrease in LAI. This point is located in Poland.

The decline in LAI does not occur at the same time in the three point, the first point shows a decline after 500 years, while the last experiences an abrupt changes after 1500 years. The time difference is therefore smaller than the one observed in South America. In the point where LAI increases, the fist rise is observed after 500 years, reaching a higher value after around 1500 years of simulation.

In the three locations where LAI decreases, the difference between precipitation and evaporation drops to 0 mm/day, leading to a decline in soil moisture. This behaviour is driven by an increase in evaporation, which starts rising before the abrupt change. The increase in evaporation is likely due to an increase in the difference between soil and atmospheric humidity, included in the evaporation parametrization. On the other hand, precipitation does not show significant changes initially, remaining mostly constant during the first centuries.

Similarly to the Amazon rainforest, the increase in evaporation precedes the abrupt decline in LAI, and it is likely its main cause, as it leads to a reduction in soil moisture, which is one of the limiting factors for LAI. Water availability is therefore the key driver for the LAI decline.

The LAI calculated from the water-limiting factor is plotted in *Figure 36*, and it decreases when the decline begins. However, compared to the Amazon, the water-limited factor is more frequently the limiting factor after the decline, as the water-limited LAI is similar to the simulated one. Still, the two are not completely overlapped, meaning that biomass remains the limiting factor in some instances, even after the decline.

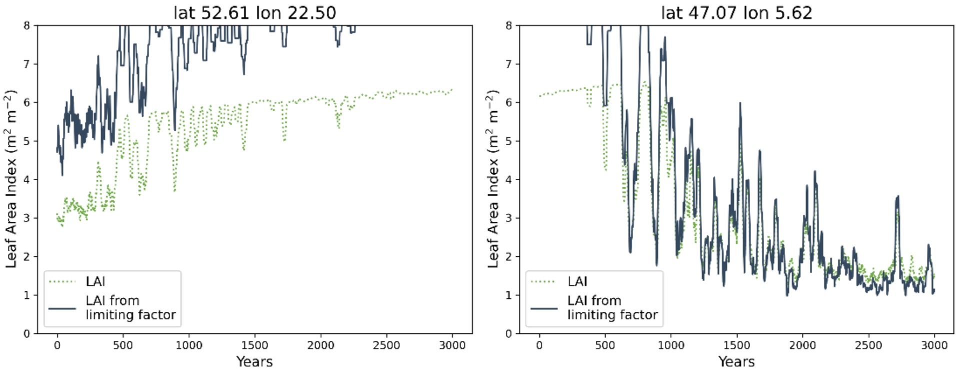

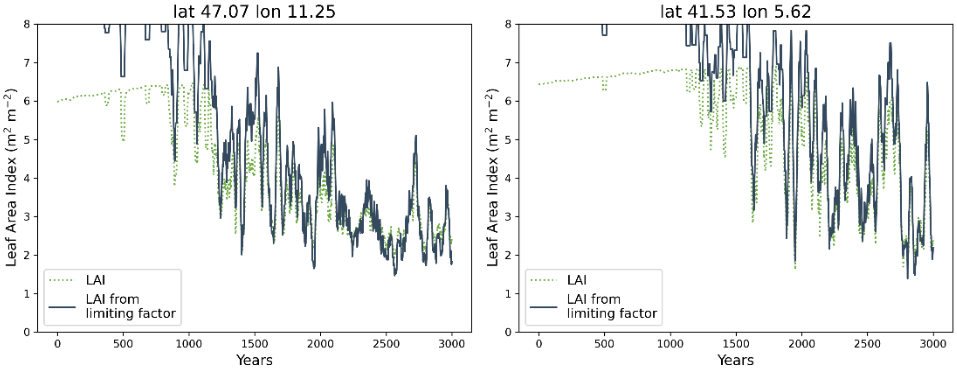

Figure 36: Time series of average yearly values with a 25-year running mean for different grid points. The coordinates, in terms of longitude and latitude, are displayed above each plot. The plots show LAI obtained from PlaSim and the LAI calculated from water-limited factor.

After the LAI decline, both evaporation and precipitation decline as well. The decrease in evaporation is likely due to lower soil moisture, since in PlaSim parametrization evaporation is directly proportional to soil moisture. Moreover, the maximum soil water holding capacity decreases after the decline, due to a reduced biomass, which is a result of both LAI decrease and lower water availability. As opposed to the Amazon rainforest, the grid points in Europe show a shorter delay between the decrease in soil moisture and the decline in LAI. This may be due to the steeper decline in soil moisture in Europe compared to the Amazon, where it becomes a limiting factor later. As shown in *Figure 33* and *Figure 36*, the water-limiting factor reaches lower values in Europe compared to the grid points in South America.

In the grid point where an abrupt increase in LAI is observed, the difference between precipitation and evaporation increases from 0 mm/day, which is the initial value, to a value close to 0.5 mm/day. Similarly to the pattern seen in South America, after LAI increases, precipitation rises while evaporation declines. Initially, slightly higher precipitation compared to evaporation causes soil moisture to begin rising, then, as LAI reaches a higher value, likely driven by an increase in soil moisture and to the fertilization effect, evaporation begins to decline, while precipitation continues to rise. At higher LAI values, precipitation and evaporation become decoupled, with evaporation decreasing as precipitation increases. The decrease in evaporation is likely due to a reduced difference in specific humidity between air and soil, as air humidity is increasing.

Similarly to what was observed in South America, the abrupt decrease in LAI observed in specific grid points in Europe can be attributed to a change in the hydrological cycle, which leads to a decrease in soil moisture. This aligns with the discussion in *Chapter 5.2.2*, which highlighted that the decrease in LAI is to be expected in southern Europe, where soil moisture decreases, while an increase is to be expected in northern latitudes, where the fertilization effect prevails. Additionally, rising temperatures at higher latitudes, accounted in the GPP parametrization, which goes to zero when temperatures drop below 0ºC, may have further contributed to the LAI increase.

5.5. Concluding Remarks

This chapter explored the feedback between interactive vegetation and regional climate, with a focus on vegetation tipping. By comparing two regions such as the Amazon and Europe, the analysis revealed that the hydrological cycle exerts a strong control on vegetation dynamics.

As observed in *Chapter 5.3.2,* regions that experience a decrease in LAI and in forest cover also show a decrease in evaporation. Conversely, in regions where LAI and forest cover increase, evaporation also rises. Precipitation follows more complex patterns, but generally, where LAI decreases, precipitation decreases as well, while it increases where LAI rises. By analysing the grid points in both Europe and South America, it is evident that where LAI abruptly declines both evaporation and precipitation decline as well. In contrast, in the two grid points where LAI abruptly increases, both precipitation and evaporation initially increase, but evaporation begins to decline after the LAI increase.

In South America, a steep decline in LAI was observed in four grid points. The decrease was preceded by a decrease in soil moisture, caused by reduced precipitation and increased evaporation. The decrease in soil moisture subsequently triggered the LAI collapse. The dieback in the analysed region occurred between 1000 and 2500 years after the beginning of the simulation. Only one grid point in the analysed area showed an abrupt increase in LAI, initially accompanied by an increase in both evaporation and precipitation. The abrupt increase of LAI was followed by the decoupling of the two variables from that point onward. This suggests a positive feedback on water availability, which is increased when the two variables are decoupled.

As explained in *Chapter 5.2.1*, the Amazon rainforest is a tipping element of the climate system, as it is at risk of forest dieback, an event associated to an abrupt decrease in LAI. This dieback is driven by several contributing factors, including reduced rainfall, which lead to the regional drying. Patterns that align with this dieback were observed in four of the analysed grid points, all located in the south-east region of the Amazon, the area most vulnerable to vegetation tipping due to precipitation decrease, among other factors. In this region, a decrease in precipitation combined with an increase in evaporation led to a decline in soil moisture, ultimately triggering a sudden drop in LAI.

It is important to note that the results discussed in this chapter primarily consider changes in water availability as the driver of vegetation tipping. Nonetheless, this alone was sufficient to drive the three grid points toward lower LAI values. Other key factors, such as forest fires and human-driven deforestation, which could contribute to Amazon rainforest dieback, were not considered.

In Europe, an abrupt decline in LAI was observed in three grid points, located in central and southern Europe. In these points, the decline was driven by a reduction soil moisture, as a time-invariant precipitation failed to compensate for increasing evaporation. These abrupt decreases occurred between 500 and 1500 years after the simulation began, depending on the grid point. Only one grid point, located in Poland, showed an abrupt increase in LAI, similarly to what was observed in the Amazon. The increase in LAI was followed by a decoupling between precipitation and evaporation, resulting in increased water availability in the region. This suggests a positive feedback on water availability, which is increased when the two variables are decoupled.

As mentioned in *Chapter 5.2.2*, the decrease in water availability in the southern areas of Europe is expected to cause a decrease in vegetation. The analysis carried out in this chapter is consistent with this, as in three grid points reduced water availability resulted in lower soil moisture, which caused an abrupt decrease in LAI. As for the Amazon, the increase in fire risk is also expected to contribute to vegetation loss in southern Europe, which was not considered in this analysis. Conversely, the vegetation is expected to increase in northern latitudes, where an abrupt increase in LAI was observed in one grid point.

Although vegetation does not significantly alter global climatology, it induces significant regional changes. The findings in this chapter highlight the interaction between vegetation and climate, emphasizing the importance of incorporating interactive vegetation in climate models. This allows to improve the representation of regional hydrological response and to better understand the conditions leading to local vegetation tipping.

Conclusions

The Planet Simulator (PlaSim) is an Earth system Model of Intermediate Complexity (EMIC) developed by the University of Hamburg. EMICs bridge the gap between conceptual models, which are simple approximation of the Earth system, and more comprehensive Global Climate Models. They are particularly interesting because they represent the climate system rather completely, while simplifying processes through parametrizations. Moreover, their coarser resolution compared to more complex models allows to simulate longer time scales with significantly lower computational time.

In PlaSim, vegetation is introduced through the Simulator for Biospheric Aspects (SimBA), a simple dynamic global vegetation model. The model can function in two modes: the non-interactive and the interactive vegetation mode. In the non-interactive vegetation mode, the simulated vegetation does not influence the climate, whereas in the interactive mode, vegetation influences the climate through four land-surface variables, representing certain biogeophysical feedbacks. The dynamic vegetation module had rarely been used before, since its interactive vegetation had not yet been tuned.

As a first step, the tuning of SimBA in the interactive vegetation mode was performed by modifying the parametrizations of snow-free albedo and soil water holding capacity. This allowed to represent the climate system as realistically as in the non-interactive version, but with a dynamic vegetation that actively influences the climate system. The tuning allowed to solve biases that the interactive vegetation exhibited prior to tuning, such as a global average temperature lower than observations. The tuned interactive vegetation was then compared to the non-interactive version. Results showed that interactive vegetation does not alter global climatology, but it does cause regional changes, particularly in the hydrological cycle.

The vegetation simulated by PlaSim in the tuned interactive mode was comparable to that simulated by more complex Earth System Models belonging to the CMIP6 project, in terms of both the average global Leaf Area Index (LAI) and the global spatial pattern of annual mean LAI. However, the representation of seasonal patterns in mid-latitude regions, specifically Europe, was not satisfactory compared to CMIP6 models due to the lack of a winter-deciduous phenology in PlaSim, which exclusively represents drought deciduous phenology, based on soil moisture. In tropical regions, specifically the Amazon, the representation of seasonal patterns is as unsatisfactory as the CMIP6 models evaluated. To improve PlaSim performance in reproducing seasonal patterns, a temperature-dependent phenology should be introduced in SimBA.

The vegetation response to extreme global warming was evaluated, revealing two different responses. First, an increase in global average vegetation, assessed through an increase in LAI, due to enhanced fertilization effect and increasing temperatures. This aligns with the projected increase in mean global LAI during the 21st century (Fang et al., 2019). As the atmospheric CO_2 concentration increases, after centuries of simulation, rising temperatures led to changes in the hydrological cycle and to potential crossing of tipping points in oceanic circulation. These changes resulted in lower water availability in some locations in Europe and the Amazon. In these locations, water became the limiting factor for LAI, leading to a sudden decrease in vegetation. Specifically, these events were observed in grid points located both in Southern Europe and in the south-east region of the Amazon rainforest. These results are consistent with the risk of dieback in the Amazon rainforest, which is one of the possible tipping elements of the climate system (Chen et al., 2021), and with the expected decrease in vegetation in Southern Europe (Penuelas et al., 2020; Bednar-Friedl et al., 2022).

Despite the insight provided by this work, some limitations must be addressed. One of the issues is the low resolution of the T21 grid, which limits the tipping analysis to only a few grid points over the two regions considered. Moreover, the analysis is made particularly challenging by the complex phenomenology and the intrinsic complexity of regional vegetation tipping, which remains challenging to be analysed using more comprehensive CMIP6 models, due to their inherent complexity. Additionally, the lack of a sufficient phenological representation in PlaSim further complicates the assessment. Overall, PlaSim-SimBA provides a reasonably adequate climatological representation, allowing to study regional vegetation tipping. However, introducing the dependency of vegetation on temperature would be a necessary improvement to pursue a more accurate assessment of the phenomenon.

Bibliography

Koviessen, S., O'Sullivan, A., Gholami, M., Vining, M., & de Vries, T. (2023). Physical and chemical parameters of various waste materials for living roof systems: A critical review. *194*, 107013. doi:10.1016/j.ecoleng.2023.107013

Andres, H., & Tarasov, L. (2019). Supplementary Material for: Towards understanding potential atmospheric contributions to abrupt climate changes: Characterizing changes to the North Atlantic eddy-driven jet over the last deglaciation. *Climate of the Past, 15*(4), 1621–1646. doi: 10.5194/cp-15-1621-2019-supplement

Angeloni, M. (2022). *Climate variability in an earth system model of intermediate complexity: from interannual to centennial timescales.* PhD dissertation, Università di Bologna.

Angeloni, M., Palazzi , E., & Hardenberg, J. (2020, October). Evaluation and climate sensitivity of the PlaSim v.17 Earth System Model coupled with ocean model components of different complexity. doi:10.5194/gmd-2020-245

Armstrong McKay, D., Staal, A., Abrams, J., Winkelmann, R., Sakschewski, B., Loriani, S., . . . Lenton, T. (2022). Exceeding 1.5°C global warming could trigger multiple climate tipping points. *Science, 377*(6611). doi:10.1126/science.abn7950

Bednar-Friedl, B., Biesbroek, R., Schmidt, D. N., Alexander, P., Børsheim, K. Y., Carnicer, J., . . . Whitmarsh, L. (2022). *Europe. In: Climate Change 2022: Impacts, Adaptation and Vulnerability. Contribution of Working Group II to the.* Cambridge, UK and New York, NY, USA,: Cambridge University Press. doi:10.1017/9781009325844.015

Bonan, G. (2008). Forests and Climate Change: Forcings, Feedbacks, and the Climate Benefits of Forests. *Science, 320*, 1444-1449. doi:10.1126/science.1155121

Boussetta, S., Balsamo, G., Beljaars, A., Kral, T., & Jarlan, L. (2013, April). Impact of a satellite-derived leaf area index monthly climatology in a global numerical weather prediction model. *International Journal of Remote Sensing, 34*(9-10), 3520-3542. doi: 10.1080/01431161.2012.716

Cao, S., Li, M., Zhu, Z., Wang, Z., Zha, J., Zhao, W., . . . Piao, S. (2023). Spatiotemporally consistent global dataset of the GIMMS leaf area index (GIMMS LAI4g) from 1982 to 2020. *Earth System Science Data, 15*(11), 4877-4899. doi:10.5194/essd-15-4877-2023

Cao, S., Li, M., Zhu, Z., Wang, Z., Zha, J., Zhao, W., . . . Piao, S. (2023). Spatiotemporally consistent global dataset of the GIMMS Leaf Area Index (GIMMS LAI4g) from 1982 to 2020 (V1.2) (V1.2) [Data set]. Zenodo. doi:10.5281/zenodo.8281930

Chapin, F. S., & Eviner, V. T. (2007). 8.06 - Biogeochemistry of Terrestrial Net Primary Production. In *Treatise on Geochemistry* (pp. 1-35). Pergamon. doi:10.1016/B0-08-043751-6/08130-5

Chen, D., Rojas, M., Samset, B., Cobb, K., Diongue Niang, A., Edwards, P., . . . Tréguier, A.-M. (2021). *Framing, Context, and Methods. In Climate Change 2021: The Physical Science Basis. Contribution of Working Group I to the Sixth Assessment Report of the Intergovernmental Panel on Climate Change.* Cambridge, United Kingdom and New York, NY, USA: Cambridge University Press. doi:10.1017/9781009157896.003

Clark, D., Mercado, L., Sitch, S., Jones, C., Gedney, N., Best, M., . . . Cox, P. (2011). The Joint UK Land Environment Simulator (JULES), model description – Part 2: Carbon fluxes and vegetation dynamics. *Geosci. Model Dev., 4*, 701-722. doi:10.5194/gmd-4-701-2011

Dahlin, K. M., Fisher, R. A., & Lawrence, P. J. (2015). Environmental drivers of drought deciduous phenology in the Community Land Model. *Biogeosciences, 12*, 5061–5074. doi:10.5194/bg-12-5061-2015

Döscher, R., Acosta, M., Alessandri, A., Anthoni, P., Arneth, A., Arsouze, T., . . . Zhang, Q. (2021). The EC-Earth3 Earth System Model for the Climate Model Intercomparison Project 6. doi:10.5194/gmd-2020-446

Du, Q., Xing, G., Jiao, X., Song, X., & Li, J. (2018). Stomatal responses to long-term high vapor pressure deficits mediated most limitation of photosynthesis in tomatoes. *Acta Physiologiae Plantarum, 40*, 149. doi:10.1007/s11738-018-2723-7

Duveiller, G., Pickering, M., Muñoz-Sabater, J., Caporaso, L., Boussetta, S., Balsamo, G., & Cescatti, A. (2023). Getting the leaves right matters for estimating temperature extremes. *Geosci. Model Dev., 16*(24), 7357–7373. doi:10.5194/gmd-16-7355-2023.

Estiarte, M., & Peñuelas, J. (2015). Alteration of the phenology of leaf senescence and fall in winter deciduous species by climate change: effects on nutrient proficiency. *Global Change Biology, 21*, 1005-1017. doi: 10.1111/gcb.12804

European Centre for Medium-Range Weather Forecasts (ECMWF). (2023, April 17). *CMIP6: Global climate projections*. Retrieved from ECMWF Confluence: https://confluence.ecmwf.int/display/COPSRV/CMIP6%3A%2BGlobal%2Bclimate%2Bprojections?utm_source=chatgpt.com

European Centre for Medium-Range Weather Forecasts (ECMWF). (2025, January 24). *ERA5: data documentation*. Retrieved from ECMWF Confluence: https://confluence.ecmwf.int/display/CKB/ERA5%3A+data+documentation#ERA5:datadocumentation-Parameterlistings

European Centre for Medium-Range Weather Forecasts (ECMWF). (n.d.). *ECMWF Reanalysis v5 (ERA5)*. Retrieved from ECMWF: https://www.ecmwf.int/en/forecasts/dataset/ecmwf-reanalysis-v5

Eyring, V., Bony, S., Meehl, G. A., Senior, C. A., Stevens, B., Stouffer6, R. J., & Taylor, K. E. (2016). Overview of the Coupled Model Intercomparison Project Phase 6 (CMIP6) experimental design and organization. *Geoscientific Model Development, 9*(5), 1937-1958. doi:10.5194/gmd-9-1937-2016

Fadón, E., Fernandez, E., Behn, H., & Luedeling, E. (2020). A Conceptual Framework for Winter Dormancy in Deciduous trees. *Agronomy, 10*(2), 241. doi:10.3390/agronomy10020241

Fang, H., Frederic, B., Plummer, S., & Schaepman-Strub, G. (2019). An Overview of Global Leaf Area Index (LAI): Methods, Products, Validation, and Applications. *Reviews of Geophysics*. *57*(3). doi:10.1029/2018RG000608.

FAO (Food and Agriculture Organization of the United Nations). (2020). *Global Forest Resources Assessment 2020: Main findings.* Retrieved from https://openknowledge.fao.org/server/api/core/bitstreams/8f8f2820-6df4-4746-9295-e9356148f8a2/content/CA8642EN.html#chapter-2_2

Flato, G., Marotzke, J., Abiodun, B., Braconnot, P., Chou, S. C., Collins, W., . . . Rummukainen, M. (2013). *Evaluation of Climate Models. In: Climate Change 2013: The Physical Science Basis. Contribution of Working Group I to the Fifth Assessment Report of the Intergovernmental Panel on Climate Change.* Cambridge, United Kingdom and New York, NY, USA: Cambridge University Press.

Forster, P., Storelvmo, T., Armour, K., Collins, W., Dufresne, J.-L., Frame, D., . . . Zhang, H. (2021). *The Earth's Energy Budget, Climate Feedbacks, and Climate Sensitivity. In Climate Change 2021: The Physical Science Basis. Contribution of Working Group I to the Sixth Assessment Report of the Intergovernmental Panel on Climate Change.* Cambridge, United Kingdom and New York, NY, USA: Cambridge University Press. doi:10.1017/9781009157896.009

Fraedrich, K., Kirk, E., & Lunkeit, F. (2009). *PUMA Portable University Model of the Atmosphere.* doi:10.2312/WDCC/DKRZ_Report_No16

Franks, P. J., Adams, M. A., Amthor, J. S., Barbour, M. M., Berry, J. A., Ellsworth, D. S., . . . von Caemmerer, S. (2012). Sensitivity of plants to changing atmospheric CO2 concentration: from the geological past to the next century. *New Phytologist, 197*(4), 1077-1094. doi:10.1111/nph.12104

Gettelman, A. (2023). Rainbows and climate change: a tutorial on climate model diagnostics and parameterization. doi:10.5194/egusphere-2023-227

Global Climate Observing System. (n.d.). *Leaf Area Index*. Retrieved from Global Climate Observing System: https://wmo.int/site/global-climate-observing-system-gcos/essential-climate-variables/leaf-area-index#:~:text=The%20Leaf%20Area%20Index%20(LAI,present%20in%20the%20specified%20environment.

Gobron, N., & Verstraete, M. M. (2009). *Assessment of the status of the development of the standards for the Terrestrial Essential Climate Variables: Leaf Area Index.* Retrieved from https://lpvs.gsfc.nasa.gov/PDF/TerrestrialECV/T11.pdf

Golovko, T. K., & Garmash, E. V. (2022). Plant Respiration: Classical and Current Notions. *Russian Journal of Plant Physiology, 69*(6), 563–571. doi:10.1134/S1021443722060073

Hagemann, S. (2002). *An Improved Land Surface Parameter Dataset.* Technical Report No. 336, Max Planck Institute for Meteorology. doi:10.17617/2.2344576

Hersbach, H., Bell, B., Berrisford, P., Biavati, G., Horányi, A., Muñoz Sabater, J., . . . Thépaut, J.-N. (2023). *ERA5 monthly averaged data on single levels from 1940 to present.* Copernicus Climate Change Service (C3S) Climate Data Store (CDS). doi:10.24381/cds.f17050d7

Hourdin, F., Mauritsen, T., Gettelman, A., Golaz, J.-C., Balaji, V., Duan, Q., . . . Williamson, D. (2017). Supplementary material for "The Art and Science of Climate Model Tuning". *American Meteorological Society, 98*, 589-602. doi:10.1175/BAMS-D-15-00135.2

Huete, A., Didan, K., Miura, T., Rodriguez, E. P., Gao, X., & Ferreira, L. G. (2002). Overview of the radiometric and biophysical performance of the MODIS vegetation indices. *Remote Sensing of Environment*. doi:10.1016/S0034-4257(02)00096-2.

Intergovernmental Panel on Climate Change (IPCC). (1990). *Climate Change: the IPCC Scientific Assessment.* Cambridge: Cambridge University Press.

IPCC. (2012). *Glossary of terms. In: Managing the Risks of Extreme Events and Disasters to Advance Climate Change Adaptation.* Cambridge, UK, and New York, NY, USA: Cambridge University Press.

Jiang, W., Gastineau, G., & Codron, F. (2020). Multicentennial Variability Driven by Salinity Exchanges Multicentennial Variability Driven by Salinity Exchanges Climate Model. *Journal of Advances in Modeling Earth Systems, 13*(3). doi:10.1029/2020MS002366

Kelliher, F. M., Leuning, R., Raupach, M. R., & Schulze, E. D. (1995). Maximum conductances for evaporation from global vegetation types. *Agricultural and Forest Meteorology*, 1-16. doi:10.1016/0168-1923(94)02178-M

Kleidon, A. (2006). The climate sensitivity to human appropriation of vegetation productivity and its thermodynamic characterization. *Global and Planetary Change, 54*(1-2), 109-127. doi: 10.1016/j.gloplacha.2006.01.016

Lan, X., & Keeling, R. (n.d.). *Trends in Atmospheric Carbon Dioxide (CO2)*. Retrieved from Global Monitoring Laboratory: https://gml.noaa.gov/ccgg/trends/data.html

Liepert, B. G., & Previdi, M. (2012). Inter-model variability and biases of the global water cycle in CMIP3 climate models. *Environmental Research Letters*. doi:10.1088/1748-9326/7/1/014006

Lu, L., Kuenzer, C., Wang, C., Guo, H., & Li, Q. (2015). Evaluation of Three MODIS-Derived Vegetation Index Time Series for Dryland Vegetation Dynamics Monitoring. *Remote Sensing, 7*(6). doi:10.3390/rs70607597

Lunkeit, F., Borth, H., Bottinger, M., Fraedrich, K., Jansen, H., Kirk, E., . . . Wan, H. (2011). *Planet Simulator Reference Manual Version 16.* Retrieved from https://www.mi.uni-hamburg.de/en/arbeitsgruppen/theoretische-meteorologie/modelle/sources/psreferencemanual-1.pdf

Maier-Reimer, E., Mikolajewicz, U., & Hasselmann, K. (1993). Mean Circulation of the Hamburg LSG OGCM and Its Sensitivity to the Thermohaline Surface Forcing. *Journal of Physical Oceanography*, *23*, 731–757. doi:10.1175/1520-0485(1993)023<0731:MCOTHL>2.0.CO;2

Marengo, J., Nobre, C., Betts, R., Cox, P., Sampaio, G., & Salazar Velásquez, L. (2009). Global Warming and Climate Change in Amazonia: Climate-Vegetation Feedback and Impacts on Water Resources. *Geophysical Monograph Series, 186*, 273-292. doi:10.1029/2008GM000743

Marengo, J., Nobre, C., Sampaio, G., Salazar Velásquez, L., & Borma, L. (2011). Climate change in the Amazon Basin: Tipping points, changes in extremes, and impacts on natural and human systems. In *Tropical Rainforest Responses to Climatic Change.* Springer. doi:10.1007/978-3-642-05383-2_9

Miller, R., Schmidt, G., Nazarenko, L., Bauer, S., Kelley, M., Ruedy, R., . . . Yao, M.-S. (2021). CMIP6 Historical Simulations (1850-2014) with GISS-E2.1. *Journal of Advances in Modeling Earth Systems, 13*(1). doi:10.1029/2019MS002034

Myhre, G., Highwood, E., Shine, K., & Stordal, F. (1998). New estimates of raditive forcing due to well mixed greenhouse gases. *Geophysical Research Letters, 25*(14), 2715-2718. doi:10.1029/98GL01908

National Aeronautics and Space Administration. (n.d.). *about MODIS.* Retrieved from MODIS: Moderate Resolution Imaging Spectroradiometer: https://modis.gsfc.nasa.gov/about/

National Oceanic and Atmospheric Administration (NOAA). (n.d.). *AVHRR data and products*. Retrieved from NOAA Comprehensive Large Array-data Stewardship System (CLASS): https://www.class.noaa.gov/data_available/avhrr/index.htm

Nian, D., Bathiany, S., Ben-Yami, M., Blaschke, L. L., Hirota, M., Rodrigues, R. R., & Boers, N. (2023). A potential collapse of the Atlantic Meridional Overturning Circulation may stabilise eastern Amazonian rainforests. *Communications Earth & Environment, 4*, 470. doi:10.1038/s43247-023-01123-7

OECD. (2022). *Climate Tipping Points: Insights for Effective Policy Action.* Paris: OECD Publishing. doi:https://doi.org/10.1787/abc5a69e-en

Olson, D., Dinerstein, E., Wikramanayake, E., Burgess, N., Powell, G., Underwood, E., . . . Kassem, K. (2001). Terrestrial Ecoregions of the World: A New Map of Life on Earth. *BioScience, 51*(11), 933-938. doi:10.1641/0006-3568(2001)051[0933:TEOTWA]2.0.CO;2

Pandey, V., Harde, S., Rajasekaran, E., & Debburman, P. (2024). Gross primary productivity of terrestrial ecosystems: a review of observations, remote sensing, and modelling studies over South Asia. *Theoretical and Applied Climatology, 155*(9), 8461-8491. doi:10.1007/s00704-024-05158-4

Parry, I., Ritchie, P., & Cox, P. (2022). Evidence of localised Amazon rainforest dieback in CMIP6 models. *Earth Syst. Dynam., 13*, 1667–1675. doi:10.5194/esd-13-1667-2022

Penuelas, J., Fernández-Martínez, M., Vallicrosa, H., Maspons, J., Zuccarini, P., Carnicer, J., . . . Sardans, J. (2020). Increasing atmospheric CO2 concentrations correlate with declining nutritional status of European forests. *Communications Biology, 3*, 125. doi:10.1038/s42003-020-0839-y

Phillips, O., Aragão, L., Lewis, S., Fisher, J., Lloyd, J., Lopez-Gonzalez, G., . . . Torres-Lezama, A. (2009). Drought Sensitivity of the Amazon Rainforest. *Science, 323*, 1344-7. doi:10.1126/science.1164033

Port, U., Brovkin, V., & Claussen, M. (2012). The influence of vegetation dynamics on anthropogenic climate change. *Earth System Dynamics, 3*, 233-243. doi:10.5194/esd-3-233-2012

Prentice, I. C., Williams, S., & Friedlingstein, P. (2015). *Biosphere feedbacks and climate change - Grantham Briefing Paper 12.* London: Grantham Institute.

Qin, H., Wang, C., Zhao, K., & Xi, X. (2018). Estimation of the fraction of absorbed photosynthetically active radiation (fPAR) in maize canopies using LiDAR data and hyperspectral imagery. *PLOS ONE, 13*(5). doi:10.1371/journal.pone.0197510

Reick, C. H., Gayler, V., Goll, D., Hagemann, S., Heidkamp, M., Nabel, J., . . . Wilkenskjeld, S. (2021). *JSBACH 3 The land component of the MPI Earth System Model Documentation of version 3.2.* Hamburg: Max Planck Institute for Meteorology. doi:10.17617/2.3279802

Romano, N., Palladino, M., & Chirico, G. B. (2011). Parameterization of a bucket model for soil-vegetation-atmosphere modeling under seasonal climatic regimes. *Hydrol. Earth Syst. Sci., 15*, 3877–3893. doi:10.5194/hess-15-3877-2011

Schaik, C., Terborgh, J., & Wright, J. S. (2003). The Phenology of Tropical Forests: Adaptive Significance and Consequences for Primary Consumers. *Annual Review of Ecology and Systematics, 24*(1), 353-377. doi:10.1146/annurev.es.24.110193.002033

Sellar, A., Jones, C., Mulcahy, J., Tang, Y., Yool, A., Wiltshire, A., . . . Zerroukat, M. (2019). UKESM1: Description and Evaluation of the U.K. Earth System Model. *Journal of Advances in Modeling Earth Systems, 11*(12), 4513-4558. doi:10.1029/2019MS001739

Shi, X., Lohmann, G., Sidorenko, D., & Yang, H. (2020). Early-Holocene simulations using different forcings and resolutions in AWI-ESM. *The Holocene, 30*(1). doi:10.1177/0959683620908634

Shi, Y., Gong, W., Duan, Q., Jackson, C., Xiao, C., & Wang, H. (2019). How parameter specification of an Earth system model of intermediate complexity influences its climate simulations. *Progress in Earth and Planetary Science, 6*(1), 46. doi:10.1186/s40645-019-0294-x

Siqueira Silva, D. H., Castro-Gamboa, I., & Da Silva Bolzani, V. (2010). Plant Diversity from Brazilian Cerrado and Atlantic Forest as a Tool for Prospecting Potential Therapeutic Drugs. In *Comprehensive Natural Products II* (pp. 95-133). Elsevier. doi:10.1016/B978-008045382-8.00061-7

Smith, B. (2007). *LPJ-GUESS – an ecosystem modelling framework.*

Song, X., Wang, D.-Y., Li, F., & Zeng, X.-D. (2021). Evaluating the performance of CMIP6 Earth system models in simulating global vegetation structure and distribution. *Advances in Climate Change Research, 12*(4), 584-595. doi:10.1016/j.accre.2021.06.008

Staal, A., Fetzer, I., Wang-Erlandsson, L., Bosmans, J. H., Dekker, S. C., van Nes, D. H., . . . Tuinenburg, O. A. (2020). Hysteresis of tropical forests in the 21st century. *Nat Commun., 11*(1), 4978. doi:10.1038/s41467-020-18728-7

Tang, H., Brolly, M., Zhao, F., Strahler, A. H., Schaaf, C. L., Ganguly, S., . . . Dubayah, R. (2014). Deriving and validating Leaf Area Index (LAI) at multiple spatial scales through lidar remote sensing: A case study in Sierra National Forest, CA. *Remote Sensing of Environment, 143*, 131-141. doi:10.1016/j.rse.2013.12.007

Universitat Hamburg. (2022, May). *Planet Simulator*. Retrieved from Universitat Hamburg: https://www.mi.uni-hamburg.de/en/arbeitsgruppen/theoretische-meteorologie/modelle/plasim.html

von Schuckmann, K., Minière, A., Gues, F., Cuesta-Valero, F. J., Kirchengast, G., Adusumilli, S., . . . Zemp, M. (2023). Heat stored in the Earth system 1960–2020: Where does the energy go? *15*, 1675–1709. doi:10.5194/essd-15-1675-2023

Wunderling, N., Staal, A., Sakschewski, B., Hirota, M., Tuinenburgd, O. A., Donges, J. F., . . . Winkelmann, R. (2022). Recurrent droughts increase risk of cascading tipping events by outpacing adaptive capacities in the Amazon rainforest. *Environmental Sciences, 119*(32). doi:10.1073/pnas.2120777119

Xu, X., & Chen, D. (2024). Estimating global annual gross primary production based on satellite-derived phenology and maximal carbon uptake capacity. *Environmental Research, 252*. doi: 10.1016/j.envres.2024.119063

Yan, G., Hu, R., Luo, J., Weiss, M., Jiang, H., Mu, X., . . . Zhang, W. (2019). Review of indirect optical measurements of leaf area index: Recent advances, challenges, and perspectives. *Agricultural and Forest Meteorology*, *265*(15), 390-411. doi:10.1016/j.agrformet.2018.11.033

Yang, Y., Huang, Q., Wu, Z., Wu, T., Luo, J., Dong, W., . . . Zhang, D. (2022, July). Mapping crop leaf area index at the parcel level via inverting a radiative transfer model under spatiotemporal constraints: A case study on sugarcane. *Computers and Electronics in Agriculture*. doi: 10.1016/j.compag.2022.107003

Zhu, Z., Piao, S., Myneni, R. M., Huang, M., Zeng, Z., Canadell, J. G., . . . Zeng, N. (2016, April). Greening of the Earth and its drivers. *Nature Climate Change, 6*(8), 791-795. doi:10.1038/nclimate3004